

Alternans, ephaptic coupling and their relation to
ventricular arrhythmias

A DISSERTATION
SUBMITTED TO THE FACULTY OF THE GRADUATE SCHOOL
OF THE UNIVERSITY OF MINNESOTA
BY

Ning Wei

IN PARTIAL FULFILLMENT OF THE REQUIREMENTS
FOR THE DEGREE OF
Doctor of Philosophy

Prof. Yoichiro Mori and Prof. Alena Talkachova

May, 2016

© Ning Wei 2016
ALL RIGHTS RESERVED

Acknowledgements

First of all, I would like to thank my advisors Prof. Yoichiro Mori and Prof. Alena Talkachova for guiding me through my academic careers as a graduate student and leading me to learn cardiac physiology, which is a very intriguing subject. I learned a tremendous amount from them.

I benefited a lot from the discussions with Prof. Charlie Peskin from Courant Institute of Mathematical Sciences, New York University and Prof. James Keener from University of Utah, who shared with me their insights into my work.

I also would like to thank my committee members Prof. Richard McGehee, Prof. Duane Nykamp for reviewing my thesis and serving on the committee of my thesis defence. I really appreciate their help.

Finally, I would like to thank my lab mates Steven Lee, Elizabeth Annoni, Kanchan Kulkarni and Christopher Johnson for their discussions and help.

Abstract

The heart functions as a mechanical pump that propels blood through the circulatory system. Blood flows from the body into the right atrium, and then into the right ventricle where it gets pumped into the lungs through the pulmonary artery. Blood gets oxygenated in the lungs, flows into the left atrium, and then into the left ventricle where it gets pumped through the aorta to different organs of the body. Ventricular fibrillation (VF), identified as disorganized and ineffective quiver of the ventricles, is the most serious ventricular arrhythmias. When VF occurs, the heart is unable to pump blood. Sudden cardiac arrest follows. About 220,000 deaths from heart attacks in the United States each year are thought to be caused by VF.

Alternans, a periodic beat-to-beat short-long alternation in action potential duration (APD), is considered to be a precursor of VF. In extended cardiac tissue, electrical alternans can be either spatially concordant (SCA, all cells oscillate in phase) or spatially discordant (SDA, cells in different regions oscillate out of phase). SDA gives rise to an increase in the spatial dispersion of repolarization, which is thought to be proarrhythmic. In this dissertation, I use a mapping model with two beats of memory, a simple but powerful tool to study cardiac dynamics and their relation to VF at the level of single cell and a spatially coupled cell strand.

Ventricular myocytes are connected electrically by gap junction channels formed mainly by connexin 43 (Cx43) and, to a smaller extent, Cx45. Decreased and heterogeneous expression of Cx43 is a common feature in animal heart failure models. Ephaptic coupling is an electric field mechanism of propagation. It relies on the presence of narrow cleft space between neighboring cells, which is resistively connected to the extracellular space. Emerging evidence suggests a more active role for ephaptic coupling in mediating intercellular electrical communication when gap junctions are reduced in a homogeneous manner. Here, I explore the effect of ephaptic coupling when Cx43 expression is reduced in a heterogeneous fashion. For this purpose, I use a physiologically detailed ionic channel model with their gating kinetics applied in a two dimensional tissue model of electrically coupled cardiac cells.

Contents

| | |
|---|-----------|
| Acknowledgements | i |
| Abstract | ii |
| List of Tables | v |
| List of Figures | vi |
| 1 Introduction | 1 |
| 1.1 The role of short term memory and conduction velocity restitution in alternans formation | 3 |
| 1.2 The dual effect of ephaptic coupling on cardiac conduction with heterogeneous expression of connexin 43 | 3 |
| 2 Cardiac alternans | 6 |
| 2.1 Cardiac action potential | 6 |
| 2.2 Alternans | 7 |
| 2.3 Overview of SDA studies | 9 |
| 2.4 Motivation of our study | 10 |
| 3 The role of short term memory and conduction velocity restitution in alternans formation. | 11 |
| 3.1 Materials and Methods | 12 |
| 3.1.1 Mapping model with two beats of memory | 12 |
| 3.1.2 Spatially coupled mapping model | 13 |

| | | |
|----------|--|-----------|
| 3.1.3 | Pacing protocols | 14 |
| 3.1.4 | Overpacing and conduction block | 15 |
| 3.2 | Results | 20 |
| 3.2.1 | Dynamical responses of single cell | 20 |
| 3.2.2 | SDA in spatially coupled mapping model | 22 |
| 3.3 | Conclusion and discussions | 29 |
| 4 | Cardiac action potential propagation | 31 |
| 4.1 | Global cardiac action potential propagation | 31 |
| 4.2 | Local cardiac action potential propagation | 32 |
| 4.2.1 | Contraction of cardiac myocytes | 33 |
| 4.2.2 | Gap junctions | 33 |
| 4.2.3 | Ephaptic coupling | 35 |
| 4.3 | Motivation of our study | 39 |
| 5 | The dual effect of ephaptic coupling on cardiac conduction with heterogeneous expression of connexin 43 | 40 |
| 5.1 | Materials and Methods | 40 |
| 5.1.1 | Mathematical model | 40 |
| 5.1.2 | Numerical simulation | 46 |
| 5.2 | Results | 47 |
| 5.2.1 | The effect of ephaptic coupling on cardiac conduction. | 47 |
| 5.2.2 | Conduction features when Cx43KO content is 100% ($p = 1$). | 48 |
| 5.2.3 | Conduction block (CB) in mixed genotype lattices. | 59 |
| 5.2.4 | Mechanisms behind the increased proportions of CB. | 63 |
| 5.3 | Conclusions and discussions | 69 |
| | References | 71 |
| | Appendix A. Derivation of ξ and ω in chapter 3 | 79 |

List of Tables

| | | |
|-----|--|----|
| 3.1 | Parameters Abbreviations. | 15 |
| 5.1 | Parameters that enter our model. | 46 |
| 5.2 | Number of CB for a 2×75 lattice. | 61 |
| 5.3 | Number of CB for a 3×75 lattice. | 62 |
| 5.4 | Number of CB for a 6×75 lattice. | 62 |
| 5.5 | Number of CB for a 10×75 lattice. | 63 |
| 5.6 | Number of CB for a 16×75 lattice. | 63 |

List of Figures

| | | |
|-----|---|----|
| 1.1 | Blood circulation in the heart. | 2 |
| 2.1 | Transmembrane potential traces of two APs. | 6 |
| 2.2 | APD bifurcation. | 7 |
| 2.3 | Schematic view of SCA and SDA in simulated cardiac tissue. | 8 |
| 2.4 | T wave alternans. | 9 |
| 3.1 | CV restitution. | 13 |
| 3.2 | Overpacing of single cell and cable. | 18 |
| 3.3 | The effect of overpacing on single cell. | 19 |
| 3.4 | Dynamical responses of single cell. | 21 |
| 3.5 | The effect of overpacing in cable. | 23 |
| 3.6 | Stable and unstable SDA nodal behaviors. | 24 |
| 3.7 | Nodal positions and time to reach steady state against α | 25 |
| 3.8 | Dynamical responses of the cable. | 28 |
| 4.1 | Action potential propagation throughout the heart. | 32 |
| 4.2 | Gap junctions between adjacent cells. | 34 |
| 4.3 | ID of branched cardiomyocytes. | 35 |
| 4.4 | Ephaptic mechanism. | 37 |
| 5.1 | 2D bidomain model with ephaptic coupling incorporated. | 45 |
| 5.2 | CV_L plotted against d_{cleft} for $p = 1$ and 0 | 48 |
| 5.3 | Alternating conduction. | 51 |
| 5.4 | End transmembrane potential traces for different d_{cleft} | 52 |
| 5.5 | Instability of planar fronts. | 54 |
| 5.6 | SAP. | 56 |
| 5.7 | Intermediate wave. | 56 |

| | | |
|------|---|----|
| 5.8 | Activation gating variable (m) profile of Na^+ channels residing on the end membrane and ϕ profile when SAP occurs. | 57 |
| 5.9 | Activation gating variable (d) profile of L-type Ca^{2+} channels residing on the end and side membranes and ϕ profile when SAP, intermediate wave and normal conduction occur. | 58 |
| 5.10 | Representative plots of EAT along a 6×75 lattice, where $p = 0.6$, $d_{\text{cleft}} = 2$ nm and 115 nm. | 65 |
| 5.11 | Representative plots of EAT along a 6×75 lattice, where $p = 0.6$, $d_{\text{cleft}} = 3.5$ nm and 115 nm. | 66 |
| 5.12 | Representative plots of EAT along a 6×75 lattice, where $p = 0.6$, $d_{\text{cleft}} = 8$ nm and 115 nm. | 67 |
| 5.13 | Representative plots of EAT along a 6×75 lattice, where $p = 0.6$, $d_{\text{cleft}} = 8.5$ nm and 115 nm. | 68 |

Chapter 1

Introduction

The heart is an amazing organ. It is a pump, or two pumps in one, which continuously pumps oxygen and nutrient-rich blood throughout the body to sustain life.

The heart consists of four chambers, two chambers at the top are called the atria. The other two chambers located in the bottom portion of the heart are known as ventricles. Individually, they are named left atrium (LA), right atrium (RA), left ventricle (LV) and right ventricle (RV) based on their locations in the heart. As deoxygenated blood flows into the RA from the body tissues, it passes through the tricuspid valve into the RV, which pumps the blood through the pulmonary valve and through the pulmonary artery to the lungs. The blood is oxygenated and eventually flows back into the LA, and then through the mitral valve, whereupon it enters LV. From there, blood is pumped out through the aortic valve into the aortic arch and onward to the rest of the body. The blood circulation thus continues (Fig. 1.1).

In the light of foregoing, LV is responsible for pumping oxygenated blood to the whole body. By contrast, RV solely pumps blood to the lungs. In other words, ventricles are the main pumping chambers of the heart. Various conditions may affect the ventricles and interfere with their proper functioning. The most serious and commonly identified ventricular arrhythmias is ventricular fibrillation (VF) [1], which causes the heart's lower (pumping) chambers to contract in a rapid, unsynchronized way. The heart pumps little or no blood. Irreversible tissue damage follows.

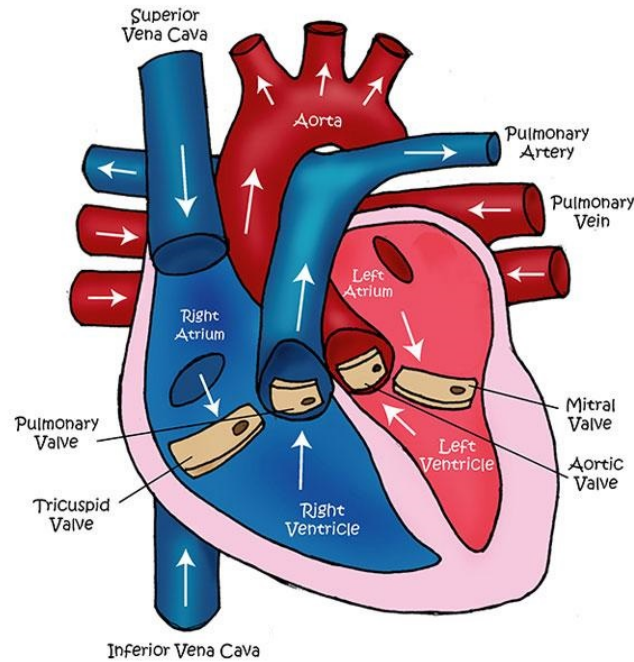


Figure 1.1: Blood circulation in the heart.

In this dissertation, I develop and apply numerical and analytical techniques to study different models, which are primarily related to ventricular arrhythmias, including VF. I also test the models and results against biological experiments. There are several numerical approaches to study the dynamical behaviors of the heart. A biophysically faithful approach is to use a mathematical model to illustrate the complexity and highly interactive nature of the excitation process in a two-dimensional cardiac tissue. In this model, various ionic currents, currents carried by pumps and exchangers, and dynamic changes of ionic concentrations are represented by mathematical equations. This is, in fact, the approach I use in chapters 4 and 5 to study dynamical behaviors during heart failure. However, such models result in a large system of differential equations, and is difficult to analyze mathematically. In chapters 2 and 3, I use a mapping model, a simple but powerful tool to study cardiac dynamics at the level of single cell/cell strand and their relations to VF. A large number of differential equations are replaced by a spatially coupled recurrence relation, which can keep computational cost low,

while retaining some key qualitative features of cardiac dynamics. The outline of the dissertation is as follows:

1.1 The role of short term memory and conduction velocity restitution in alternans formation

In chapter 2, I shall talk about alternans in stimulated cardiac cell and cardiac tissue. Alternans (Fig. 2.2), characterized by a beat-to-beat alternation in action potential duration (APD), is a naturally occurring phenomenon of cardiac cell, which can occur at sufficiently fast pacing rates. Its presence has been putatively linked to the onset of cardiac reentry, which is a precursor to VF [2, 3]. Tissue-level alternans normally arises as spatially concordant alternations, in which long-short alternations in APD are in-phase throughout the tissue. Although this spatially concordant alternans (SCA, Fig. 2.3 A) itself is not believed to be a pro-arrhythmic state, it is usually requisite for progression to so-called spatially discordant alternans (SDA) (Fig. 2.3 B), where regions of long-short APD alternation occur adjacent to regions with short-long APD alternation [4]. It has been mechanistically linked to conduction block and the initiation of reentrant arrhythmias [5]. However, the mechanism behind is still under investigation.

In chapter 3, I will give a detailed description of a mapping model with two beats of memory, with which I explore cardiac dynamics and their link to VF at the level of single cell and cell strand. Indeed, on single cell level, I will investigate the interaction between the two aspects of short term memory (STM) (the dependence of APD on the pacing history) on alternans formation. In a spatially coupled cell strand, I will study the interplay of STM and conduction velocity (CV) restitution (the dependence of CV on the preceding diastolic interval) on SDA formation.

1.2 The dual effect of ephaptic coupling on cardiac conduction with heterogeneous expression of connexin 43

In chapter 4, I shall talk about cardiac action potential propagation at the organ and cellular levels. The ordered stimulation of myocardium during cardiac cycle allows the efficient contraction of the heart, and therefore allows the blood to be pumped

throughout the body. At the organ level (Fig. 4.1), electrical signal arising in the Sinoatrial (SA) node (located in RA) stimulate the atria to contract, and travel to the atrioventricular (AV) node, which is located in the interatrial septum. After a delay, the stimulus diverges and is conducted through the left and right bundle of His to the respective Purkinje fibers for each side of the heart, as well as to endocardium at the apex of the heart, then finally to ventricular epicardium. On the microscopic level, the wave of depolarization propagates to adjacent cells via gap junctions located at the intercalated disc (ID). Gap junctions (Fig. 4.2) are membrane channels that mediate the cell-to-cell movement of ions and small metabolites.

It is widely accepted that gap junctional coupling is the primary mechanism for electrical communication between cardiac cells. However, recent experimental studies in [6, 7] revealed that gap junctions do not tell the complete story of cellular coupling during action potential propagation in the heart. Ephaptic coupling has been suggested as a possible alternative mechanism for cardiac propagation in the near absence of gap junctions [8], which relies on the presence of ID or cleft space between adjacent cardiac cells. When the cleft space is sufficiently narrow (the width of the cleft, d_{cleft} , is sufficiently small), flow of electric current into the cleft may give rise to a local voltage gradient, which may be large enough to allow signal propagation.

Connexin 43 (Cx43) is the major connexin expressed in gap junction channels between ventricular myocytes. Decreased and heterogeneous expression of Cx43 is a common feature during heart failure, which allows for the occurrence of ventricular arrhythmias [9]. Ephaptic coupling has been suggested to play an important role in cardiac propagation when gap junctions are reduced in a homogeneous manner [6, 10, 11, 12]. The interplay of ephaptic and heterogeneous gap junction mediated mechanisms has remained unclear.

In chapter 5, I will model the ephaptic conduction using a two dimensional bidomain approach while Cx43 is reduced in a heterogeneous fashion. I choose Luo-Rudy dynamic guinea pig ventricular model 2007 (LRd 2007) [13] to represent the excitable dynamics of normal cardiac tissue. Under severely reduced Cx43 expressions (Cx43 knockout content is 100%), I identify three new phenomena in the presence of ephaptic coupling: alternating conduction, in which ephaptic and gap junction mediated mechanisms alternate to dominate; Instability of fronts; small amplitude action potential (SAP), which

has a much lower potential amplitude than the normal conduction. When Cx43 expression is heterogeneous, ephaptic coupling can either prevent or promote conduction block (CB) depending on the Cx43 knockout (Cx43KO) content. When Cx43KO content is high, ephaptic coupling reduces the probabilities of CB. However, ephaptic coupling promotes CB when Cx43KO and wild type cells are mixed in roughly equal proportion, which can be attributed to a current-to-load mismatch.

Chapter 2

Cardiac alternans

2.1 Cardiac action potential

Cardiac cells respond to an electrical stimulus by generating an *action potential* [14, 15]. The response consists of a rapid depolarization of the transmembrane potential followed by a much slower repolarization process before returning to the resting value (Fig. 2.1). The time interval during which the potential is elevated is called APD. The amount of time in which the cardiac cell recovers its resting properties before the following stimulus is called diastolic interval (DI). The time interval between two consecutive stimuli is called basic cycle length (BCL) or simply the pacing period. For periodic pacing, $APD + DI = BCL$.

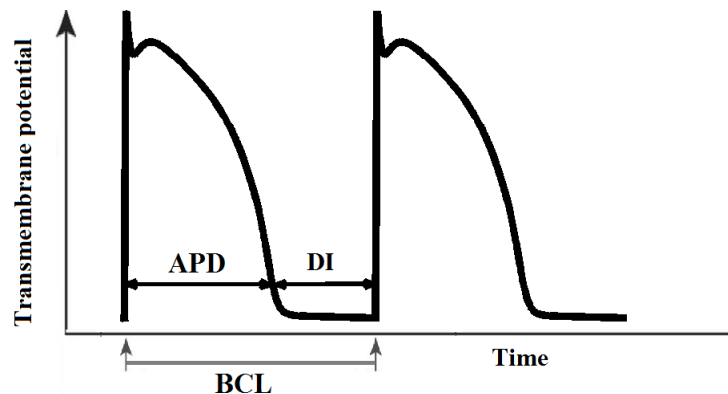


Figure 2.1: Transmembrane potential traces of two action potentials.

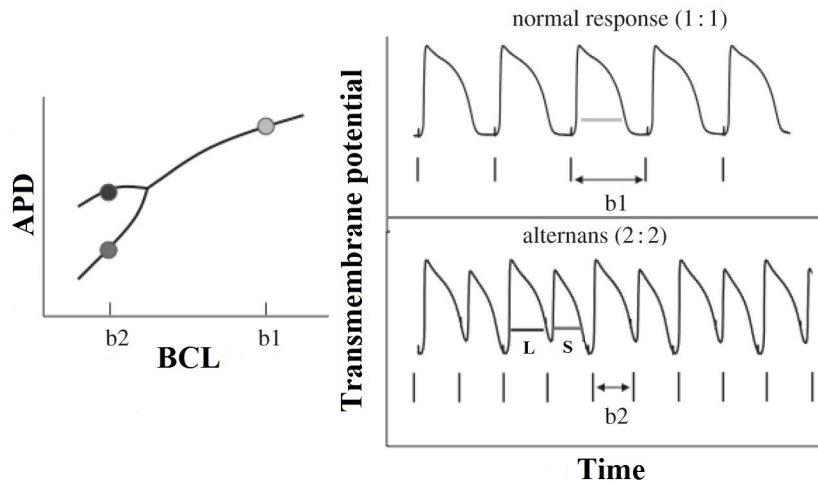


Figure 2.2: APD bifurcation. When BCL is long (e.g. $BCL = b_1$), action potential is locked 1:1 response (upper right). At some point, the BCL becomes short enough (e.g. $BCL = b_2$) that a phase-locked 2:2 pattern emerges and alternans occurs (lower right). Adapted from [16].

2.2 Alternans

VF is a condition in which there is uncoordinated contraction of the cardiac muscle of the ventricles in the heart, making them quiver rather than contract properly. As a result, the heart fails to adequately pump blood. Death can occur in a matter of minutes without cardiopulmonary resuscitation (CPR) or emergency defibrillation and oxygen administration. VF is the most serious and commonly identified ventricular arrhythmia in cardiac arrest patients [1].

Alternans (or the so-called 2:2 response) is a beat-to-beat short-long alternation in the APD of a high frequency periodically stimulated cardiac cell (Fig. 2.2), which has been linked to the genesis of life-threatening VF [2, 3, 17]. In the heart, alternans can be *spatially concordant* or *spatially discordant*. SCA is a phenomenon in which all cells from spatially distinct regions oscillate in phase. For example, all cells display a long-short sequence of APD concurrently. In contrast, SDA is a phenomenon of two spatially distinct regions displaying APD alternans of opposite phases. For example,

some cells display a short-long sequence of APD, the other cells display a long-short sequence. The two regions of opposite phases are separated by a nodal line, in which no alternans is present (Fig. 2.3).

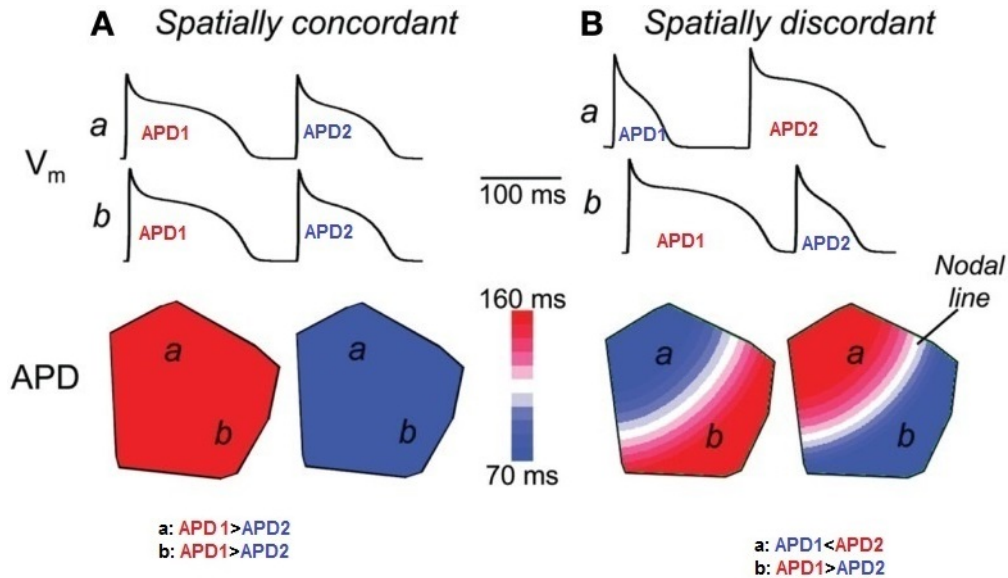


Figure 2.3: Schematic view of SCA (A) and SDA (B) in simulated cardiac tissue. In (A), APD of all myocytes alternate in phase. In (B), the action potentials of adjacent regions of tissue alternate out-of-phase. Indeed, as seen from top traces, the action potentials of site a alternate short-long at the same time as those of site b alternate long-short. As seen in bottom traces, the SDA causes a large gradient in APD across the tissue, with large regions of tissue with counter-phase APD-alternans, separated by a nodal line where alternans is not seen (and where the APD gradient is steepest). Adapted from [18].

SDA has recently been related to T wave alternans (Fig. 2.4), a periodic beat-to-beat variation in the amplitude or shape of the T wave in an electrocardiogram (ECG). T wave alternans is associated with the vulnerability to ventricular arrhythmias and sudden cardiac death [19, 20, 21]. Therefore, it is widely accepted that SDA leads to the formation of steep gradient of refractoriness that can promote the occurrence of wave-break and subsequently, reentry [19, 22, 23] in the heart, and thus it is proarrhythmic.

However, the mechanisms of SDA are not completely understood.

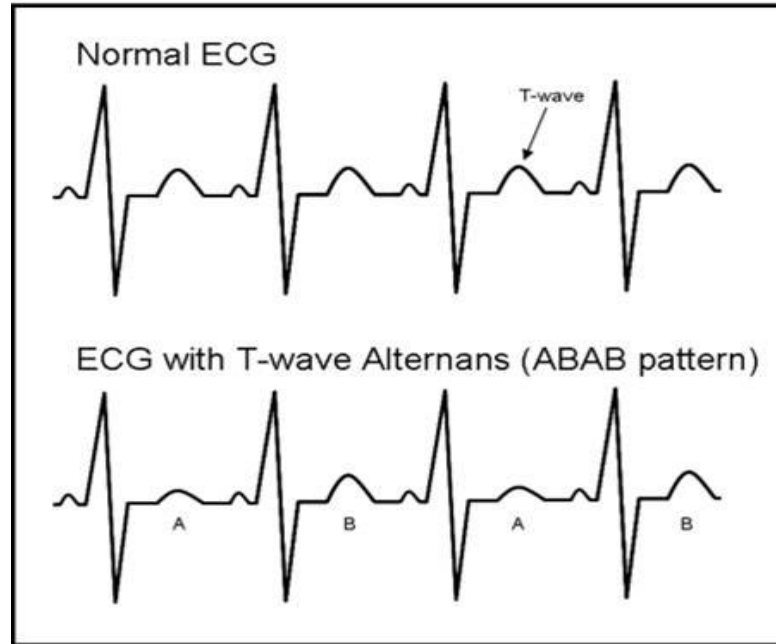


Figure 2.4: Normal T wave and T wave alternans in ECG.

2.3 Overview of SDA studies

Several mechanisms of SDA formation have been proposed. The first mechanism requires preexisting tissue heterogeneities. SDA can be formed via a timed stimulus or faster pacing rate around regions of heterogeneities [19, 24, 25]. However, as indicated in several numerical studies, tissue heterogeneity is not essential for SDA formation [26, 27]. For example, it has been revealed that SDA can form in a perfectly homogeneous tissue via a pure dynamic mechanism [26]. The second proposed mechanism for SDA is a steep CV restitution mechanism, i.e. when CV of a propagating wave has a step dependence on the preceding DI [17, 26, 28, 29, 30]. A third possible mechanism is unstable intracellular calcium cycling, which refers to the steep relation between calcium release versus sarcoplasmic reticulum (SR) calcium load [31]. The last possible

mechanism [32] is STM. The original assumption is that APD depends only on the preceding DI. However, STM implies the dependence of APD on the preceding APD and earlier DIs, thus indicating two beats of memory.

The above four mechanisms of SDA formation in cardiac tissue can be distinguished from the behaviors of nodal lines. Nodal lines formed by tissue heterogeneities are displayed by one of the following two scenarios [33]. First, once a nodal line forms, it can drift away from the pacing site on a beat-to-beat basis without reaching a steady state. Second, the nodal line may reach a steady state but remain pinned as pacing rate increases. In contrast, nodal lines formed by steep CV restitution reach steady state and move towards the pacing site at faster pacing rates [33]. However, nodal lines formed by unstable calcium cycling are not oriented radially with respect to the pacing site, and also does not move in response to changes in pacing rate [34]. On the other hand, it has been suggested that STM is related to unstable behaviors of nodal lines, which means that the nodal lines undergo drifting when pacing rate increases [32].

2.4 Motivation of our study

As discussed above, steep CV restitution and STM are two main mechanisms in SDA formation. However, in experiments, it is difficult to identify the role of each. In addition, the interplay between these two mechanisms is still unclear. In the following chapter, I will explore the interplay of CV restitution and STM on alternans formation via a mapping model with two beats of memory.

Chapter 3

The role of short term memory and conduction velocity restitution in alternans formation.

In this chapter, we aim to uncover the mechanisms of SDA formation using numerical simulations of a mapping model with two beats of memory that is introduced in [35]. This is a rather simple yet powerful tool to determine the contributions of STM to alternans formation in single cell. In addition, to identify the individual contribution of STM and CV restitution to SDA formation, we perform numerical simulations of the mapping model in a homogeneous cable. The main results of this chapter have been published in [36] joint with Prof. Yoichiro Mori and Prof. Elena G. Tolkacheva.

We adopt the mapping model in the following form [35]:

$$A_{n+1} = F(D_n, A_n, D_{n-1}), \quad (3.1)$$

where A_n and D_n are APD and DI at the n^{th} stimulus. Note that, in Eq. (3.1), APD depends not only on the preceding DI, but also on the previous APD and earlier DI, which indicates the presence of two beats of STM in the model. We consider the case of periodic pacing of constant basic cycle length (BCL), for which relation $A_n + D_n = \text{BCL}$ holds.

3.1 Materials and Methods

3.1.1 Mapping model with two beats of memory

For exact form of Eq. (3.1), we use a mapping model that is introduced in [37]:

$$A_{n+1} = (1 - \alpha M_{n+1})G(D_n), \quad (3.2a)$$

$$M_{n+1} = [1 - (1 - M_n)\exp(-A_n/\tau)]\exp(-D_n/\tau), \quad (3.2b)$$

where

$$G(D_n) = Q + \frac{R}{1 + \exp(-(D_n - S)/T)}$$

and α and τ are two aspects of STM, which represent rate-dependent restitution and APD accommodation, respectively. Rate-dependent restitution is measured as the difference between slopes of different restitution curves calculated at the same BCL [38]. APD accommodation refers to the slow change of APD over time after an abrupt change in BCL. Note that, large α refers to more disparity between APD restitution curves, and large τ refers to more APD accommodations. We choose the following parameters in Eq. (3.2),

$$Q = 115 \text{ ms}, R = 121 \text{ ms}, S = 42.5 \text{ ms}, T = 20.2 \text{ ms},$$

since these values allow the mapping model to fit with the steady state solutions from a physiological model of action potential.

In order to investigate the effect of STM on alternans formation using mapping model Eq. (3.2), we vary α from 0 to 1 and choose three different values of τ : 11.4 s (large APD accommodation), 260 ms and 200 ms (small APD accommodation).

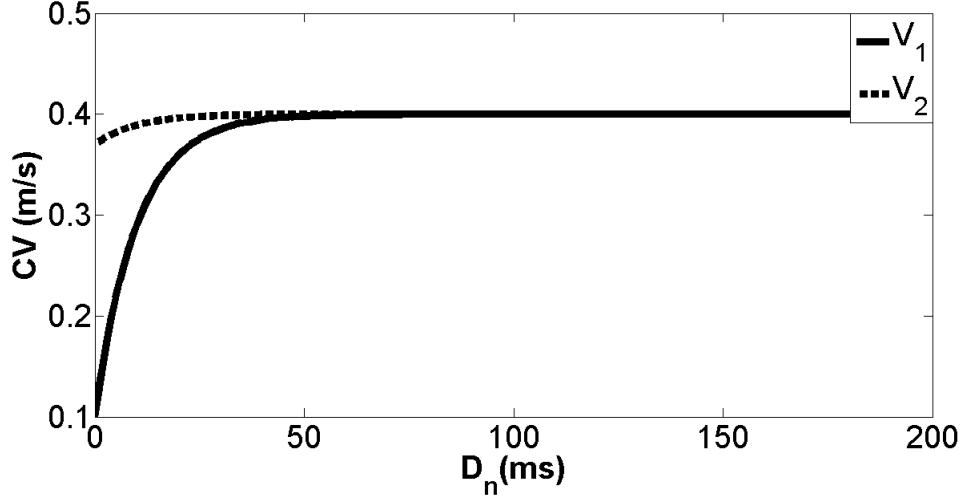


Figure 3.1: CV as a function of D_n , for steep restitution curves V_1 (solid) and shallow V_2 (dashed).

3.1.2 Spatially coupled mapping model

In order to model a one dimensional cable, we adopt a spatially coupled mapping model Eq. (3.3) by adding diffusion and advection terms to Eq. (3.1), as suggested in [39]:

$$A_{n+1} = F(D_n, A_n, D_{n-1}) + \xi^2 \nabla^2 A_{n+1} - \omega \nabla A_{n+1}, \quad (3.3)$$

where $\xi = 1, \omega = 0.35$. The choices of ξ and ω are based on [39, 40], and detailed justification can be seen in Appendix. Here, the diffusion term $\xi^2 \nabla^2 A_{n+1}$ represents the coupling between cells, and the advection term $-\omega \nabla A_{n+1}$ depicts the asymmetry of influence by its left and right neighbors, considering that cells are activated at different times by the propagating wave front [40, 41]. The distribution of $D_n(x)$, the n^{th} DI along the cable has been described in [26]:

$$\frac{dD_n(x)}{dx} = \frac{1}{V(D_n(x))} - \frac{1}{V(D_{n-1}(x))} - \frac{dA_n(x)}{dx}, \quad (3.4)$$

where x is the position along the cable and V represents a CV restitution curve. Note that, $A_n(0) + D_n(0) = \text{BCL}$. We combine Eq. (3.3) with Eq. (3.4) to solve A_{n+1} along a cable with length $L = 4$ cm, [39]. Due to the finite length of the cable, we

impose the Neumann boundary condition, $\frac{\partial A_{n+1}}{\partial x}|_{x=0,L} = 0$, on the two ends of the cable to minimize the boundary effect. To investigate the effect of CV restitution on SDA formation, we use steep (V_1) and shallow (V_2) restitution curves, as shown in Fig. 3.1,

$$\begin{aligned} V_1(D_n) &= 0.4 - 0.3\exp(-D_n/10), \\ V_2(D_n) &= 0.4 - 0.03\exp(-D_n/10). \end{aligned} \tag{3.5}$$

We discretize Eqs. (3.3) and (3.4) along a cable with length L by the following scheme at a spatial step size ($\Delta x = \frac{L}{N}$) of 0.01 cm.

$$\begin{aligned} & -\frac{\xi^2}{\Delta x^2}A_{n+1}(x_{i-1}) + (1 + 2\frac{\xi^2}{\Delta x^2} - \frac{\omega}{\Delta x})A_{n+1}(x_i) - (\frac{\xi^2}{\Delta x^2} - \frac{\omega}{\Delta x})A_{n+1}(x_{i+1}) \\ & = F(D_n(x_i), A_n(x_i), D_{n-1}(x_i)), \quad i = 1 \cdots N, \end{aligned}$$

$$A_{n+1}(x_0) = A_{n+1}(x_1), \quad A_{n+1}(x_N) = A_{n+1}(x_{N+1}).$$

$$D_n(x_i) = \text{BCL} + \sum_{j=0}^{i-1} \frac{\Delta x}{V(D_n(x_j))} - \sum_{j=0}^{i-1} \frac{\Delta x}{V(D_{n-1}(x_j))} - A_n(x_i),$$

where x_i is the i^{th} site along the cable, $\Delta x = x_i - x_{i-1}$.

3.1.3 Pacing protocols

In order to study the mechanism of alternans formation after an abrupt change in pacing rate, BCL is decreased from $\text{BCL}_1 = 500$ ms to a different BCL_2 , ranging from 100 ms to 300 ms. We apply 300 stimuli at BCL_1 and sufficient number of stimuli to reach steady state at BCL_2 .

In the cable, pacing is applied at the left end $x = 0$, and the following parameters are recorded: steady state positions of nodes (X_{ss}) and time to reach steady state of the nodes (t_{ss}) at BCL_2 . Here, X_{ss} is defined as a point for which APD node drifts less than 0.1 mm for the ten consecutive stimuli. t_{ss} is recorded from the beginning of pacing at BCL_2 until steady state is reached. (See Table 3.1 for details.)

Table 3.1: Parameters Abbreviations.

| Parameter | Meaning | Value |
|--------------------|---|--|
| D_{\min} | minimum DI for which action potential can be initiated. | 2 ms |
| BCL_1 | Initial BCL in the pacing protocol. | 500 ms |
| BCL_2 | Second BCL in the jump pacing protocol. | 100 ms to 300 ms |
| X_{ss} | Steady state positions of nodes in the cable. | |
| t_{ss} | Time to steady state of the nodes in the cable. | |
| A_1^{thr} | Threshold for APD without overpacing. | $A_1^{\text{thr}} = BCL_2 - D_{\min}$. |
| A_2^{thr} | Threshold for APD including overpacing. | $A_2^{\text{thr}} = 2BCL_2 - D_{\min}$. |
| CB | Conduction block in the single cell or cable. | |
| CB ₁ | Type I conduction block in the cable. (Block occurs at $x = 0$). | |
| CB ₂ | Type II conduction block in the cable. (Block occurs at $x \neq 0$). | |
| V_1 | Steep CV restitution curve. | $V_1 = 0.4 - 0.3\exp(-DI/10)$. |
| V_2 | Shallow CV restitution curve. | $V_2 = 0.4 - 0.03\exp(-DI/10)$. |
| x | Position in the cable. | |
| L | Length of the cable. | 4 cm |

3.1.4 Overpacing and conduction block

One of the general limitations of the mapping model is that in a single cell, APD computed using Eq. (3.2) may be larger than $BCL - D_{\min}$, where $D_{\min} = 2$ ms is the minimum DI for which an action potential can be initiated [29, 39, 42]. Slight changes in D_{\min} do not affect our results significantly. If $DI < D_{\min}$, then the cell does not produce an action potential, which will lead to a 2:1 response provided $APD < 2BCL - D_{\min}$. However, if the cell is further stimulated, it may recover from 2:1 back to 1:1 or 2:2

responses. This phenomenon is known as overpacing, and it is shown in Fig. 3.2A.

Fig. 3.2A illustrates responses of mapping model Eq. (3.2) when BCL is decreased from BCL_1 to BCL_2 . The $(n-1)^{\text{th}}$ and n^{th} stimuli give rise to action potentials, while the $(n+1)^{\text{th}}$ stimulus fails to produce an action potential, since $A_n > A_1^{\text{thr}} = BCL_2 - D_{\min}$. However, if $A_n < A_2^{\text{thr}} = 2BCL_2 - D_{\min}$, then the $(n+2)^{\text{th}}$ stimulus will be able to produce an action potential, and

$$\begin{aligned} D_{n+1} &= 2BCL_2 - A_n, \\ A_{n+2} &= F(D_{n+1}, A_n, D_{n-1}). \end{aligned} \tag{3.6}$$

If a cell cannot recover from 2:1 response as a result of overpacing, we define it as conduction block (CB) for single cell. In general, a $k : 1 (k > 2)$ response may be possible if $APD > A_2^{\text{thr}}$.

The effect of overpacing on single cell dynamics for the mapping model Eq.(3.2) when BCL is changed from BCL_1 to $BCL_2 = 170$ ms is demonstrated in Fig. 3.3. It shows an example of CB (A) and transition from 2:1 to 1:1 responses (B) as a result of overpacing. Here, $\alpha = 0.1$ (A), $\alpha = 0.6$ (B) and $\tau = 11.4$ s. As observed in Fig. 3.3A, APDs (open circles) are always greater than A_1^{thr} (dashed line) but less than A_2^{thr} (dashed line), indicating a sustained 2:1 response.

In contrast, in Fig. 3.3B, APDs are greater than A_1^{thr} and less than A_2^{thr} at the beginning of pacing at BCL_2 . But with continued pacing, APD becomes less than A_1^{thr} , thus indicating the transition from 2:1 response to 1:1 behavior can only be observed in the presence of overpacing.

In a cable, one may have $D_n(x) \geq D_{\min}$ for certain x , whereas $D_n(x) < D_{\min}$ for other x . Several scenarios of dealing with CB and overpacing in the cable have been discussed in the literature. For example, in [42], the authors developed a method that uses the APD and CV restitution relations to generate predictions regarding which sequences of premature stimuli are most likely to induce type II CB and reentry. Specifically, block occurs when the trailing edge of the preceding wave travels slower than the leading edge of the current wave, allowing the latter to encroach and terminate on the former. In [39], simulation is terminated once $D_n(x) < D_{\min}$ occurred for any x in the cable. In [29], overpacing is considered for a cable consisting of a simple mapping model without memory, $A_{n+1} = f(D_n)$.

In this chapter, we implement overpacing in the cable for the mapping model with two beats of STM by using the approach shown in Fig. 3.2B, which illustrates responses of spatially coupled mapping model Eq. (3.3) when the cable is paced at $x = 0$ and BCL is decreased from BCL_1 to BCL_2 . As observed, solid and dashed lines represent the wavefront and waveback of an action potential along the cable, respectively. Let x^* be the maximal value such that

$$\widetilde{D}_n(x) \geq D_{\min}, \text{ for } x < x^*, \quad (3.7)$$

where $\widetilde{D}_n(x)$ satisfies the following:

$$\frac{d\widetilde{D}_n(x)}{dx} = \frac{1}{V(\widetilde{D}_n(x))} - \frac{1}{V(D_{n-1}(x))} - \frac{dA_n(x)}{dx},$$

$$A_n(0) + \widetilde{D}_n(0) = \text{BCL}.$$

Then we let $D_n(x) = \widetilde{D}_n(x)$ for $x < x^*$, where $D_n(x)$ is the n^{th} DI. That is, the $(n+1)^{\text{th}}$ action potential can only propagate to x^* . Therefore, $A_{n+1}(x)$ also exists for $x < x^*$ (we let $A_{n+1} = 0$ for $x \geq x^*$ to emphasize).

Let us consider the situation when the $(n+2)^{\text{th}}$ action potential can propagate to the end. For $x < x^*$, $D_{n+1}(x)$ and $A_{n+2}(x)$ can be obtained by Eqs. (3.3) and (3.4). For $x \geq x^*$, $D_{n+1}(x)$ and $A_{n+2}(x)$ can be obtained by Eq. (3.8) below.

$$\frac{dD_{n+1}(x)}{dx} = \frac{1}{V(D_{n+1}(x))} - \frac{1}{V(D_{n-1}(x))} - \frac{dA_n(x)}{dx}, \quad (3.8)$$

$$A_{n+2} = F(D_{n+1}, A_n, D_{n-1}) + \xi^2 \nabla^2 A_{n+2} - \omega \nabla A_{n+2},$$

where $D_{n+1}(x)$ is the DI that follows either $A_{n+1}(x)$ (for $x < x^*$) or $A_n(x)$ (for $x \geq x^*$). If the action potential cannot propagate to the end of the cable, CB occurs. Moreover, if CB occurs at $x = 0$, we define it as type I CB (CB₁). If CB occurs at $x \neq 0$, we define it as type II CB (CB₂).

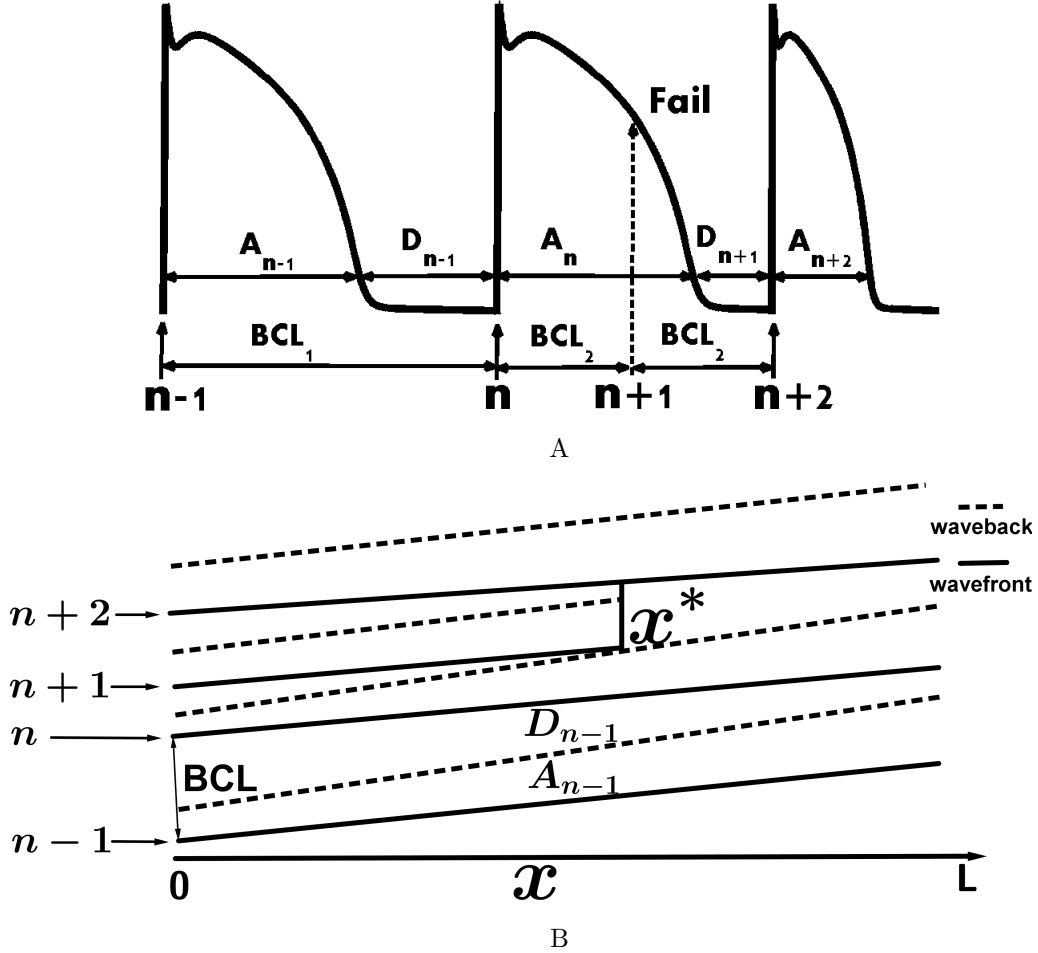
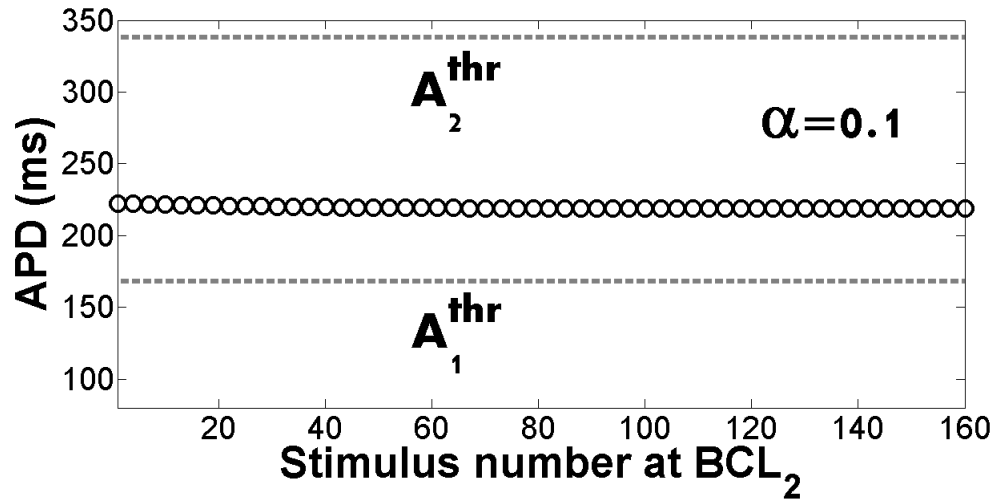
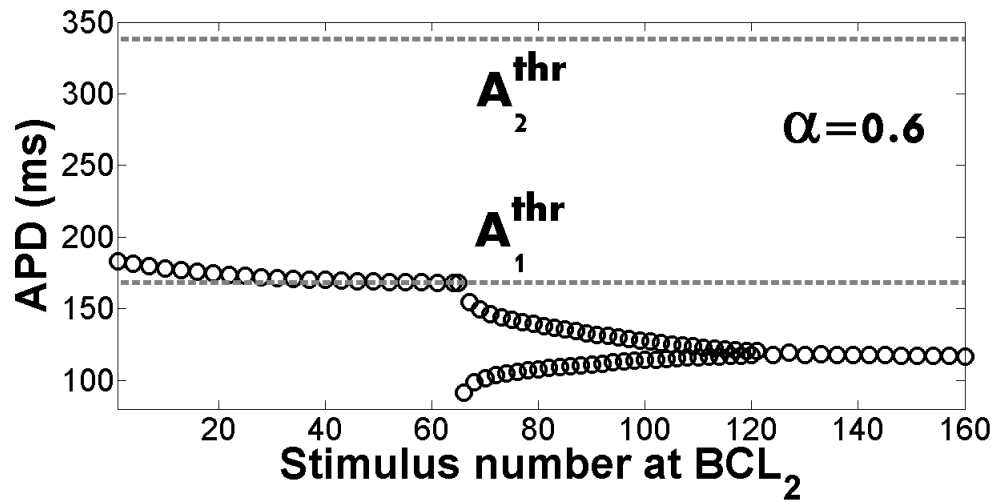


Figure 3.2: Overpacing of single cell (A) and cable (B). In A, action potentials are shown for pacing protocol in which BCL is changed from BCL_1 to BCL_2 . Note that, $(n-1)^{th}$ and n^{th} stimuli produce action potentials, but the $(n+1)^{th}$ stimulus (dashed vertical line) fails to produce an action potential. However, if the $(n+2)^{th}$ beat produces an action potential, then D_{n+1} and A_{n+2} can be obtained by Eq. (3.6). In B, solid and dashed lines represent the wavefront and waveback of an action potential, respectively. The $(n-1)^{th}$ and n^{th} stimuli produce action potentials that propagate to the end of the cable. But the $(n+1)^{th}$ action potential can only be delivered for $x < x^*$, i.e. CB occurs at $x = x^*$. Note that, the $(n+2)^{th}$ action potential can propagate to the end of the cable.



A



B

Figure 3.3: CB (A) and overpacing leading to transition from 2:1 to 1:1 in single cell (B). APD (open circle) is displayed versus stimulus number at BCL_2 when BCL is changed from $BCL_1 = 500$ ms to $BCL_2 = 170$ ms. Here, $\alpha = 0.1$ (A), $\alpha = 0.6$ (B) and $\tau = 11.4$ s. Dashed lines represent $A_1^{\text{thr}} = BCL_2 - D_{\text{min}}$ and $A_2^{\text{thr}} = 2BCL_2 - D_{\text{min}}$.

3.2 Results

3.2.1 Dynamical responses of single cell

We first aim to classify different dynamical behaviors of the mapping model Eq. (3.2) at steady state (i.e. 1:1, 2:2, or CB) when BCL is changed from BCL_1 to various BCL_2 . Fig. 3.4 illustrates steady state responses at different BCL_2 as a function of α for $\tau = 11.4$ s (A), $\tau = 260$ ms (B), and $\tau = 200$ ms (C). Black dashed lines outline the regions for 1:1 responses (filled circles or upper right corner regions labeled as 1:1) and CB. For $\tau = 11.4$ s and 260 ms (Figs. 3.4A and 3.4B), we can see that when BCL_2 is large, only 1:1 responses are observed. As BCL_2 decreases, CB or 2:2 (or alternans) (crosses) behaviors occur, which transition to 1:1 responses as α increases. Once BCL_2 becomes sufficiently small, only CB is observed.

Fig. 3.4C shows different dynamical responses of the mapping model Eq. (3.2) for $\tau = 200$ ms. Here, we can see a larger region occupied by alternans (crosses), especially for large α . These results suggest that the effect of α is diminished as τ decreases.

The dynamical behaviors of a single cell are different for high and low values of τ . The cases $\tau = 11.4$ s and $\tau = 200$ ms are two representatives of the respective regimes. The high τ regime extends to about 290 ms and the low τ regime extends to around 250 ms. There is a narrow transition regime between $\tau = 250$ ms and $\tau = 290$ ms, for which we showed the case $\tau = 260$ ms.

The individual roles of α and τ in alternans formation can be understood by considering the limit of M_{n+1} as τ approaches zero. Eq. (3.2b) yields $\lim_{\tau \rightarrow 0} M_{n+1} = \lim_{\tau \rightarrow 0} [1 - (1 - M_n)\exp(-A_n/\tau)]\exp(-D_n/\tau) = 0$, since $A_n, D_n > 0$. Then Eq. (3.2a) reduces to $A_{n+1} = G(D_n)$, i.e. no memory. Thus, effect of α is diminished as τ decreases.

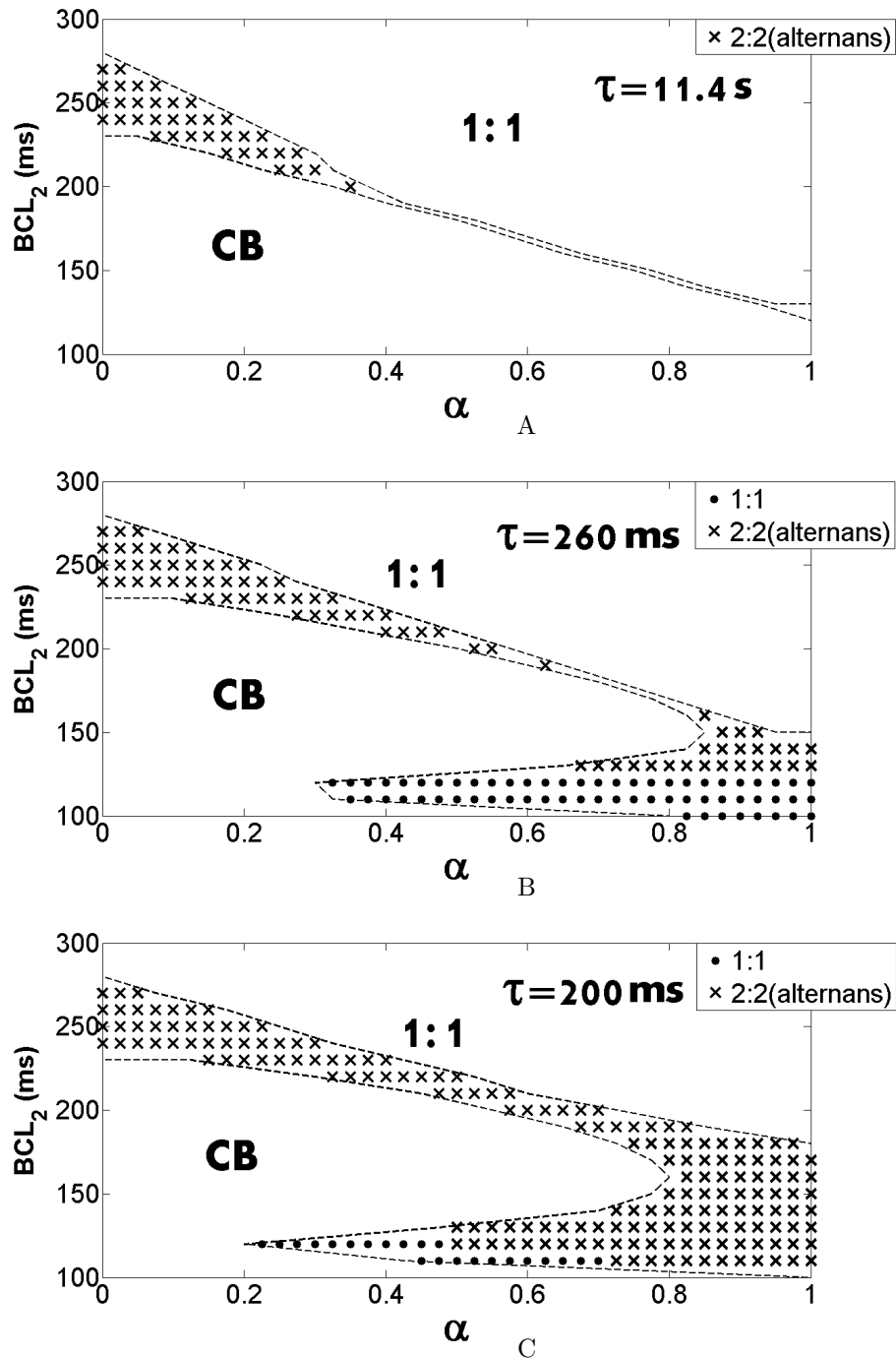


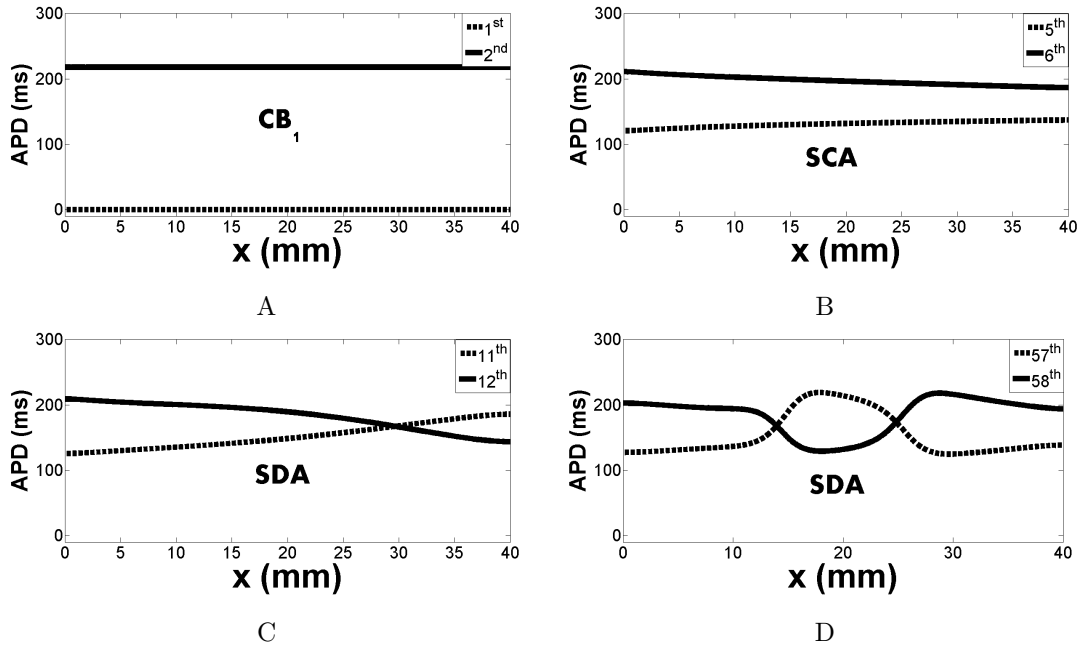
Figure 3.4: Dynamic responses of single cell at steady state as a function of α when BCL is decreased from BCL_1 to different BCL_2 for $\tau = 11.4$ s (A), $\tau = 260$ ms (B), and $\tau = 200$ ms (C). Behaviors are classified as 1:1 (filled circles or upper right corner regions labeled as 1:1), 2:2 (or alternans) (crosses) and CB.

3.2.2 SDA in spatially coupled mapping model

Effect of overpacing on CB

We find that the effect of overpacing has more important consequences on dynamics in the cable, in comparison to the single cell. To illustrate it, we perform numerical simulations of spatially coupled mapping model Eq. (3.3) when BCL is decreased from BCL_1 to BCL_2 . Figs. 3.5A – 3.5E show results for different stimulus number at $BCL_2 = 220$ ms, $\alpha = 0.175$, $\tau = 11.4$ s and $CV = V_1$. As observed, Fig. 3.5A demonstrates that CB_1 occurs at the first beat as BCL is decreased to BCL_2 , after which SCA (Fig. 3.5B) and SDA (Figs. 3.5C and 3.5D) occur sequentially. SDA persists for about 40 beats, and then CB_2 (Fig. 3.5E) is observed at the 59th beat, at which action potential is blocked in the middle of the cable.

In Fig. 3.5F, we set $BCL_2 = 190$ ms, $\alpha = 0.425$, $\tau = 11.4$ s and $CV = V_1$. As stimuli number increases, we observe a transition from CB_1 (dashed line) to SDA (open and filled circles) and then to 1:1 (grey line) behavior under overpacing. Note that, neither the transition from CB_1 to CB_2 nor the transition from CB_1 to SDA and then to 1:1 response can be observed without overpacing. Instead, simulations would have terminated at the first beat.



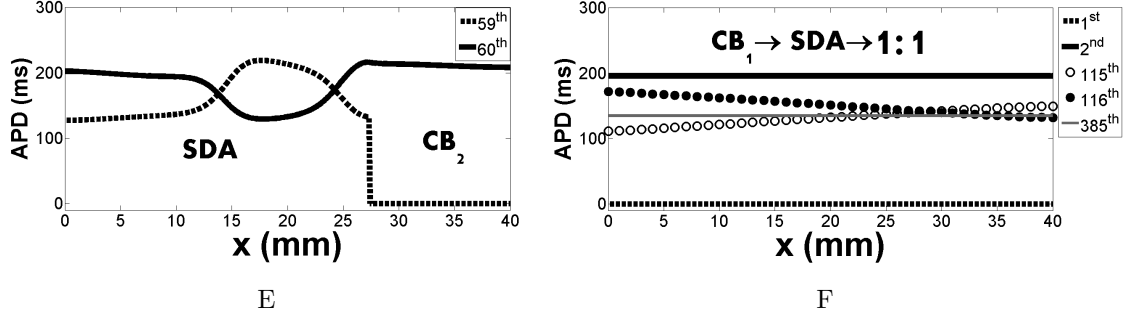


Figure 3.5: Effect of overpacing in cable. Transition from CB_1 (A) to SCA (B) and SDA (C, D) and then to CB_2 (E) as BCL is decreased from BCL_1 to $BCL_2 = 220$ ms. Here, $\alpha = 0.175$, $\tau = 11.4$ s and $CV = V_1$. Transition (F) from CB_1 to SDA and then to 1:1 response as BCL is decreased from BCL_1 to $BCL_2 = 190$ ms. Here $\alpha = 0.425$, $\tau = 11.4$ s and $CV = V_1$.

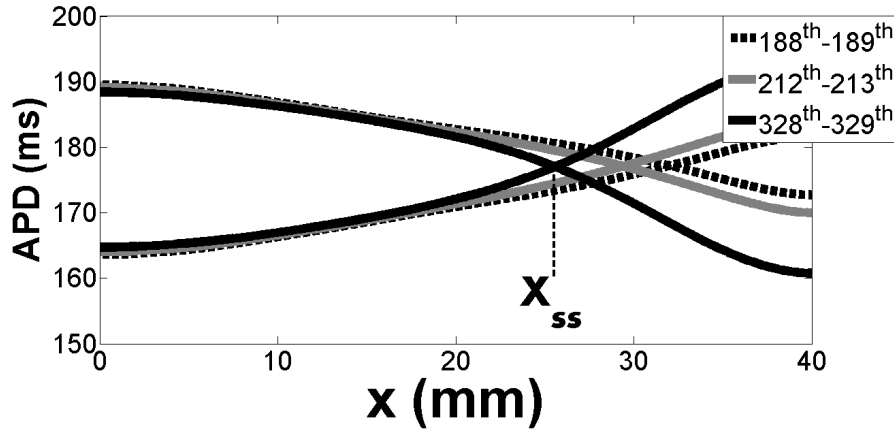
SDA node behaviors while approaching steady state

We observe two different behaviors of SDA nodes while approaching steady state: stable and unstable node formation. Fig. 3.6A shows stable behavior of nodes for the spatially coupled mapping model Eq. (3.3) when BCL is decreased from BCL_1 to $BCL_2 = 240$ ms, $\alpha = 0.175$, $\tau = 11.4$ s and $CV = V_1$. Note that the node formed by the 188th and 189th beats (black dashed) appears at the distal end of the cable and then moves towards (grey and black nodes) the pacing site $x = 0$ as it approaches steady state X_{ss} .

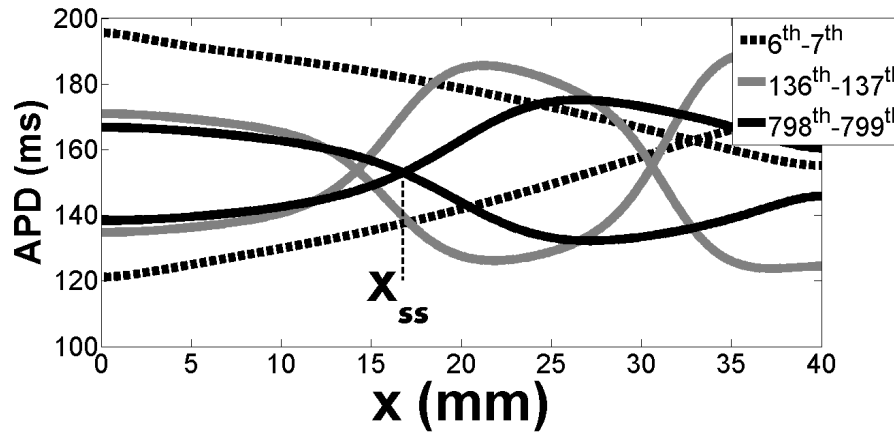
Fig. 3.6B shows unstable behavior of the node for the spatially coupled mapping model Eq. (3.3) when BCL is decreased from BCL_1 to $BCL_2 = 210$ ms, $\alpha = 0.3$, $\tau = 11.4$ s and $CV = V_1$. The node formed by the 6th and 7th beats (black dashed) appears at the end of the cable and migrates towards (grey solid) the pacing site $x = 0$ first, and then away from (black solid) the pacing site $x = 0$ as it approaches steady state X_{ss} .

For the stable nodes, we calculate the steady state positions (X_{ss}) and time to reach steady state (t_{ss}). Figs. 3.7A and 3.7B are representative examples displaying X_{ss} and t_{ss} as a function of α respectively. Both figures are obtained for the spatially coupled mapping model Eq. (3.3) when BCL is changed from BCL_1 to $BCL_2 = 130$ ms, where $\tau = 200$ ms and $CV = V_1$. As depicted, X_{ss} increases as α increases and t_{ss} first

decreases and then increases. Our results show that increase of α could result in steady state nodes being further away from pacing site. Nevertheless, there appears to be a minimum t_{ss} as α is varied in Fig. 3.7B.

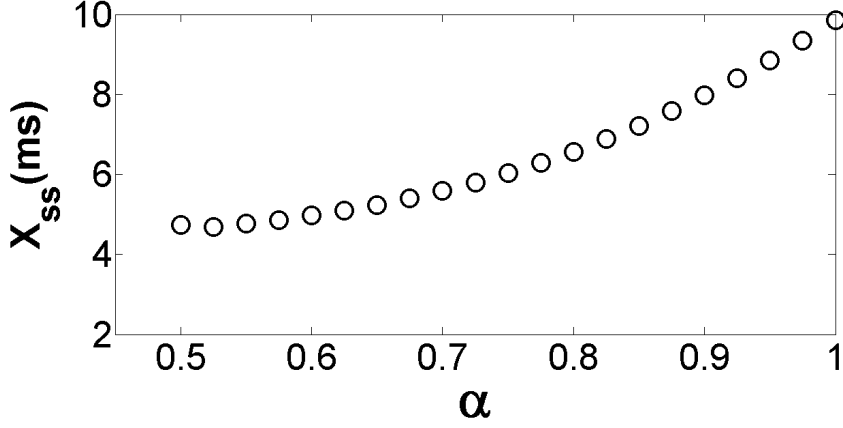


A

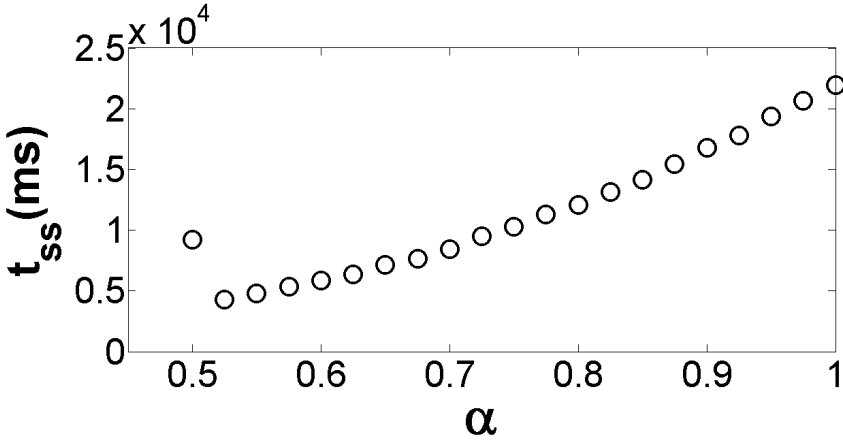


B

Figure 3.6: Stable (A) and unstable (B) SDA nodal behaviors. APD of selective beats are displayed versus cable length when BCL is decreased from BCL_1 to $BCL_2 = 240$ ms (A) and $BCL_2 = 210$ ms (B), $\alpha = 0.175$ (A), $\alpha = 0.3$ (B), $\tau = 11.4$ s and $CV = V_1$ (steep CV restitution).



A



B

Figure 3.7: X_{ss} and t_{ss} as a function of α for stable nodes when BCL is decreased from BCL_1 to $BCL_2 = 130$ ms, $\tau = 200$ ms and $CV = V_1$ (steep CV restitution).

Interplay between CV restitution and STM

Finally, we aim to characterize different dynamical behaviors of the spatially coupled mapping model Eq. (3.3) at steady state when BCL is changed from BCL_1 to various BCL_2 . Fig. 3.8 illustrates steady state responses at different BCL_2 as a function of α for V_2 (shallow CV restitution), $\tau = 11.4$ s (A), $\tau = 260$ ms (B), $\tau = 200$ ms (C) and for V_1 (steep CV restitution), $\tau = 11.4$ s (D), $\tau = 260$ ms (E), $\tau = 200$ ms (F). As

observed in Figs. 3.8A – 3.8C, at $CV = V_2$, steady state behaviors in the cable look very similar to those of single cell if SDA (cross) and SCA (square) are considered as alternans, since single cells cannot exhibit spatial phenomena.

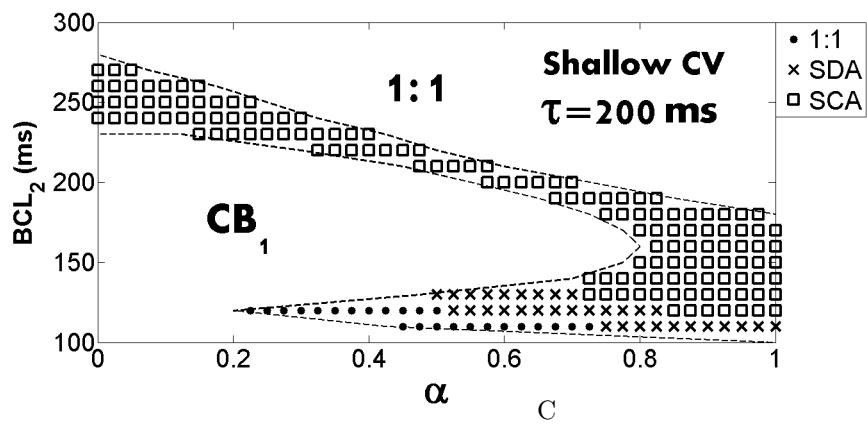
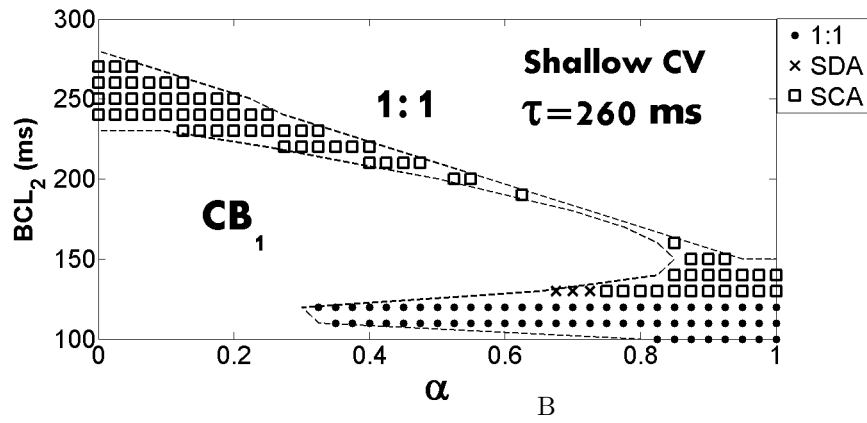
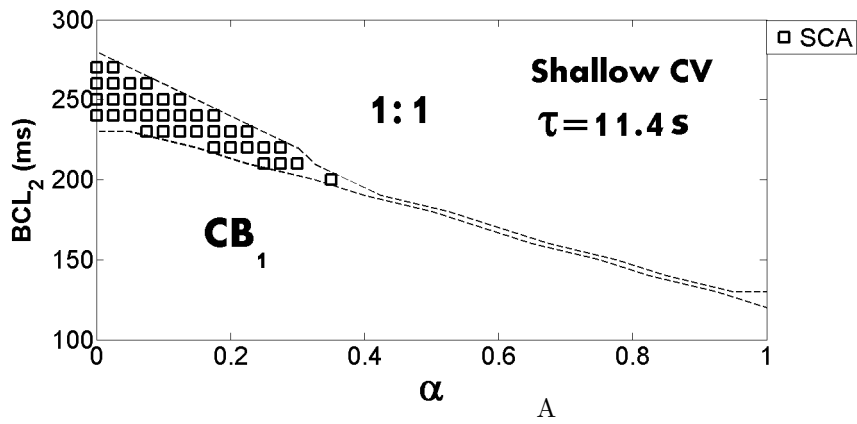
Figs. 3.8A and 3.8D illustrate that for $\tau = 11.4$ s, steep CV restitution (V_1 , Fig. 3.8D) leads to appearance of more complicated dynamical responses, such as CB_2 (diamond) (Fig. 3.5E), transition from CB_1 to CB_2 (star, $CB_1 \rightarrow CB_2$) (Figs. 3.5A – 3.5E) and unstable nodes (plus, unstable) (Fig. 3.6B).

However, Figs. 3.8B, 3.8C, 3.8E, 3.8F illustrate that for $\tau = 260$ ms and 200 ms, the effect of steep CV restitution curves is negligible, except more formation of SDA, including the region of large α .

Furthermore, Figs. 3.8D and 3.8F illustrate that for V_1 , smaller τ (200 ms) leads to appearance of simpler dynamical responses, such as the inhibition of CB_2 (diamond), transition from CB_1 to CB_2 (star, $CB_1 \rightarrow CB_2$), and unstable nodes (plus, unstable).

Similar to the single cell case, the dynamical behaviors of the cable are different for high and low values of τ . The cases $\tau = 11.4$ s and $\tau = 200$ ms are two representatives of the respective regimes. We also show results for $\tau = 260$ ms, at which the behavior is intermediate between the two regimes.

Our results indicate that shallow CV restitution together with large τ can help suppress SDA. Steep CV restitution coupled with large τ gives rise to CB_2 , the transition from CB_1 to CB_2 and unstable nodes, which are inhibited by either shallow CV or small τ . Steep CV restitution together with small τ can lead to more formation of SDA, including the region of large α . Our result also indicates that STM plays a dominant role in SDA formation.



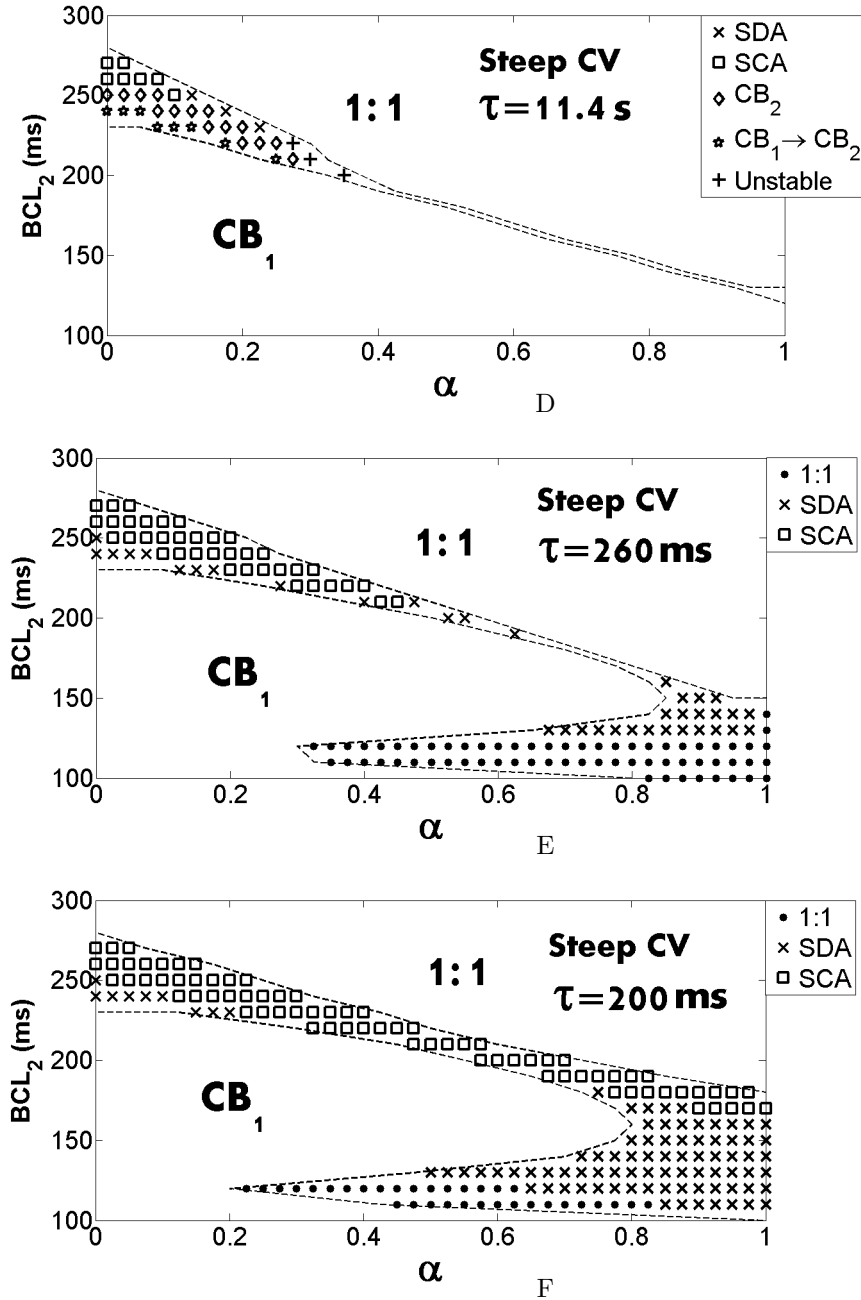


Figure 3.8: Dynamical responses of the cable at steady state as a function of α when BCL is changed from BCL_1 to different BCL_2 for $CV = V_2$, $\tau = 11.4$ s (A), $\tau = 260$ ms (B) and $\tau = 200$ ms (C); $CV = V_1$, $\tau = 11.4$ s (D), $\tau = 260$ ms (E), $\tau = 200$ ms (F). Behaviors are classified as 1:1 response (filled circle or upper right corner regions labeled as 1:1), SDA (cross), SCA (square), CB_1 , CB_2 (diamond), transition from CB_1 to CB_2 (star, $CB_1 \rightarrow CB_2$) and unstable nodes (plus, unstable).

3.3 Conclusion and discussions

In this chapter, we investigate the effect of two aspects of STM (α , τ) and their interplay with CV restitution on alternans formation using numerical simulations of a mapping model with two beats of memory. In both single cell and spatially coupled homogeneous cable, the interplay between α and τ affects the dynamical behaviors of the system. For the case of large APD accommodation ($\tau \geq 290$ ms), an increase in α leads to suppression of alternans. However, if APD accommodation is small ($\tau \leq 250$ ms), an increase in α leads to appearance of additional alternans region. On the other hand, the slope of CV restitution does not change the regions of alternans in the cable. However, steep CV restitution leads to more complicated dynamical behaviors of the system. Specifically, SDA instead of SCA are observed. In addition, for steep CV restitution and sufficiently large τ , we observe formations of CB_2 , transition from CB_1 to CB_2 , and unstable nodes.

To our knowledge, this is the first use of overpacing in a mapping model with two beats of memory. At the single cell level, the cell may recover from 2:1 rhythm back to 1:1 or 2:2 rhythm if the cell is stimulated beyond the beat at which $DI < D_{\min}$. The same can be said of the cable. This indicates the importance of pacing beyond conduction block. In [39], stimulation is terminated once $DI(x) < D_{\min}$ for any x in the cable. In [29], overpacing is adopted using a simple mapping model without memory; APD only depended on the preceding DI, making it relatively simple to implement overpacing. Here, we overpace the cable in a mapping model with two beats of memory. The dependence of APD on the preceding APD and two preceding DIs gives rise to new difficulties in the continuation of pacing after $DI < D_{\min}$ for any x in the cable. The resolution of this difficulty is a technical contribution of our paper. Our use of continued pacing has allowed us to observe recoveries from CB_1 to 1:1 responses or SDA and transitions from CB_1 to CB_2 that we would not have been able to see otherwise.

This is the first study in which a mapping model with two beats of memory has been used to investigate SDA formation. Over the last decades, the study of SDA has become a major focus of research because of its potentially crucial link to cardiac instability. Our numerical results are in agreement with previous experimental and theoretical studies of SDA. We confirm that SDA can be observed in a homogeneous

cable [26, 27], and that steep CV restitution facilitates SDA [17, 26, 28, 29, 30]. We also find that small τ , together with steep CV restitution, further facilitates SDA formation. This agrees with the experimental results in [32] which states that stable SDA nodal lines were associated with steep CV restitution and small τ . Finally, we demonstrate that unstable behaviors of nodes is related to steep CV restitution and large τ . This is consistent with experimental results in [32], wherein the unstable drifting behaviors of nodal lines during adaptation to change in BCL are seen for large values of τ .

One limitation of our study is that we choose $D_{\min} = 2$ ms. However, our simulation results demonstrate that sufficiently large increases in D_{\min} might affect the dynamic behaviors of the cable model. Specifically, for $D_{\min} = 20$ ms, $\tau = 11.4$ s and $CV = V_1$ (steep CV restitution), we observe more incidences of CB_1 as well as transitions from SCA or SDA to CB_2 , the latter of which are not present for $D_{\min} = 2$ ms.

Another limitation of our study is that we choose the cable length L to be 4 cm with 401 cells. It is clear that we will see more incidences of SDA and nodes in a larger domain. However, if simulations are performed on a larger domain with length $L > 4$ cm, but the dynamical behaviors are only tracked on the first 4 cm segment of the simulation domain, we have checked that the simulation results are similar to the case when $L = 4$ cm. This indicates that the boundary conditions at $x = L$ do not appreciably affect the results of the simulation.

Chapter 4

Cardiac action potential propagation

The ordered propagation of the Cardiac Action Potential is the basis for coordinated contraction of the heart. Spread of the cardiac action potential can be thought of as coordinated on two different scales: globally throughout the entire heart (Fig. 4.1), and locally between adjacent cardiomyocytes. These different scales of coordinated propagation operate using different mechanisms and are discussed separately below.

4.1 Global cardiac action potential propagation

On the organ-level, cardiac action potential is initiated at *SA Node* in the RA. The SA Node is directly connected to contractile atrial cardiomyocytes and certain conducting fibers known as the “Interatrial Band”, which rapidly spread the action potential from the RA to the LA. Thus, following initiation by the SA Node, the cardiac action potential first spreads throughout both atria. The SA Node is called the primary pacemaker.

During this process the cardiac action potential travels through internodal pathways in RA to the *AV Node*, located just above the atrioventricular ring. The AV Nodal cells conduct cardiac action potentials relatively slowly and thus significantly delay the spread of the cardiac action potential from the atria to the ventricles. This AV delay is critical for ensuring that the atria have sufficient time to contract and fill the ventricles prior to ventricular contraction. AV Node is thus called the secondary pacemaker. If the SA

Node fails, the AV Node can assume control of the heart and drive it successfully.

From the AV Node, the impulse travels through the *bundle of His* located in the interventricular septum and down the left and right bundle branches. Both left and right branches terminate at the *Purkinje fibers*, a set of highly specialized conducting cardiomyocytes, which transmit the cardiac action potential to the endocardium at the apex of the heart, then finally to the ventricular epicardium. The propagation of action potentials must be carefully timed to coordinate the complex mechanics of contraction, synchronize ventricular contraction and thereby optimize the ejection of blood.

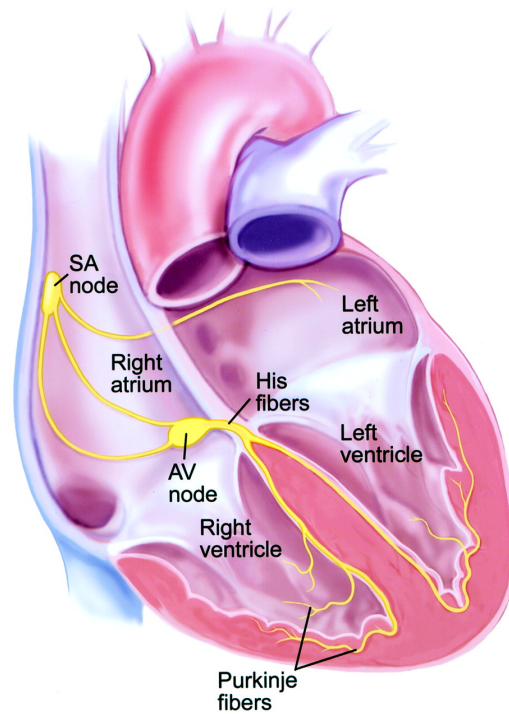


Figure 4.1: Action potential propagation throughout the heart.

4.2 Local cardiac action potential propagation

The molecular mechanism by which the cardiac action potential spreads from cell to cell is the free flow of ions between cardiomyocytes through gap junction-rich intercalated discs. This allows an action potential event in one cardiomyocyte to induce action

potential events in adjacent cells with a slight time delay. Macroscopically, this manifests as a wave of depolarization which spreads across sections of myocardium from its initiation point.

4.2.1 Contraction of cardiac myocytes

Cardiac cells communicate electrically to coordinate the muscular contraction of the heart to pump blood. Indeed, the excitation of cardiac myocytes triggers contraction—a process called excitation-contraction coupling. When an action potential depolarizes the cell membrane, voltage-gated Ca^{2+} channels are activated. Ca^{2+} entry through the L-type Ca^{2+} channel is essential for raising of $[\text{Ca}^{2+}]_i$ in the vicinity of the Ryanodine receptor 2 (RYR2) on the SR. The result of Ca^{2+} rise activates an adjacent cluster of RYRs, causing them to release Ca^{2+} locally from SR into the cytoplasm, which is called Ca^{2+} induced Ca^{2+} release (CICR). Such single event of CICR can raise $[\text{Ca}^{2+}]_i$ as high as $10 \mu\text{M}$ in microdomains of $1 \mu\text{m}$ in diameter. If many L-type Ca^{2+} channels open simultaneously, the spatial and temporal summation of many elementary calcium sparks leads to a global increase in $[\text{Ca}^{2+}]_i$. $[\text{Ca}^{2+}]_i$ ions then bind to cardiac troponin-C, which moves the tropomyosin away and expose the actin binding site. This removal of the tropomyosin frees the actin to be bounded by myosin and initiates contraction.

4.2.2 Gap junctions

Gap junctions (Fig. 4.2) are low-resistance pathways that mediate the electrical impulses between myocytes. They directly connect the cytoplasm of two cells, which allows various molecules, ions and electrical impulses to directly pass through a regulated gate between cells.

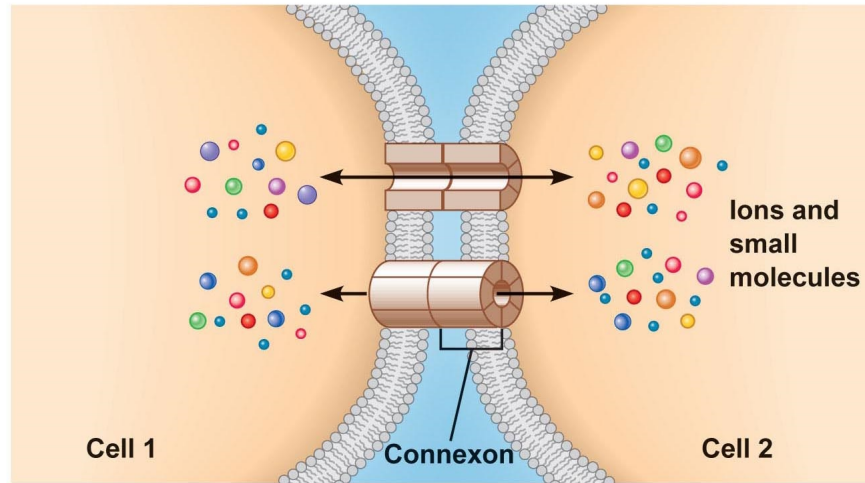


Figure 4.2: Gap junctions between adjacent cells.

Heterogeneity of connexin 43

Ventricular myocytes are connected electrically through gap junction channels formed mainly by Cx43 and, to a smaller extent, Cx45 [43]. Growing experimental and theoretical evidence suggests that *heterogeneity of Cx43* can lead to altered patterns of conduction, re-entrant arrhythmias and sudden death, [44, 9, 45, 46, 47]. For example, in [44], authors investigated susceptibility to arrhythmias in a genetically engineered murine model to express progressively decreasing levels of Cx43. Lethal tachyarrhythmias are initiated if cardiac Cx43 expression is decreased in a heterogeneous fashion to 18% of the control level. In [9], authors designed a murine model of heterogeneous gap junction channel expression, which results in conduction defects as well as markedly depressed contractile function. Additionally, in [47], authors showed that velocity and stability of conduction behave in a nonlinear manner when cardiomyocytes expressing different amounts of Cx43 are combined. In particular, conduction becomes very heterogeneous and is susceptible to block in the co-culturing of Cx43KO and wild type (WT) cells, while block is never observed in monogenotypic preparations.

4.2.3 Ephaptic coupling

The central assumption of cardiac electrophysiology has been that gap junctional coupling is the primary mechanism responsible for electrical communication between cardiac cells [48]. However, there are some controversy as to whether gap junctions are indeed necessary for electrical signal transmission [49]. This controversy has been given renewed attention in the light of experimental studies in [6, 7], which raised the question of whether conduction can be sustained in the absence of gap junctions. For instance, in [6], intercellular conductance measured by dual whole cell voltage clamp in pairs of adult rat ventricular myocytes with genetic Cx43 ablation is dramatically reduced from 588 nS to 10 nS. However, impulse propagation is reduced by only 50% in tissue composed of the same cells. In [7], optical mapping of the epicardial electrical activation pattern in Cx43KO mice reveals that ventricular conduction velocity is only slowed by up to 55% in the transverse direction and 42% in the longitudinal direction. In addition, the Cx43KO mice can still live up to 2 months.

One possible explanation of these intriguing observations is *ephaptic coupling*, first proposed in [8] and further elaborated in [49]. In [8], ephaptic coupling is seen as an electric field effect developed at the ID, which makes the propagation possible in the absence of gap junctions. IDs are microscopic identifying features of cardiac muscle, which are narrow clefts (2nm – 115 nm in width) connecting the individual cardiac cells to form a functional syncytium (Fig. 4.3).

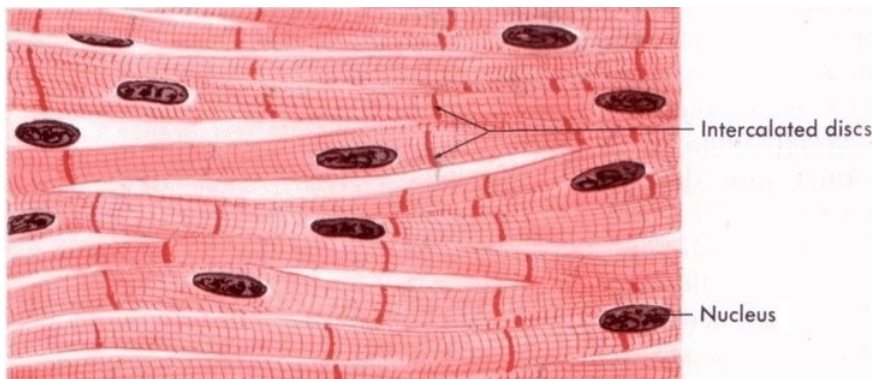


Figure 4.3: ID of branched cardiomyocytes.

Ephaptic mechanism

Fig. 4.4 is a cartoon showing action potential propagation in the presence of ephaptic coupling between two cells. As indicated in Fig. 4.4, cell A and cell B are electrically coupled through a narrow cleft space, and suppose that there are no gap junctions connecting the two cells. It is further assumed that Na^+ channels are preferentially localized to the cleft space, as shown by experiments in [10, 49, 50, 51]. When an action potential reaches cell A, the Na^+ current flows into the cell from extracellular space. Since Na^+ channels face the cleft, there must be a strong Na^+ influx from the cleft into cell A. By the continuity of the current, there is a current flowing into the cleft from the extracellular space away from the cleft. By Ohm's law, there should be a positive voltage difference driving this current, $\phi_{\text{ext}} - \phi_c > 0$. This difference should increase proportionally to the cleft resistance. Therefore, the narrow cleft implies greater value of potential differences $\phi_{\text{ext}} - \phi_c$. Consider the Na^+ channels embedded in the end membrane of cell B, which can detect the potential differences between intracellular space of cell B and cleft, $\phi_i^B - \phi_c$.

$$\phi_i^B - \phi_c = \phi_i^B - \phi_{\text{ext}} + \phi_{\text{ext}} - \phi_c.$$

Even if ϕ_{ext} and ϕ_i^B do not change by the depolarization of cell A. The positive difference $\phi_{\text{ext}} - \phi_c$ driven by the depolarization of end membrane of cell A gives rise to an increase in $\phi_i^B - \phi_c$. Once $\phi_i^B - \phi_c$ exceeds the threshold potential, the voltage gated Na^+ channels open. The end membrane of cell B is thus depolarized and undergoes excitation. The resulting inward current across the end membrane of cell B then depolarizes the side membrane of that cell, and the entire cell B becomes excited. We refer the above mechanism as ephaptic coupling.

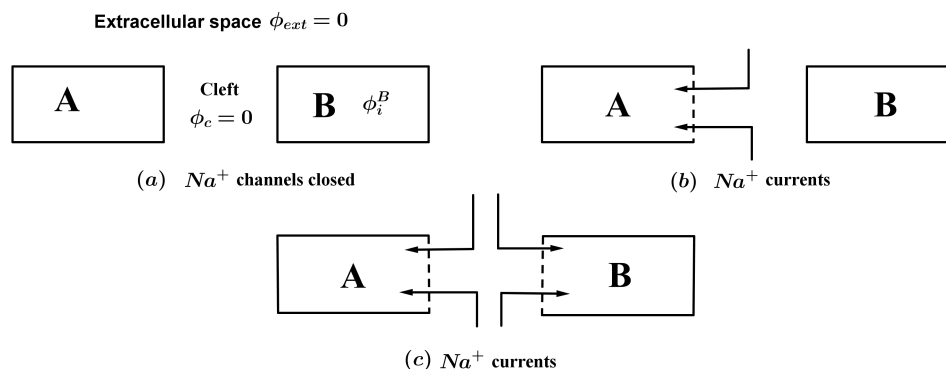


Figure 4.4: A cartoon of ephaptic coupling between two adjacent cells. Initially, the Na^+ channels of cell A and cell B are closed (a). When an action potential reaches cell A, its Na^+ channels open, allowing an influx of Na^+ current from extracellular space via the cleft (b). By Ohm's law, the cleft potential decreases, resulting in the depolarization of end membrane of cell B. It causes Na^+ channels to open and allows the current to flow inward (c), thus initiating the action potential in cell B.

Overview of studies about ephaptic coupling

Theoretical and numerical studies of ephaptic coupling have been revived after 2000s [10, 11, 12, 52, 53, 54, 55, 56]. In [10, 11], the authors assessed the hypothesis that ephaptic coupling can modulate the conduction when the Na^+ channels are preferentially localized in the cleft space, which causes a large negative potential in the cleft and influences conduction in two opposite ways, depending on the strength of gap junctional coupling. In particular, for normal and moderately reduced gap junctional coupling, localization of Na^+ channels to the cleft space forces Na^+ current to go through the large resistance between cleft and extracellular space, which slows down the conduction. In contrast, for greatly reduced gap junctional coupling, the negative cleft potential induced by Na^+ current in the prejunctional membrane leads to a suprathreshold depolarization of the postjunctional membrane, which facilitated and accelerated conduction. In [52], the authors applied a mathematical model that takes the detailed 3D cell geometry and ionic concentration effects to explore cardiac action potential propagation under severely reduced gap junctions. The study uncovers quantitative features of ephaptic

conduction that differ from previous studies based on one-dimensional models. For example, at higher values of d_{cleft} , the classical 1D models significantly overestimate the CV, whereas underestimate CV at lower values of d_{cleft} . The differences result from the discretization of the cleft along the radius in a 3D model. Thus, the effective resistance for the current to gain access to the cleft is smaller in 3D model. In this case, the current can easily enter the positions close to the lateral membrane, since the voltage gradient can develop. In addition, the authors also identified a mode of conduction in which the ephaptic and gap-junction-mediated mechanisms alternate. In [10, 55]. They showed that propagation is possible without gap junctions if the Na^+ channels are localized to the cleft and the resistance between the cleft space and extracellular space is sufficiently high. However, these parameter dependencies have not been well quantified. Other than that, authors of [54] derived and analyzed a mathematical model of two cells coupled through a shared cleft to explore the feasibility of ephaptic mechanism in the absence of gap junctions. Consistent with previous findings, they revealed that an increase in junctional Na^+ channel density is indeed necessary for propagation. Apart from this, they characterized parameter space of the junctional resistance to ensure successful propagation. In [12, 56], the authors explored ephaptic conduction by incorporating the detailed cell geometry, microdomain effects induced by the small extracellular space and Na^+ channel distribution. They found that the microdomain effect induced by inhomogeneities in extracellular space have dramatic effect on propagation speed. In particular, transverse conduction can be maintained by the ephaptic effects, even in the absence of gap junctions. Apart from numerical studies, authors in [57] experimentally demonstrated that changes in interstitial volume (V_{IS}) can modulate CV, anisotropy (AR), the CV-Gap junction relationship, thereby altering arrhythmia susceptibility. For example, albumin decreases histologically assessed V_{IS} , increases transverse CV by $71 \pm 10\%$, and lowers AR. Conversely, mannitol increases V_{IS} , decreases transverse CV by $24 \pm 4\%$, and increases AR. The CV-Gap junction relationship was assessed using the gap junction uncoupler carbenoxolone (CBX). Whereas $13 \mu\text{M}$ gap junction uncoupler carbenoxolone (CBX) does not significantly change CV in control condition, it slows transverse CV by $38 \pm 9\%$ during mannitol application. Furthermore, mannitol is associated with spontaneous ventricular tachycardias. Therefore, V_{IS} may underlie arrhythmia susceptibility, particularly in diseases associated with gap junction remodeling. Changes in the V_{IS} by

using albumin and mannitol can lead to the corresponding changes in the d_{cleft} . Therefore, the effect of V_{IS} on CV, AR and CV-Gap junction relationship may give rise to experimental evidence for the existence of ephaptic coupling.

4.3 Motivation of our study

Decreased and heterogeneous expression of Cx43 is a common feature in animal heart failure models [58, 59, 60]. Heart failure is the final common pathway of various cardiac pathologies and is associated with sudden cardiac death, mostly caused by ventricular arrhythmias [61, 62]. Based on the discussions of Sec. 4.2.3, emerging evidence suggests a more active role for ephaptic coupling in mediating intercellular electrical communication when gap junctions are reduced in a homogeneous manner [10, 11, 12, 52, 53, 55, 56]. However, the interplay between heterogeneous Cx43 expression and ephaptic coupling on cardiac conduction had not been investigated. In the following chapter, we will explore the effects of ephaptic coupling on cardiac impulse propagation via numerical simulations when Cx43 expression is reduced and heterogeneous.

Chapter 5

The dual effect of ephaptic coupling on cardiac conduction with heterogeneous expression of connexin 43

In this chapter, we explore the effects of ephaptic coupling on cardiac conduction when Cx43 expression is reduced in a heterogeneous fashion. The main results of this chapter have been published in [63] joint with Prof. Yoichiro Mori and Prof. Elena G. Tolkacheva.

5.1 Materials and Methods

5.1.1 Mathematical model

Bidomain model with ephaptic coupling

A two dimensional (2D) bidomain model (Fig. 5.1A) of electrical conduction is modified to incorporate ephaptic coupling [11, 54], which relies on the presence of a junctional cleft space between the ends of adjacent cells. Each cell is assumed to be cylindrical in shape with radius r and length L . The cells are connected by gap junctions to form

an $M \times N$ rectangular lattice. At each lattice point (i, j) , we associate intracellular potential $\phi_i^{(i,j)}$ and extracellular potential $\phi_e^{(i,j)}$. The cleft lies in between cells (i, j) and $(i, j + 1)$. We then define a cleft potential $\phi_c^{(i,j+\frac{1}{2})}$ at location $(i, j + \frac{1}{2})$. We call the space, which lies in the extracellular space and stays adjacent to the cleft, the extracellular-cleft space. The potential in the extracellular-cleft space is denoted by $\phi_{ec}^{(i,j+\frac{1}{2})}$. Note that Fig. 5.1A shows the lattice view of the model, whereas Fig. 5.1B shows the connection between lattices. In particular, Fig. 5.1B shows a circuit diagram for two adjacent cells that are ephaptically coupled through a common cleft space in the presence of end-to-end gap junctions (GJ_{end}), side-to-side gap junctions (GJ_{side}) and resistive connections between extracellular spaces (R_{ee}) are not shown here. Cleft space is modelled as a single narrow compartment with resistive connections (R_c) to the extracellular space; Resistive connections between extracellular space and the extracellular-cleft space are denoted by R_{ec} . Intracellular and extracellular spaces of each cell are separated by the cell side membrane; intracellular and cleft spaces are separated by the cell end membrane. Both side and end membranes allow the free flow of ionic and capacitive currents. Ephaptic coupling is maintained by the active end membranes that are connected by a shared cleft potential. In order to save on computational cost, we treat intracellular and extracellular spaces of each cell to be isopotential.

As can be seen from Fig. 5.1, four different compartments, namely intracellular, extracellular, cleft, and extracellular-cleft spaces, are modelled separately. Current conservation in each compartment provides the following equations, with parameters listed in Table 5.1.

- Intracellular space ($\phi_i^{(i,j)}$; $1 \leq i \leq M$, $2 \leq j \leq N - 1$) :

$$\begin{aligned}
& GJ_{\text{end}}(\phi_i^{(i,j)} - \phi_i^{(i,j-1)}) + GJ_{\text{end}}(\phi_i^{(i,j)} - \phi_i^{(i,j+1)}) \\
& + GJ_{\text{side}}(\phi_i^{(i,j)} - \phi_i^{(i-1,j)}) + GJ_{\text{side}}(\phi_i^{(i,j)} - \phi_i^{(i+1,j)}) \\
& + A_{\text{end}}C_m \frac{\partial(\phi_i^{(i,j)} - \phi_c^{(i,j-\frac{1}{2})})}{\partial t} + A_{\text{end}}C_m \frac{\partial(\phi_i^{(i,j)} - \phi_c^{(i,j+\frac{1}{2})})}{\partial t} + I_{\text{end}} \\
& + A_{\text{side}}C_m \frac{\partial(\phi_i^{(i,j)} - \phi_e^{(i,j)})}{\partial t} + I_{\text{side}} = 0,
\end{aligned} \tag{5.1}$$

where $A_{\text{end}} = \pi r^2$ and $A_{\text{side}} = 2\pi rL$ denote the cross-sectional and side areas of a

cell, respectively; $GJ_{\text{end}} = A_{\text{end}}g_{\text{end}}$ and $GJ_{\text{side}} = \frac{A_{\text{side}}}{2}g_{\text{side}}$ denote end-to-end and side-to-side gap junctional conductance, respectively; $\phi_i^{(i,j)}$, $\phi_i^{(i,j-1)}$ and $\phi_i^{(i,j+1)}$ denote the intracellular potentials of cells (i, j) , $(i, j-1)$ and $(i, j+1)$, respectively; $\phi_i^{(i-1,j)}$ and $\phi_i^{(i+1,j)}$ denote the intracellular potentials of cells $(i-1, j)$ and $(i+1, j)$, respectively; $\phi_c^{(i,j-\frac{1}{2})}$ and $\phi_c^{(i,j+\frac{1}{2})}$ denote cleft potentials at locations $(i, j-\frac{1}{2})$ and $(i, j+\frac{1}{2})$, respectively; C_m represents the membrane capacitance per area; I_{end} and I_{side} denote the outward ionic current of the end and side membranes, respectively; $\phi_e^{(i,j)}$ represents the extracellular potential of cell (i, j) .

Note that for $j = 1$, terms $GJ_{\text{end}}(\phi_i^{(i,j)} - \phi_i^{(i,j-1)})$ and $A_{\text{end}}C_m \frac{\partial(\phi_i^{(i,j)} - \phi_c^{(i,j-\frac{1}{2})})}{\partial t}$ are dropped from Eq. (5.1). Similarly, for $j = N$, terms $GJ_{\text{end}}(\phi_i^{(i,j)} - \phi_i^{(i,j+1)})$ and $A_{\text{end}}C_m \frac{\partial(\phi_i^{(i,j)} - \phi_c^{(i,j+\frac{1}{2})})}{\partial t}$ are dropped from Eq. (5.1). In order to minimize the edge effects, we impose periodic boundary condition in the x direction (see Fig. 5.1A): we identify $\phi_i^{(i-1,j)}$ with $\phi_i^{(M,j)}$ for $i = 1$, and we identify $\phi_i^{(i+1,j)}$ with $\phi_i^{(1,j)}$ for $i = M$.

- Extracellular space ($\phi_e^{(i,j)}$; $1 \leq i \leq M$, $2 \leq j \leq N-1$) :

$$\begin{aligned} & \frac{\phi_e^{(i,j)} - \phi_{ec}^{(i,j-\frac{1}{2})}}{R_{ec}} + \frac{\phi_e^{(i,j)} - \phi_{ec}^{(i,j+\frac{1}{2})}}{R_{ec}} \\ & + \frac{\phi_e^{(i,j)} - \phi_e^{(i-1,j)}}{R_{ee}} + \frac{\phi_e^{(i,j)} - \phi_e^{(i+1,j)}}{R_{ee}} \\ & - A_{\text{side}}C_m \frac{\partial(\phi_i^{(i,j)} - \phi_e^{(i,j)})}{\partial t} - I_{\text{side}} = 0, \end{aligned} \quad (5.2)$$

where $\phi_{ec}^{(i,j-\frac{1}{2})}$ and $\phi_{ec}^{(i,j+\frac{1}{2})}$ denote the extracellular-cleft potentials at location $(i, j-\frac{1}{2})$ and $(i, j+\frac{1}{2})$, respectively; R_{ec} represents the resistance between extracellular space and the extracellular-cleft space; $\phi_e^{(i-1,j)}$ and $\phi_e^{(i+1,j)}$ denote the extracellular potentials of cells $(i-1, j)$ and $(i+1, j)$, respectively; R_{ee} represents the resistance between extracellular spaces in the x direction (see Fig. 5.1A).

Note that for $j = 1$, term $\frac{\phi_e^{(i,j)} - \phi_{ec}^{(i,j-\frac{1}{2})}}{R_{ec}}$ is dropped from Eq. (5.2). Similarly, for $j = N$, $\frac{\phi_e^{(i,j)} - \phi_{ec}^{(i,j+\frac{1}{2})}}{R_{ec}}$ is dropped from Eq. (5.2). In order to minimize the edge effects, we impose periodic boundary condition in the x direction (see Fig. 5.1A): we identify $\phi_e^{(i-1,j)}$ with $\phi_e^{(M,j)}$ for $i = 1$, and we identify $\phi_e^{(i+1,j)}$ with $\phi_e^{(1,j)}$ for $i = M$.

- Cleft space ($\phi_c^{(i,j+\frac{1}{2})}$; $1 \leq i \leq M$, $1 \leq j \leq N-1$):

$$\begin{aligned}
& - A_{\text{end}} C_m \frac{\partial(\phi_i^{(i,j)} - \phi_c^{(i,j+\frac{1}{2})})}{\partial t} - A_{\text{end}} C_m \frac{\partial(\phi_i^{(i,j+1)} - \phi_c^{(i,j+\frac{1}{2})})}{\partial t} - I_{\text{end}} \\
& + \frac{\phi_c^{(i,j+\frac{1}{2})} - \phi_{ec}^{(i,j+\frac{1}{2})}}{R_c} = 0,
\end{aligned} \tag{5.3}$$

where R_c represents the resistance between cleft and extracellular space.

- Extracellular-cleft space ($\phi_{ec}^{(i,j+\frac{1}{2})}$; $1 \leq i \leq M$, $1 \leq j \leq N-1$):

$$\frac{\phi_e^{(i,j)} - \phi_{ec}^{(i,j+\frac{1}{2})}}{R_{ec}} - \frac{\phi_e^{(i,j+1)} - \phi_{ec}^{(i,j+\frac{1}{2})}}{R_{ec}} - \frac{\phi_c^{(i,j+\frac{1}{2})} - \phi_{ec}^{(i,j+\frac{1}{2})}}{R_c} = 0. \tag{5.4}$$

Modeling Cx43 expression

Since we aim to study the effect of distribution pattern of Cx43KO and WT cells on conduction features in the presence of ephaptic coupling, we follow [47] to model heterogeneous Cx43 expression, where genotypes of cells are allocated stochastically according to the predefined Cx43KO content (p). In other words, under each p , we stochastically assign cell genotypes to be Cx43KO or WT. Here, $p = 0$ implies that the Cx43KO content is 0%, i.e. all cells are WT. In contrast, $p = 1$ implies that Cx43KO content is 100%, i.e. all cells are knockout.

Conductance of gap junctions is set proportionally to the area of contacts between adjacent cells using proportionality constants g_{end} and g_{side} (Table 5.1) for end-to-end and side-to-side contacts, respectively. For connections between WT cells, g_{end} and g_{side} are scaled by a factor k_{WT} (Table 5.1). For connections between Cx43KO cells, g_{end} and g_{side} are scaled by a factor k_{Cx43KO} (Table 5.1). The value of k_{Cx43KO} (Table 5.1) is chosen to keep the longitudinal conduction velocity (CV_L) in the absence of ephaptic coupling (which can be modelled by a sufficiently large cleft width) the same as CV_L for Cx43KO strands reported in [47], where ephaptic coupling is not considered.

As reported in previous studies, the residual low connexin expressions between Cx43KO and WT cells are mediated by Cx43/Cx45 [64, 65]. For connections between WT and Cx43KO cells, g_{end} and g_{side} are also scaled by the factor k_{Cx43KO} based on the assumption that the coupling between cells is essentially determined by the cell expressing the least amount of connexins [64]. In [64], the authors experimentally measures the intercellular conductance between pairs of ventricular myocytes with different

Cx43 expression. They find that ablation of Cx43 in one cell of a pair caused a marked decrease in mean intercellular conductance, from 68.3 ± 9.6 nS to 5.2 ± 1.7 nS.

Membrane currents

The excitable dynamics of normal cardiac tissue is described by Luo-Rudy dynamic guinea pig ventricular model 2007 (LRd 2007) [13]. Two different distributions are used for Na^+ channels: (1) uniform distribution, in which Na^+ channels are evenly distributed along the cell membrane; (2) localized distribution, in which all Na^+ channels are localized to the cleft spaces at the two cell ends, while the total conductance of Na^+ channels is fixed to its normal value. In this study, Na^+ channels are assumed to be localized to the cleft, unless indicated otherwise. The other ionic channels of LRd 2007 model are uniformly distributed along the cell membrane.

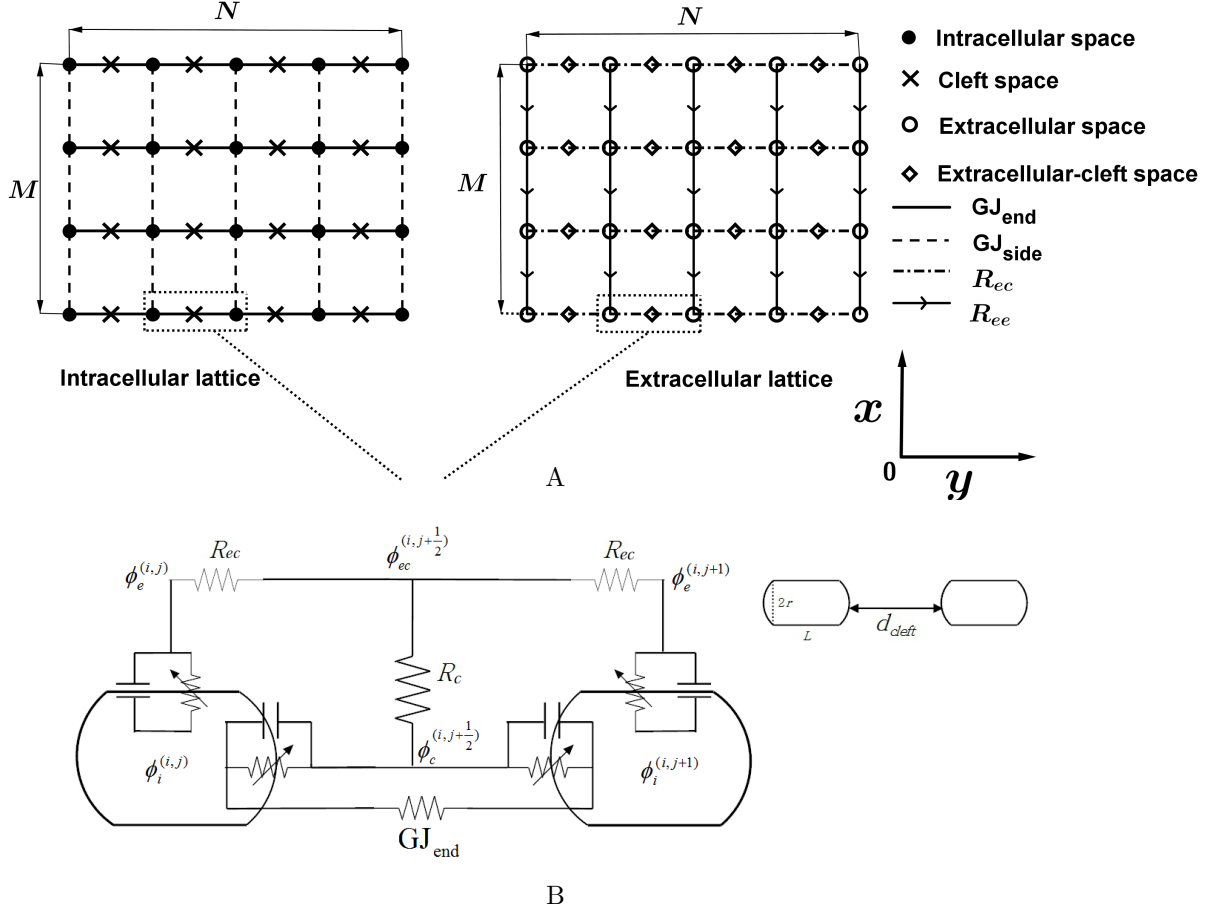


Figure 5.1: A lattice view of a 2D bidomain model in the presence of ephaptic coupling (A) and circuit diagram for two adjacent cells coupled through a shared cleft in the presence of end-to-end gap junctions (GJ_{end}) (B), side-to-side gap junctions (GJ_{side}) and resistive connections between extracellular spaces (R_{ec}) are not shown here. This diagram is not to scale, as the cleft width is three orders of magnitude smaller than the length of cell. $\phi_i^{(i,j)}$ and $\phi_i^{(i,j+1)}$ represent intracellular potentials of cells at location (i, j) and $(i, j + 1)$, respectively. $\phi_e^{(i,j)}$ and $\phi_e^{(i,j+1)}$ represent extracellular potentials of cells (i, j) and $(i, j + 1)$, respectively. Cleft space is modelled as a narrow compartment between cells (i, j) and $(i, j + 1)$, which is resistively connected (R_c) to the extracellular space. Cleft potential $\phi_c^{(i,j+\frac{1}{2})}$ is defined at location $(i, j + \frac{1}{2})$. The space, which lies in the extracellular space and stays adjacent to the aforementioned cleft is called the extracellular-cleft space. The potential in the extracellular-cleft space is denoted by $\phi_{ec}^{(i,j+\frac{1}{2})}$. Resistive connections between extracellular space and the extracellular-cleft space are denoted by R_{ec} .

Table 5.1: Parameters that enter our model.

| Symbol | Parameter | Value/Expression | Reference |
|-----------------------|--|---|-----------|
| r | Radius of cell | 1.1×10^{-3} cm | [11] |
| L | Length of cell | 10^{-2} cm | [11] |
| g_{end} | End-to-end gap junctional conductance per area | 6.66×10^2 mS/cm ² | [11] |
| α | Ratio between g_{end} and g_{side} | 6 | [66] |
| g_{side} | Side-to-side gap junctional conductance per area | $\frac{g_{\text{end}}}{\alpha}$ | Derived |
| C_m | Membrane capacitance per area | 1 μ F/cm ² | [11] |
| d_{cleft} | Cleft width | 2 – 115 nm | [11] |
| σ_{ext} | Extracellular conductivity | 6.67 mS/cm | [11] |
| R_c | Resistance between cleft and extracellular space | $\frac{1}{8\pi\sigma_{\text{ext}}d_{\text{cleft}}}$ | [11] |
| AR_x | Anisotropy ratio of resistance in x direction | 1.33 | [67] |
| AR_y | Anisotropy ratio of resistance in y direction | 0.35 | [67] |
| R_{ec} | Resistance between extracellular space and extracellular cleft | $\frac{1}{2\text{AR}_y A_{\text{end}} g_{\text{end}}}$ | [67] |
| R_{ee} | Resistance between extracellular spaces in x direction | $\frac{2}{\text{AR}_x A_{\text{side}} g_{\text{side}}}$ | [67] |
| k_{WT} | Scaling factor for g_{end} and g_{side} between WT cells | 1 | [47] |
| k_{Cx43KO} | Scaling factor for g_{end} and g_{side} between Cx43KO cells / WT and Cx43KO cells | 0.005 | Derived |
| ϕ_i | Intracellular potential | | |
| ϕ_e | Extracellular potential | | |
| ϕ_c | Cleft potential | | |
| ϕ | Side transmembrane potential | $\phi_i - \phi_e$ | |

5.1.2 Numerical simulation

Simulations are run in a lattice consisting of $M \times N$ cells (Fig. 5.1A), where $M = 2, 3, 6, 10,$ and $16,$ and $N = 75.$ Initially, all potentials and gating variables are held at resting states. Conduction is initiated by applying 0.5 ms excitatory current pulses of amplitude $0.15 \mu\text{A}$ into all cells at the left hand side of the lattice.

The resulting model consists of a large number of differential algebraic equations.

We use a splitting method by updating the potential and gating variables of ion channels separately to solve the system. When updating the potential, gating variables are fixed; the linear parts of the system (linear in potential) are treated using backward Euler method; the ionic currents and dynamics are linearized and treated using backward Euler method afterwards. The system is solved via a direct method (backslash operator in Matlab).

We define the wavefront of a normal travelling action potential as the spatial location where the side transmembrane potential (ϕ) crosses -30 mV with $\frac{\partial\phi}{\partial t} > 0$. This value is set to distinguish small amplitude action potential (SAP) (Sec. 5.2.2) from normal action potential, since SAP does not reach -30 mV. Activation is monitored by identifying the earliest activation time (EAT) at every column of the $M \times N$ lattice (Fig. 5.1A). CV_L is computed by linear regression of EAT over 20% to 80% of lattice length to exclude the boundary effect. Conduction block (CB) is defined as the failure of wavefront to reach the right hand side of the lattice.

5.2 Results

5.2.1 The effect of ephaptic coupling on cardiac conduction.

To explore the effects of ephaptic coupling on impulse propagation, we identify several possible values of cleft width (d_{cleft}), from 2 nm to 115 nm (see Table 5.1). Note that smaller d_{cleft} corresponds to larger R_c , which therefore implies stronger ephaptic coupling.

In Figs. 5.2A and 5.2B, CV_L is plotted as a function of d_{cleft} for $p = 1$ (A, Cx43KO cells) and $p = 0$ (B, WT cells), respectively. As observed, Fig. 5.2A displays a biphasic behavior of CV_L : with increasing d_{cleft} , CV_L exhibits a marked increase to 13.1 cm/s (at $d_{\text{cleft}} = 8$ nm) followed by a decrease to 2.5 cm/s with further cleft widening. In contrast, when gap junctional coupling is strong, CV_L shows a monotone increase as d_{cleft} increases (see Fig. 5.2B). Note that in Fig. 5.2, the most notable differences in qualitative behaviors of CV_L are seen for $d_{\text{cleft}} < 20$ nm.

To further investigate the effects of ephaptic coupling on conduction, we choose $d_{\text{cleft}} = 2$ nm, 3.5 nm, 8 nm, 8.5 nm, and 115 nm as the representative values in our numerical simulations.

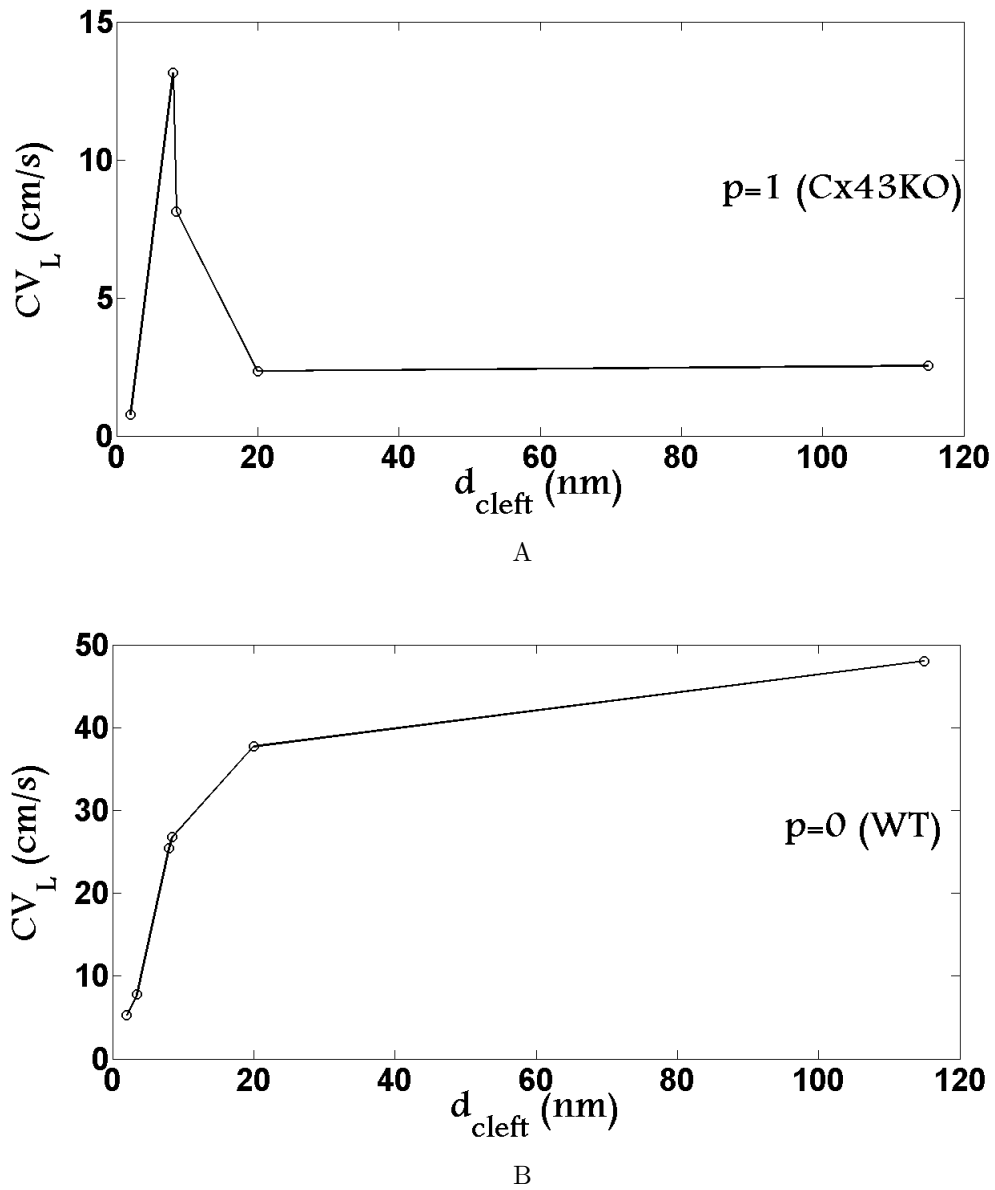


Figure 5.2: CV_L as a function of d_{cleft} for $p = 1$ (A, Cx43KO) and $p = 0$ (B, WT).

5.2.2 Conduction features when Cx43KO content is 100% ($p = 1$).

To further explore spatiotemporal excitation patterns that occur in the near absence of gap junctions, we perform numerical simulations in lattices consisting of 100% Cx43KO cells. The following three novel conduction features are observed in the presence of

ephaptic coupling: alternating conduction (Sec. 5.2.2), instability of planar fronts (Sec. 5.2.2) and SAP (Sec. 5.2.2). However, when gap junction-mediated mechanism dominates (d_{cleft} is sufficiently large), none of these features can be observed. Note that alternating conduction and SAP are one-dimensional phenomena, which do not depend on lattice width. In contrast, the instability of planar fronts can only be observed in a 2D simulation.

Alternating conduction

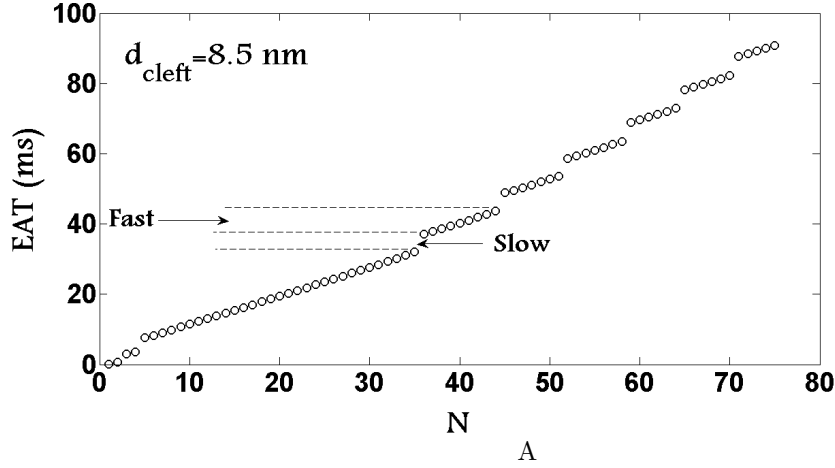
Fig. 5.3 shows EAT as a function of N for $d_{\text{cleft}} = 8.5$ nm (A), 8.6 nm (B), 8.7 nm (C), 8.9 nm (D), which demonstrates the presence of periodic transitions between fast and slow conduction under severely reduced gap junctions. For instance, at $d_{\text{cleft}} = 8.9$ nm, action potential propagates fast between columns N and $N + 1$ when N is even, but slowly between columns N and $N + 1$ when N is odd. Note that for $9 \text{ nm} \leq d_{\text{cleft}} \leq 9.6 \text{ nm}$, the EAT pattern is the same as that for $d_{\text{cleft}} = 8.9$ nm.

Fig. 5.4 shows the end transmembrane potential ($\phi_{ic} = \phi_i - \phi_c$) traces of the left (ϕ_{icL}) and right sides (ϕ_{icR}) of cells at location (3, 24), (3, 25), (3, 26) and (3, 27), where $d_{\text{cleft}} = 5$ nm (A), 8.9 nm (B) and 10 nm (C). As indicated in Fig. 5.4B, ϕ_{ic} traces of the fast conduction phase (cell (3, 24) to cell (3, 25), and cell (3, 26) to cell (3, 27) in Fig. 5.3D) are similar to the potential traces ($\phi_{icR}^{(3,24)}$, $\phi_{icL}^{(3,25)}$, $\phi_{icR}^{(3,26)}$ and $\phi_{icL}^{(3,27)}$) seen when $d_{\text{cleft}} = 5$ nm, at which the propagation is driven primarily by ephaptic coupling. However, ϕ_{ic} profiles of the slow conduction phase (cell (3, 25) to cell (3, 26) in Fig. 5.3D) are similar to the potential traces ($\phi_{icR}^{(3,25)}$ and $\phi_{icL}^{(3,26)}$) seen when $d_{\text{cleft}} = 10$ nm, at which the conduction can be attributed to the residual gap junctional coupling. Alternating conduction shown in Fig. 5.3 thus lies in an intermediate regime, in which the two aforementioned mechanisms play an equal role, but spatially alternate in being the dominant mode of conduction. Alternating conduction was reported in [52], where the authors only demonstrated the pattern similar to the one shown in Fig. 5.3D. However, patterns seen in Figs. 5.3A - 5.3C have never been reported previously.

Note that two upstrokes are observed in $\phi_{icR}^{(3,25)}$ and $\phi_{icL}^{(3,26)}$ traces of Fig. 5.4B and in multiple traces of Fig. 5.4C. For $\phi_{icR}^{(3,25)}$ trace in Fig. 5.4B, the first upstroke corresponds to the depolarization of the right end membrane of cell (3, 25), which results in a drop in the cleft potential shared by cells (3, 25) and (3, 26). The drop

in the aforementioned cleft potential gives rise to a passive increase in $\phi_{icL}^{(3,26)}$ (first upstroke in $\phi_{icL}(26)$ trace), which is not large enough to activate the left end membrane of cell (3, 26). Similarly, the depolarization of left end membrane of cell (3, 26) (second upstroke in $\phi_{icL}^{(3,26)}$ trace) can lead to a passive increase in $\phi_{icR}^{(3,25)}$ (second upstroke in $\phi_{icR}^{(3,25)}$ trace). Similar explanation can be applied to traces in Fig. 5.4C. However, in Fig. 5.4A ($d_{\text{cleft}} = 5$ nm), cells are more tightly connected, which gives rise to stronger ephaptic coupling, and therefore, only one upstroke is seen on ϕ_{ic} traces.

We point out that the differences in upstroke timing in the ϕ_{ic} traces of Fig. 5.4 are primarily a result of ephaptic coupling (for example $\phi_{icR}^{(3,24)}$ and $\phi_{icL}^{(3,25)}$ traces) and different action potential arrival times in the cleft spaces (for example $\phi_{icL}^{(3,25)}$ and $\phi_{icR}^{(3,25)}$ traces). The upstroke timing differences here should thus not be confused with the junctional and intracellular delays discussed in [68, 69], where ephaptic coupling are not considered.



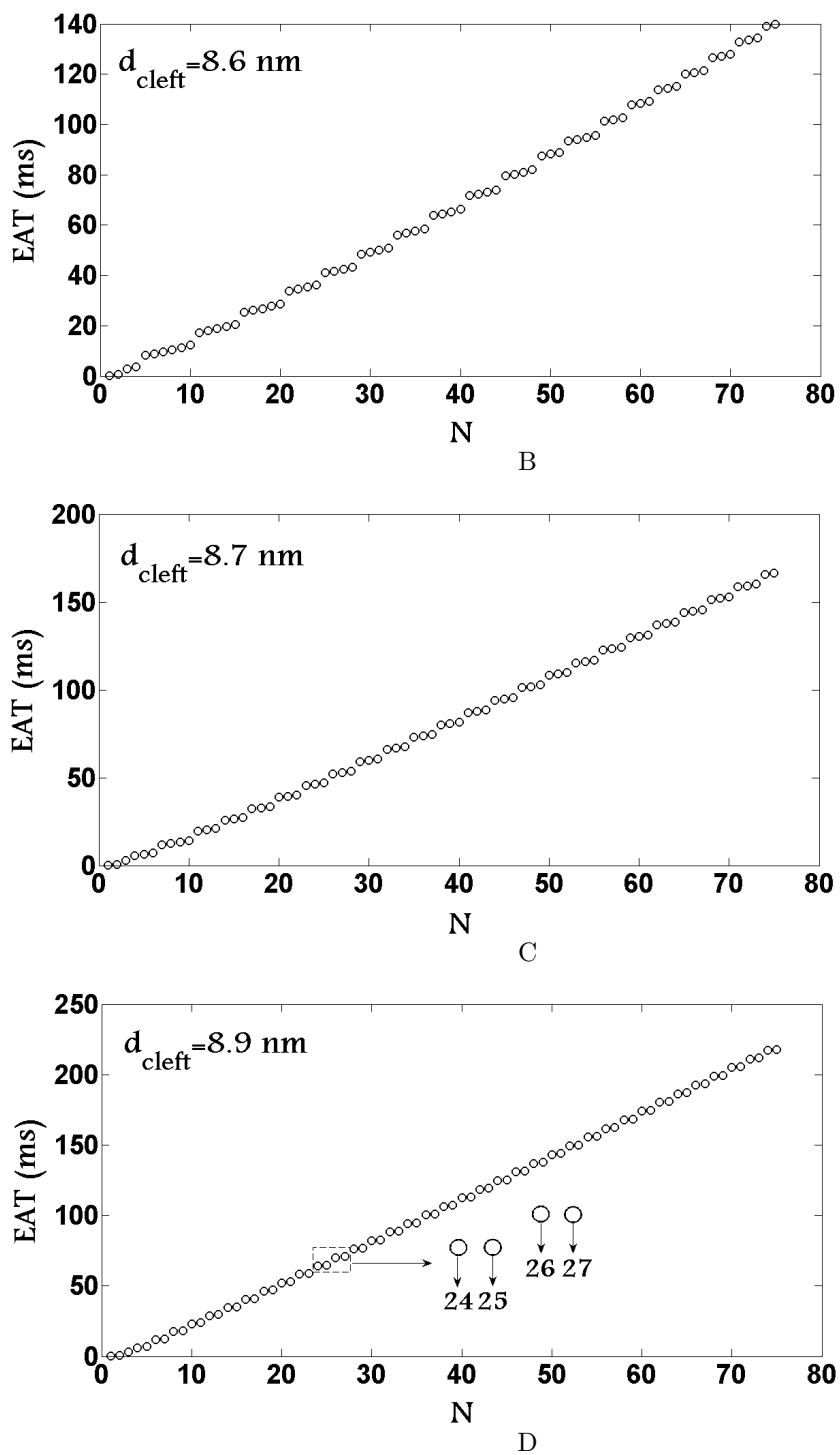


Figure 5.3: EAT as a function of N at $d_{\text{cleft}} = 8.5 \text{ nm}$ (A), 8.6 nm (B), 8.7 nm (C), 8.9 nm (D).

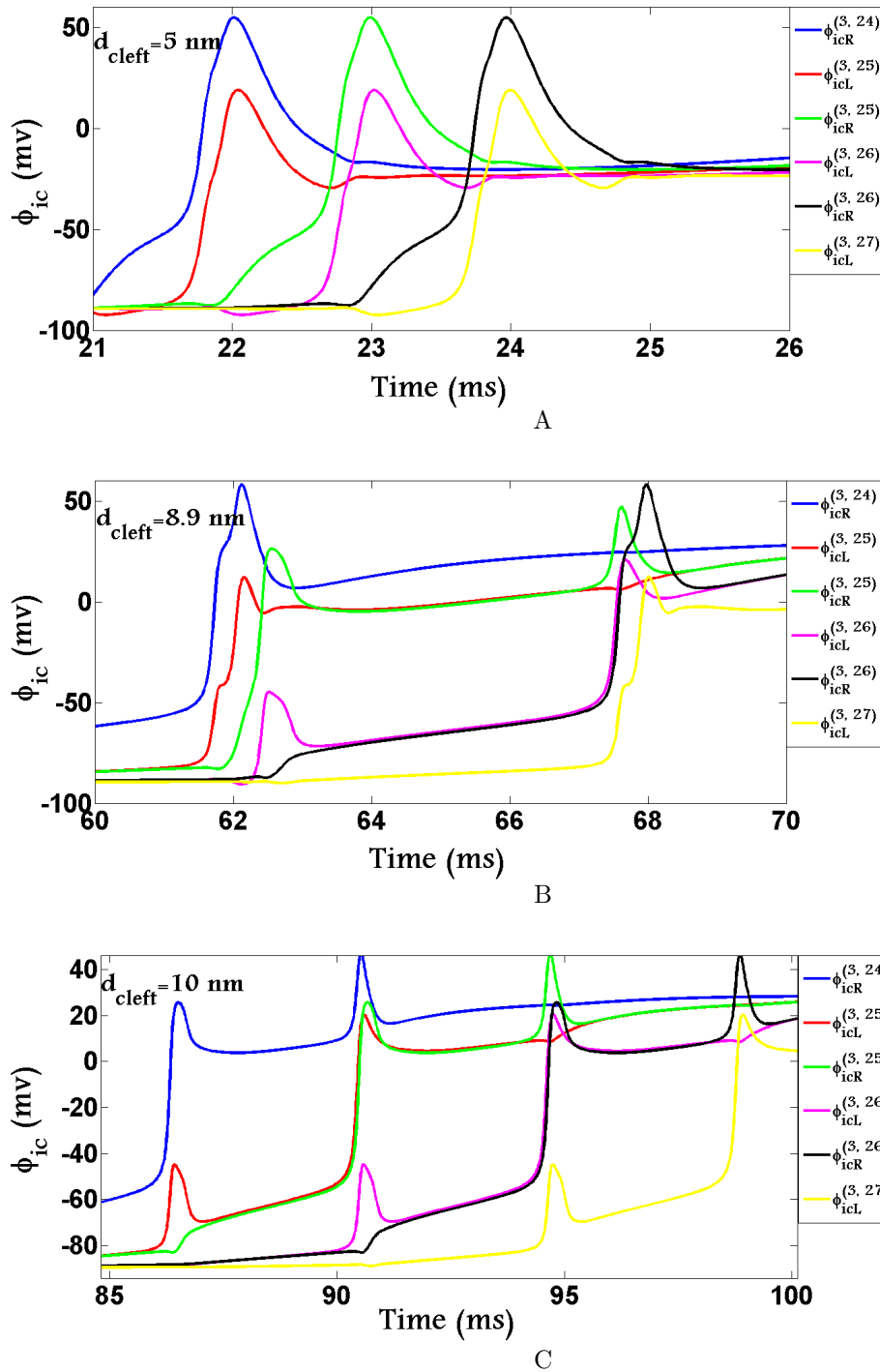


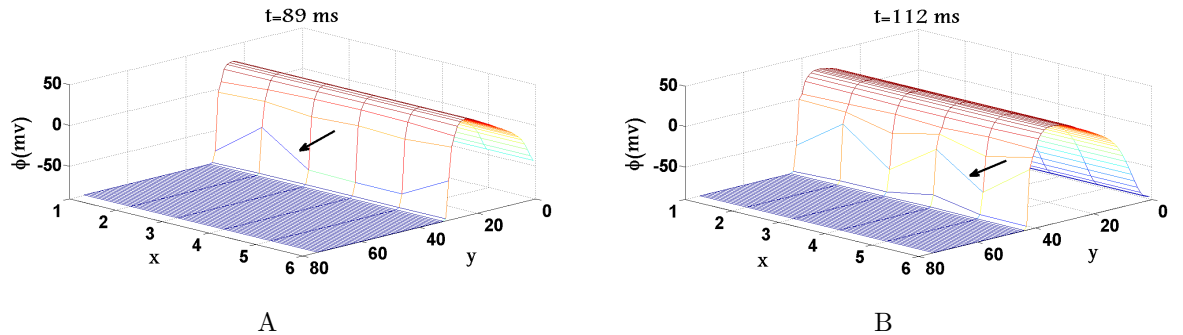
Figure 5.4: End transmembrane potential ($\phi_{ic} = \phi_i - \phi_c$) traces of the left (ϕ_{icL}) and right (ϕ_{icR}) sides of cells at location (3, 24), (3, 25), (3, 26) and (3, 27), where $d_{\text{cleft}} = 5 \text{ nm}$ (A), 8.9 nm (B) and 10 nm (C).

Instability of planar fronts

Fig. 5.5 shows a propagation of an unusual action potential at $d_{\text{cleft}} = 9.8$ nm, in which instability of planar fronts occurs. This effect is only observed for $9.7 \text{ nm} \leq d_{\text{cleft}} \leq 9.8 \text{ nm}$. Figs. 5.5A - 5.5D show a sequence of snapshots demonstrating propagation when an external current activates all cells at the left hand side of the lattice. The snapshots plot ϕ at time (t) = 89 ms (A), 112 ms (B), 139 ms (C) and 173 ms (D). In order to make the wavefront easier to observe, we rotate the figures by 180° . As indicated in Fig. 5.5, there is an irregular change in the shape of the wavefront (denoted by black arrows), which proceeds in a zigzag fashion. Such wavefronts propagate to neighboring cells in a spatially heterogeneous manner, rather than evenly along the lattice.

This zigzag wavefront pattern is a result of instability of the planar fronts, reminiscent of stability of front solutions studies in [70]. Inevitable numerical deviations from the planar front, which will decay and remain small in case of a stable planar front, and grows when the planar front is unstable. Such numerical deviations, in biophysical terms, correspond to external noise; the planar front thus destabilizes in the presence of noise.

We speculate that the instability also results from the presence of two modes of conduction, the ephaptic and the gap junction mediated. Unlike alternating conduction (Sec. 5.2.2) in which the mode of conduction depends only on the y -coordinate (Fig. 5.1A), here, the mode of conduction depends on the x -direction as well. A checkerboard pattern of ephaptic and gap junction mediated alternation gives rise to the instability of planar fronts.



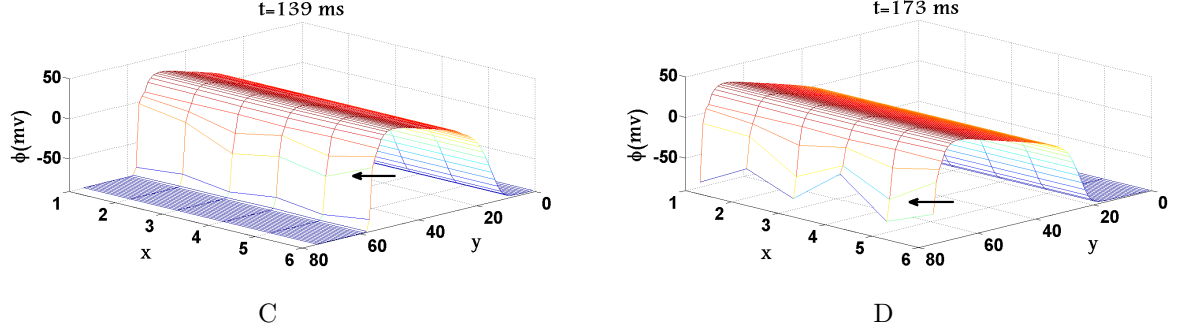


Figure 5.5: Instability of planar fronts. A sequence of snapshots of propagation, illustrating ϕ at $t = 89$ ms (A), 112 ms (B), 139 ms (C) and 173 ms (D), respectively at $d_{\text{cleft}} = 9.8$ nm.

Small amplitude action potentials (SAP)

Fig. 5.6 demonstrates a novel type of action potential propagation at $d_{\text{cleft}} = 3.5$ nm, which has a much lower potential amplitude than the normal conduction, with the maximum value of $\phi = -40$ mV. Figs. 5.6A - 5.6D show a sequence of snapshots demonstrating SAP when an external current activates all cells at the left hand side of the lattice. The snapshots illustrate ϕ at time (t) = 13 ms (A), 51 ms (B), 80 ms (C) and 126 ms (D), respectively.

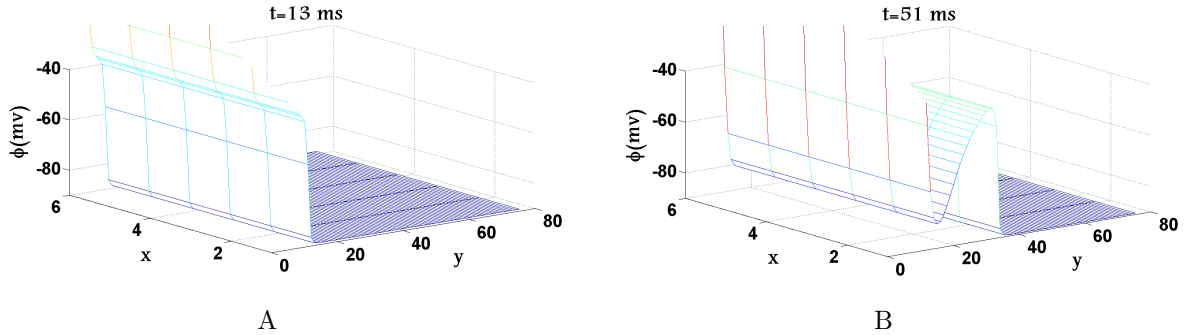
Note that propagation patterns depend highly on the values of d_{cleft} . For instance, SAP occurs for $3.5 \text{ nm} \leq d_{\text{cleft}} \leq 3.7 \text{ nm}$, while CB occurs for $3.2 \text{ nm} \leq d_{\text{cleft}} \leq 3.4 \text{ nm}$. For $3.8 \text{ nm} \leq d_{\text{cleft}} \leq 5 \text{ nm}$, one observes a wave that has characteristics in between normal conduction and SAP (see Fig. 5.7), reminiscent of stacked fronts observed in [71]. Finally, for $2 \text{ nm} \leq d_{\text{cleft}} \leq 3.1 \text{ nm}$ and $d_{\text{cleft}} > 5 \text{ nm}$, normal conduction is seen. However, when $2 \text{ nm} \leq d_{\text{cleft}} \leq 3.1 \text{ nm}$, conduction is extremely slow with $CV_L = 0.7 \text{ cm/s}$.

At $d_{\text{cleft}} = 3.5$ nm, R_c is very high. In this case, the cleft potential drops low enough to excite the end membrane. However, the resulting inward Na^+ current is not sufficient to fully activate the side membrane, and therefore SAP occurs. In other words, when SAP occurs, Na^+ channels residing on the end membrane are fully activated, as indicated by the activation gating variable (m_{end}) of Na^+ channels that reside on the end membrane of cell (3, 25) (Fig. 5.8A). Nevertheless, the side membrane is not fully

excited, as indicated by ϕ profile of that cell (Fig. 5.8B). SAP may thus be seen as a cardiac propagation jumping from cleft to cleft.

When SAP occurs, L-type Ca^{2+} channels are not fully activated. Figs. 5.9A and 5.9B show the activation gating variable (d) of Ca^{2+} channels that reside on the end (d_{end} , A) and side (d_{side} , B) membranes of cell (3, 25); Fig. 5.9C exhibits ϕ profile of cell (3, 25), where $d_{\text{cleft}} = 3.5$ nm (blue), 3.8 nm (red), and 115 nm (green). As observed in Figs. 5.9A and 5.9B, gating variable d is not active when SAP occurs ($d_{\text{cleft}} = 3.5$ nm). This is in contrast to normal conduction ($d_{\text{cleft}} = 115$ nm), in which Ca^{2+} channels are fully activated. SAP is thus a wave in which an electrical pulse propagates without a large rise in Ca^{2+} concentration. We may therefore regard SAP as an electromechanically dissociated wave.

As shown in Fig. 5.9, for $d_{\text{cleft}} = 3.8$ nm, the behaviors of d_{end} , d_{side} and ϕ lie in an intermediate regime. Unlike SAP, the resulting influx of Na^+ current is sufficient to activate Ca^{2+} channels residing on the side membrane, indicated by d_{side} in Fig. 5.9B. In other words, the steep depolarization of side membrane results from Na^+ current, whereas the shallow depolarization results from L-type Ca^{2+} current (Fig. 5.9C). An intermediate wave thus occurs.



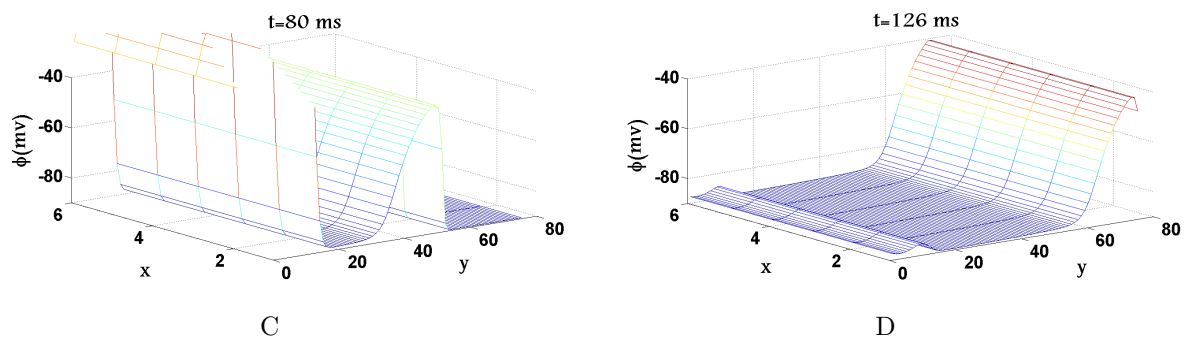


Figure 5.6: SAP. A sequence of snapshots illustrate ϕ at $t = 13$ ms (A), 51 ms (B), 80 ms (C) and 126 ms (D), respectively for $d_{\text{cleft}} = 3.5$ nm.

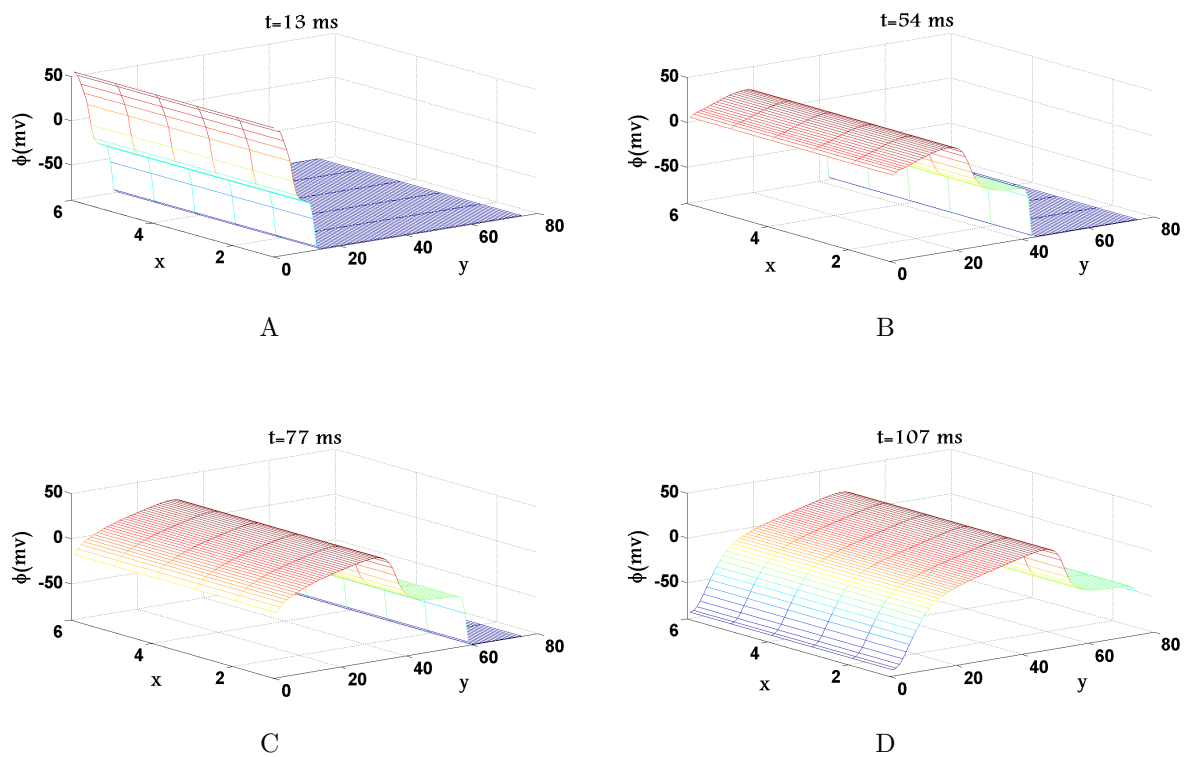
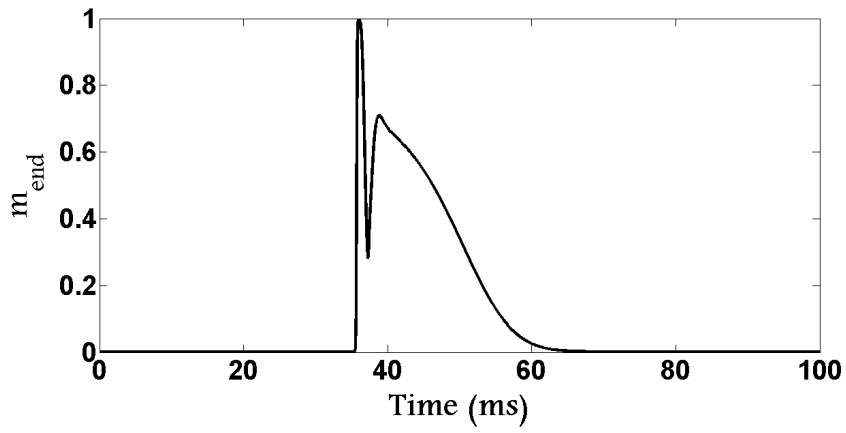
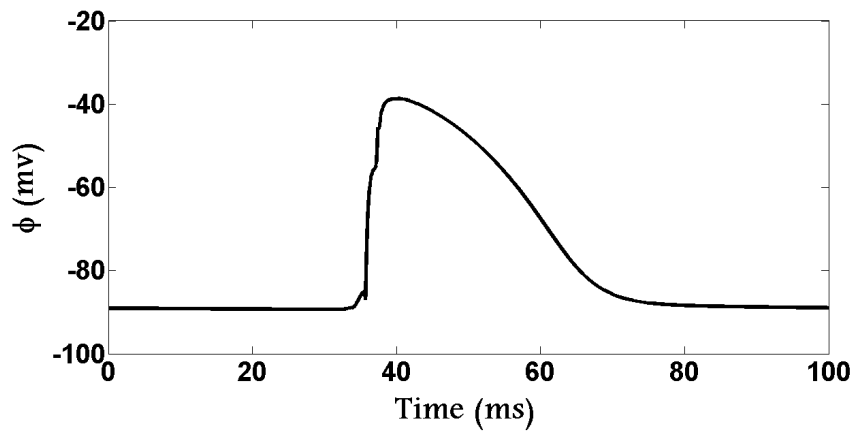


Figure 5.7: Intermediate wave. A sequence of snapshots illustrate ϕ at $t = 13$ ms (A), 54 ms (B), 77 ms (C) and 107 ms (D), respectively for $d_{\text{cleft}} = 3.8$ nm.



A



B

Figure 5.8: Activation gating variable (m) profile of Na^+ channels residing on the end membrane (A) and ϕ profile (B) of cell (3, 25) at $d_{\text{cleft}} = 3.5$ nm.

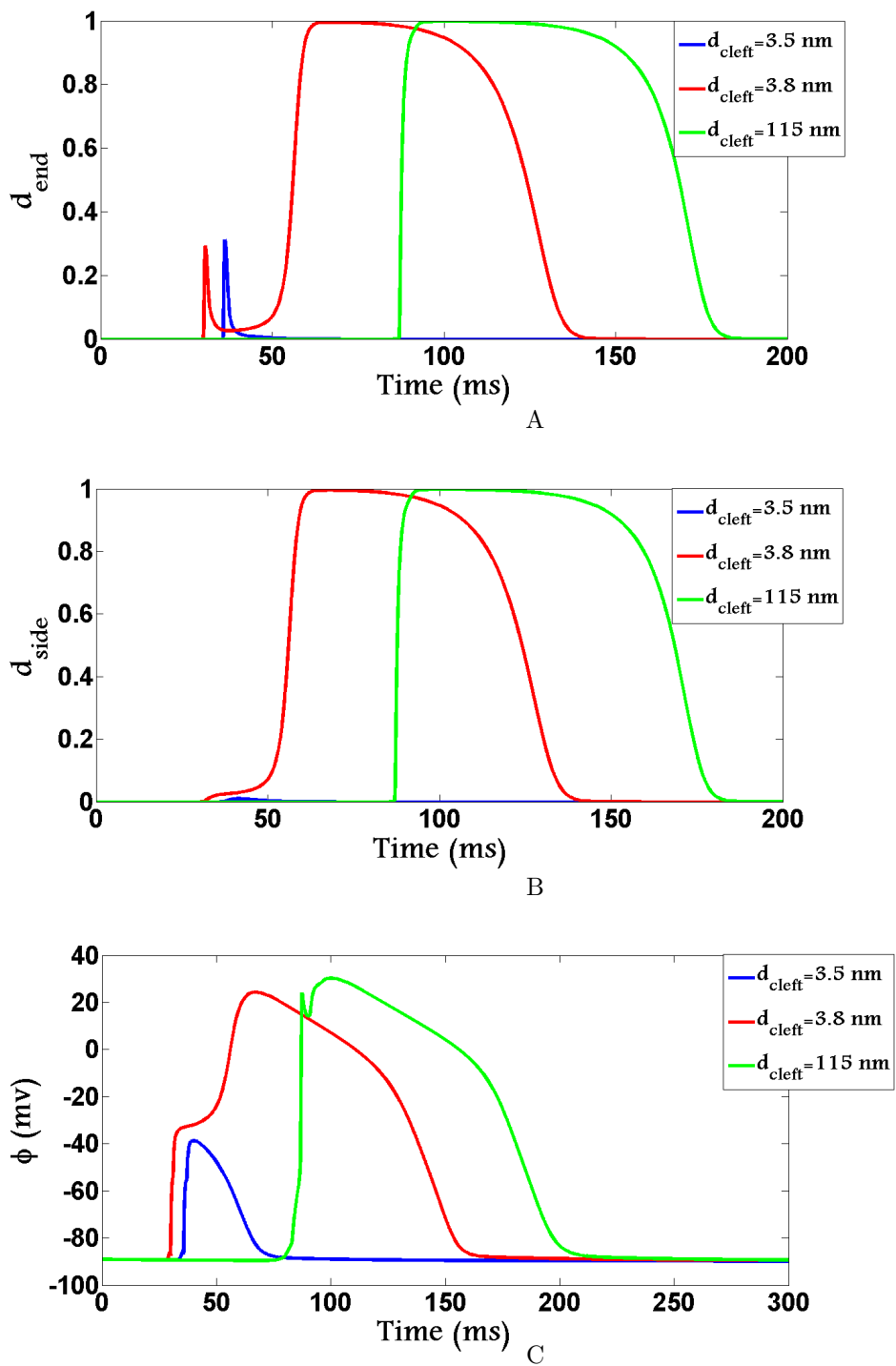


Figure 5.9: Activation gating variable (d) profile of L-type Ca^{2+} channels residing on the end (A), side (B) membranes and ϕ profile (C) of cell (3, 25), where $d_{\text{cleft}} = 3.5 \text{ nm}$ (blue), 3.8 nm (red), and 115 nm (green).

5.2.3 Conduction block (CB) in mixed genotype lattices.

In this section, we aim to investigate the possible impacts of interplay between heterogeneous Cx43 expression and ephaptic coupling on cardiac propagation, specially looking at the occurrence of CB. We perform numerical simulations in an $M \times N$ lattice with a random distribution of WT and Cx43 cells according to the predefined Cx43KO content ($0 \leq p \leq 1$), while incorporating different values of d_{cleft} . As stated in Sec. 5.1.2, $M = 2, 3, 6, 10$ and 16 , $N = 75$.

For each lattice, numerical simulations are implemented 100 iterations for every p , d_{cleft} and Na^+ channel distribution, thus taking into account different realizations of cellular architecture.

Ephaptic coupling can suppress CB when $p \geq 0.7$.

Tables 5.2 and 5.3 show the number of CB observed for different p and d_{cleft} in 2×75 and 3×75 lattices, respectively. Note that there is no CB for monogenotypic preparations ($p = 0$ or 1). However, co-culturing of Cx43KO and WT cells results in increased probabilities of CB, especially for $0.2 \leq p \leq 0.6$. This is consistent with the results of [47], where CB is studied without ephaptic coupling (corresponding to $d_{\text{cleft}} = 115$ nm in our simulations). Tables 5.2 and 5.3 indicate that the proportion of CB in the above range is independent of the value of d_{cleft} and thus of ephaptic coupling.

The number of CB in Tables 5.2 and 5.3, however, shows a dependency on d_{cleft} when $0.7 \leq p \leq 0.9$. The proportion of CB for $d_{\text{cleft}} = 8$ nm is lower than that for $d_{\text{cleft}} = 115$ nm. Indeed, in Table 5.2, for $0.7 \leq p \leq 0.8$, the differences in the number of CB at $d_{\text{cleft}} = 8$ nm and $d_{\text{cleft}} = 115$ nm are statistically significant according to two-proportion z -test ($z = 3.6$ and 2.5 , respectively). For $p = 0.9$, statistically significant difference ($z = 2.3$) can be detected if more than 800 numerical experiments are performed (data is not shown in Table 5.2). In Table 5.3, for $p = 0.7$, we observe statistically significant difference ($z = 3.3$) in the occurrence of CB between $d_{\text{cleft}} = 8$ nm and 115 nm. At $p = 0.8$, statistically significant difference ($z = 4.8$) can be observed when the number of numerical experiments is increased to 400 (data is not shown in Table 5.3). Recall that the maximum CV_L is achieved at $d_{\text{cleft}} = 8$ nm (see Fig. 5.2A) in the near absence of gap junctional coupling; and at $d_{\text{cleft}} = 115$ nm, propagation is mainly supported by

gap junctional coupling (see Section 5.2.1). When $0.7 \leq p \leq 0.9$, ephaptic coupling can thus reduce the number of CB, which points to an advantage of ephaptic coupling.

Recall from Sec. 5.2.2 that SAP occurs at $d_{\text{cleft}} = 3.5$ nm when $p = 1$. At $p = 0.9$ and $d_{\text{cleft}} = 3.5$ nm in Tables 5.2 and 5.3, SAP is seen when there is no CB.

Ephaptic coupling can enhance CB when $0.4 \leq p \leq 0.6$.

Tables 5.4 - 5.6 show the number of CB for different p and d_{cleft} in 6×75 , 10×75 and 16×75 lattices, respectively. Note that CB is never observed in monogenotypic preparations ($p = 0$ or 1). Nevertheless, similarly to simulations discussed in the previous section, conduction is susceptible to CB in preparations with mixed WT and Cx43KO cells, especially for $0.4 \leq p \leq 0.6$. This is seen for all ephaptic coupling strengths and lattice widths.

It can be seen from Tables 5.2 - 5.6 that the number of CB generally decreases as the lattice becomes wider. This is most likely because the presence of a larger number of alternative pathways for propagation in wider lattices permits the wavefront to bypass sites of low excitability. Exceptions to this rule are seen when $p = 0.9$, $d_{\text{cleft}} = 2$ nm and 3.5 nm. When $d_{\text{cleft}} = 2$ nm, the number of CB increases in wider lattices. When $d_{\text{cleft}} = 3.5$ nm, the number of CB displays an irregular dependency on the width of the lattice. The mechanism behind the phenomena is still unclear, but the unexplained variations are statistically significant.

The alleviatory effect of ephaptic coupling on CB in narrower lattices shown in Tables 5.2 and 5.3 (discussed in the previous section) is also present in wider lattices (Tables 5.4 - 5.6, $0.7 \leq p \leq 0.9$). The magnitude of this effect, seems to be smaller, however.

A new feature observed in wider lattices but not seen in narrower lattices is that the number of CB shows a dependency on d_{cleft} when $0.4 \leq p \leq 0.6$. As seen in Tables 5.4 - 5.6 the proportion of CB is *lower* at $d_{\text{cleft}} = 115$ nm than at smaller d_{cleft} . This implies that ephaptic coupling does not prevent, but rather, facilitates CB in this parameter range. Indeed, in Table 5.6, for $0.4 \leq p \leq 0.6$, the differences in the number of CB at $d_{\text{cleft}} = 115$ nm and smaller d_{cleft} are statistically significant according to the two-proportion z -test. Additionally, in Table 5.5, when $0.4 \leq p \leq 0.6$, the statistically significant differences in the occurrence of CB between $d_{\text{cleft}} = 115$ nm and $d_{\text{cleft}} =$

8 nm or 8.5 nm can be detected if 400 numerical experiments are performed (data is not shown in Table 5.5). In Table 5.4, for $p = 0.6$, a statistically significant difference between $d_{\text{cleft}} = 115$ nm and 8 nm can be seen if the number of numerical experiments is increased to 400 (data is not shown in Table 5.4). Ephaptic coupling can thus increase the possibility of CB in the co-cultures, which points to a disadvantage of ephaptic coupling. We see that this effect is more pronounced in wider lattices.

When $p = 0.9$, SAP still occurs at $d_{\text{cleft}} = 3.5$ nm in Tables 5.4 and 5.5, but the number of occurrences of CB is 2 and 1, respectively.

We have checked that the effect of suppressing (Sec. 5.2.3) or promoting CB (Sec. 5.2.3) is only seen when Na^+ channels are localized to the cleft; indeed, when Na^+ channel is uniformly distributed, the number of CB is independent of d_{cleft} values and is almost the same as the numbers in Tables 5.2 - 5.6 for $d_{\text{cleft}} = 115$ nm (data is not shown). This implies that ephaptic coupling does not modulate CB when Na^+ channel distribution is uniform.

Table 5.2: Number of CB for a 2×75 lattice. For $0.7 \leq p \leq 0.8$, the differences in the number of CB at $d_{\text{cleft}} = 8$ nm and $d_{\text{cleft}} = 115$ nm are statistically significant according to the two-proportions z -test ($z = 3.6$ and 2.5 , respectively). For $p = 0.9$, statistically significant difference ($z = 2.3$) can be detected if more than 800 numerical experiments are performed (data not shown).

| d_{cleft} (nm) \backslash p | 0 | 0.1 | 0.2 | 0.3 | 0.4 | 0.5 | 0.6 | 0.7 | 0.8 | 0.9 | 1 |
|--|---|-----|-----|-----|-----|-----|-----|-----------|-----------|----------|-----|
| 2 | 0 | 93 | 100 | 100 | 100 | 100 | 100 | 100 | 100 | 74 | 0 |
| 3.5 | 0 | 92 | 100 | 100 | 100 | 100 | 100 | 100 | 100 | 78 | SAP |
| 8 | 0 | 92 | 100 | 100 | 100 | 100 | 95 | 55 | 16 | 3 | 0 |
| 8.5 | 0 | 92 | 100 | 100 | 100 | 100 | 95 | 55 | 18 | 4 | 0 |
| 115 | 0 | 92 | 100 | 100 | 100 | 100 | 99 | 79 | 31 | 5 | 0 |

Table 5.3: Number of CB for a 3×75 lattice. For $p = 0.7$, according to the two-proportion z -test, we observe statistically significant difference ($z = 3.3$) in the occurrence of CB between $d_{\text{cleft}} = 8$ nm and 115 nm. At $p = 0.8$, statistically significant difference ($z = 4.8$) can be observed when the number of numerical experiments is increased to 400 (data not shown).

| d_{cleft} (nm) \backslash p | 0 | 0.1 | 0.2 | 0.3 | 0.4 | 0.5 | 0.6 | 0.7 | 0.8 | 0.9 | 1 |
|--|---|-----|-----|-----|-----|-----|-----|-----------|----------|-----|-----|
| 2 | 0 | 48 | 99 | 100 | 100 | 100 | 100 | 100 | 100 | 80 | 0 |
| 3.5 | 0 | 35 | 94 | 100 | 100 | 100 | 100 | 100 | 100 | 83 | SAP |
| 8 | 0 | 35 | 93 | 100 | 100 | 100 | 98 | 46 | 3 | 0 | 0 |
| 8.5 | 0 | 35 | 93 | 100 | 100 | 100 | 97 | 51 | 5 | 0 | 0 |
| 115 | 0 | 35 | 94 | 100 | 100 | 100 | 99 | 69 | 10 | 1 | 0 |

Table 5.4: Number of CB for a 6×75 lattice, For $p = 0.6$, there are statistically significant differences in the occurrence of CB between $d_{\text{cleft}} = 115$ nm and $d_{\text{cleft}} = 2$ nm, 3.5 nm or 8 nm. In particular, the significant differences between $d_{\text{cleft}} = 115$ nm and $d_{\text{cleft}} = 8$ nm can be detected if 400 numerical experiments are performed (data not shown).

| d_{cleft} (nm) \backslash p | 0 | 0.1 | 0.2 | 0.3 | 0.4 | 0.5 | 0.6 | 0.7 | 0.8 | 0.9 | 1 |
|--|---|-----|-----|-----|-----|-----|------------|-----|-----|-----|-----|
| 2 | 0 | 15 | 97 | 100 | 100 | 100 | 100 | 100 | 100 | 79 | 0 |
| 3.5 | 0 | 0 | 25 | 91 | 100 | 100 | 100 | 100 | 98 | 93 | SAP |
| 8 | 0 | 0 | 24 | 88 | 100 | 100 | 81 | 23 | 1 | 0 | 0 |
| 8.5 | 0 | 0 | 24 | 88 | 100 | 99 | 74 | 14 | 0 | 0 | 0 |
| 115 | 0 | 0 | 24 | 87 | 99 | 100 | 72 | 18 | 2 | 0 | 0 |

Table 5.5: Number of CB for a 10×75 lattice. When $0.4 \leq p \leq 0.6$, there are statistically significant differences in the number of CB at $d_{\text{cleft}} = 115$ and smaller d_{cleft} . In particular, the statistically significant differences between $d_{\text{cleft}} = 115$ nm and $d_{\text{cleft}} = 8$ nm or 8.5 nm can be detected if 400 numerical experiments are performed (data not shown).

| d_{cleft} (nm) \backslash p | 0 | 0.1 | 0.2 | 0.3 | 0.4 | 0.5 | 0.6 | 0.7 | 0.8 | 0.9 | 1 |
|--|---|-----|-----|-----|------------|------------|------------|-----|-----|-----|-----|
| 2 | 0 | 4 | 89 | 100 | 100 | 100 | 100 | 100 | 100 | 92 | 0 |
| 3.5 | 0 | 0 | 3 | 74 | 100 | 100 | 100 | 100 | 52 | 54 | SAP |
| 8 | 0 | 0 | 1 | 41 | 97 | 99 | 64 | 0 | 0 | 0 | 0 |
| 8.5 | 0 | 0 | 1 | 40 | 96 | 96 | 40 | 0 | 0 | 0 | 0 |
| 115 | 0 | 0 | 1 | 39 | 92 | 86 | 31 | 0 | 0 | 0 | 0 |

Table 5.6: Number of CB for a 16×75 lattice. When $0.4 \leq p \leq 0.6$, the number of CB at $d_{\text{cleft}} = 115$ nm is significantly less than at smaller d_{cleft} .

| d_{cleft} (nm) \backslash p | 0 | 0.1 | 0.2 | 0.3 | 0.4 | 0.5 | 0.6 | 0.7 | 0.8 | 0.9 | 1 |
|--|---|-----|-----|-----|------------|------------|------------|-----|-----|-----|-----|
| 2 | 0 | 2 | 89 | 100 | 100 | 100 | 100 | 100 | 100 | 99 | 0 |
| 3.5 | 0 | 0 | 1 | 56 | 100 | 100 | 100 | 98 | 37 | 43 | SAP |
| 8 | 0 | 0 | 0 | 12 | 83 | 99 | 50 | 0 | 0 | 0 | 0 |
| 8.5 | 0 | 0 | 0 | 10 | 79 | 97 | 27 | 0 | 0 | 0 | 0 |
| 115 | 0 | 0 | 0 | 7 | 59 | 53 | 8 | 0 | 0 | 0 | 0 |

5.2.4 Mechanisms behind the increased proportions of CB.

As demonstrated in Sec. 5.2.3, a smaller d_{cleft} can either prevent or promote CB depending on parameter range. In wider lattices, CB is more frequent in the presence of ephaptic coupling when $0.4 \leq p \leq 0.6$.

We now explore the mechanism behind this observation by using a representative example of 6×75 lattice at $p = 0.6$. A similar analysis can be performed in other cases as well. In Figs. 5.10 - 5.13, EAT is plotted at different iterations ($i = 9, 20, 35, 50$,

respectively). In Figs. 5.10A, 5.11A, 5.12A, and 5.13A, $d_{\text{cleft}} = 2$ nm, 3.5 nm, 8 nm and 8.5 nm, respectively. In Figs. 5.10B, 5.11B, 5.12B and 5.13B, $d_{\text{cleft}} = 115$ nm. In each figure, panels A and B have the same distribution of Cx43 expression. We plot EAT for instances in which CB is seen in the presence of ephaptic coupling ($d_{\text{cleft}} = 2$ nm, 3.5 nm, 8 nm, 8.5 nm) but not in its absence ($d_{\text{cleft}} = 115$ nm). At the location where CB is observed (denoted by $\text{EAT} = 0$) when ephaptic coupling is present (solid box in panel A), there is always a plateau phase of EAT when ephaptic coupling is absent (solid box in panel B). Similarly, when there is a gap in EAT in the presence of ephaptic coupling (dashed box in panel A), a plateau phase in the EAT is seen in its absence (dashed box in panel B). This implies the presence of relatively large cell clusters that are excited almost simultaneously when ephaptic coupling is absent, but are difficult or impossible to excite when ephaptic coupling is present.

In light of the foregoing, we may describe the mechanism as follows. For $0.4 \leq p \leq 0.6$, Cx43KO and WT cells are mixed in roughly equal proportion. The random distribution of cell genotypes results in local clusters of WT cells coupled through normal levels of gap junctions, which form electric loads that may substantially impair the conduction. When an action potential propagates into such cell clusters, the electric loads can lead to delayed activation or even CB if the activating current is not sufficiently strong.

In the presence of ephaptic coupling (at smaller d_{cleft}), R_c is high, and the cleft potential may drop low enough to excite the end membrane of cell downstream, but the resulting inward current may not be sufficient to excite the entire cell. The high resistance creates a bottleneck that limits the amount of current into the cleft space and across the end membrane of neighboring cell. Ephaptic coupling may thus lead to a decrease in activating current for cells downstream, which together with the increased load discussed above (when $0.4 \leq p \leq 0.6$), may result in a prominent current-to-load mismatch.

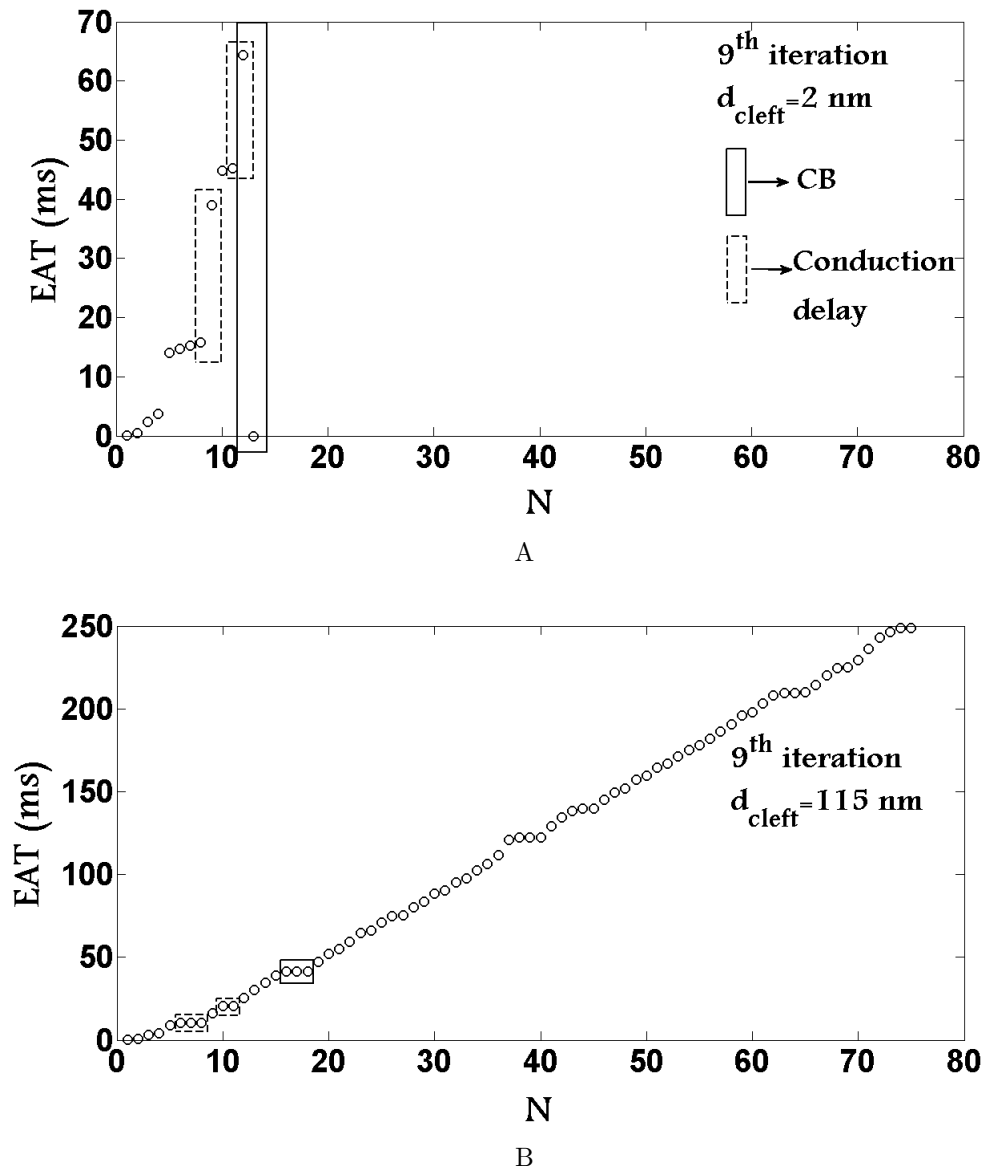


Figure 5.10: Representative plots of EAT along a 6×75 lattice at the 9th iteration, where $p = 0.6$, $d_{\text{cleft}} = 2 \text{ nm}$ (A), 115 nm (B). Conduction delays and CB (A) are denoted by dashed and solid boxes, respectively. Plateau phase of EAT (B) corresponding to conduction delays and CB are denoted by dash and solid boxes, respectively.

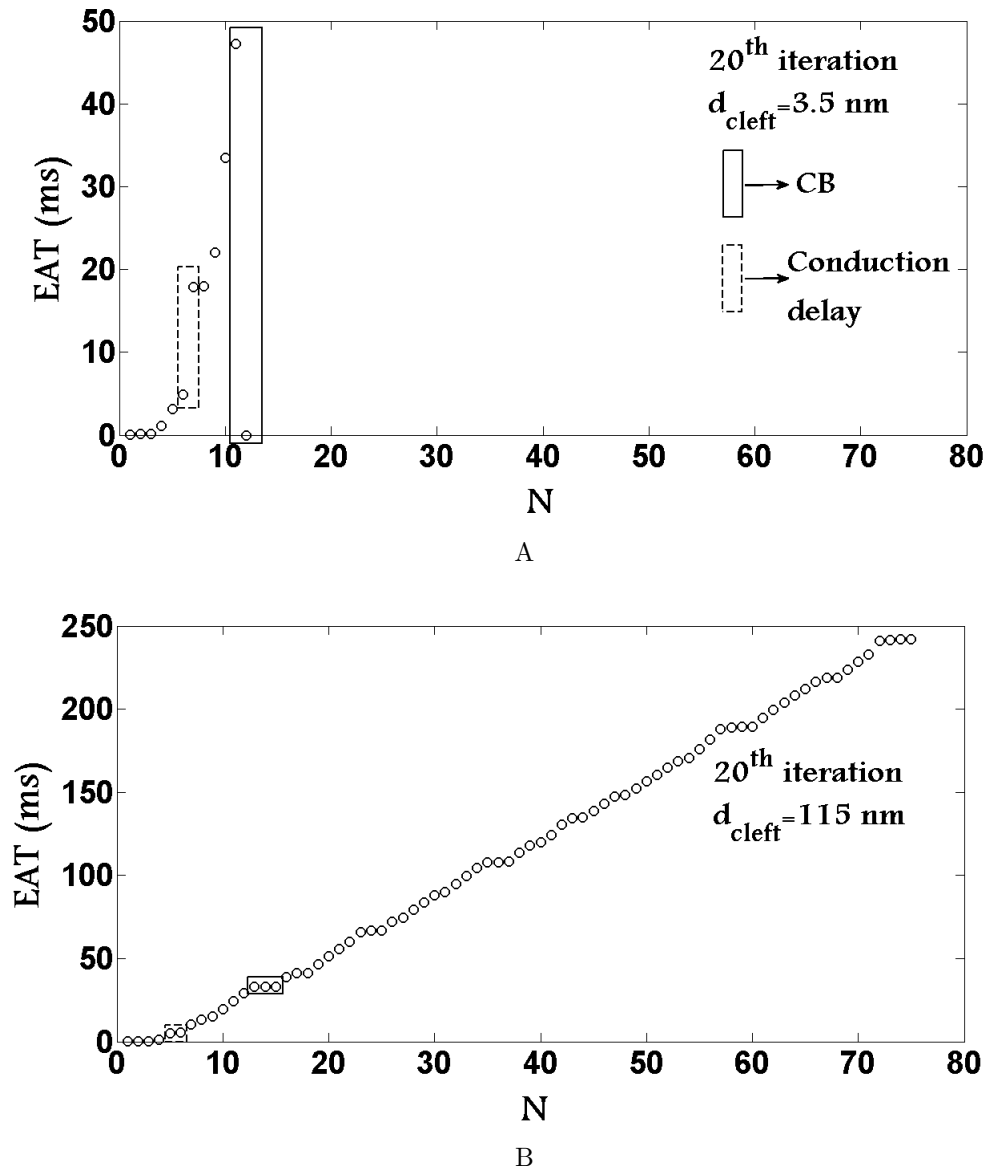


Figure 5.11: Representative plots of EAT along a 6×75 lattice at the 20th iteration, where $p = 0.6$, $d_{\text{cleft}} = 3.5$ nm (A), 115 nm (B). Conduction delays and CB (A) are denoted by dashed and solid boxes, respectively. Plateau phase of EAT (B) corresponding to conduction delays and CB are denoted by dash and solid boxes, respectively.

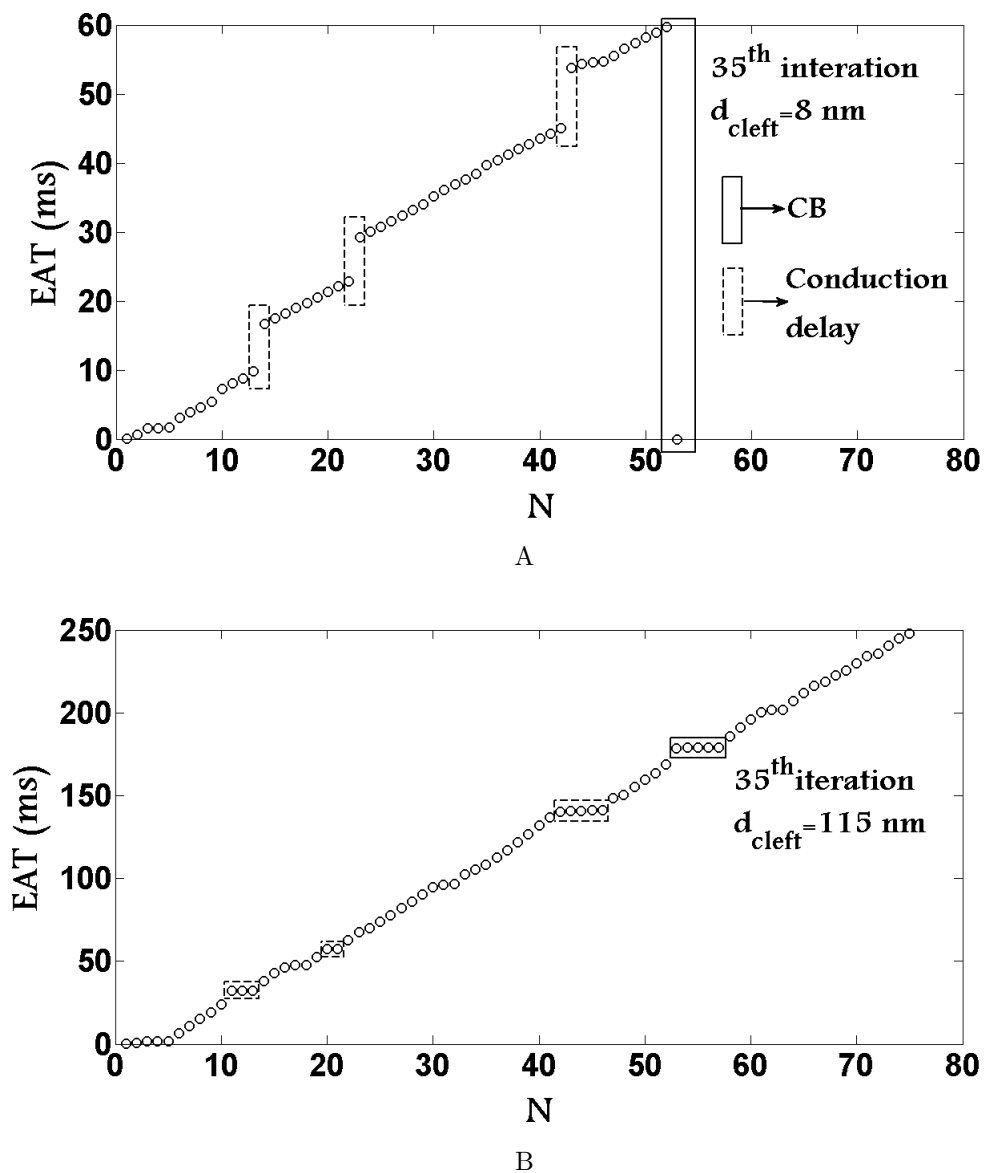


Figure 5.12: Representative plots of EAT along a 6×75 lattice at the 35th iteration, where $p = 0.6$, $d_{\text{cleft}} = 8 \text{ nm}$ (A), 115 nm (B). Conduction delays and CB (A) are denoted by dashed and solid boxes, respectively. Plateau phase of EAT (B) corresponding to conduction delays and CB are denoted by dash and solid boxes, respectively.

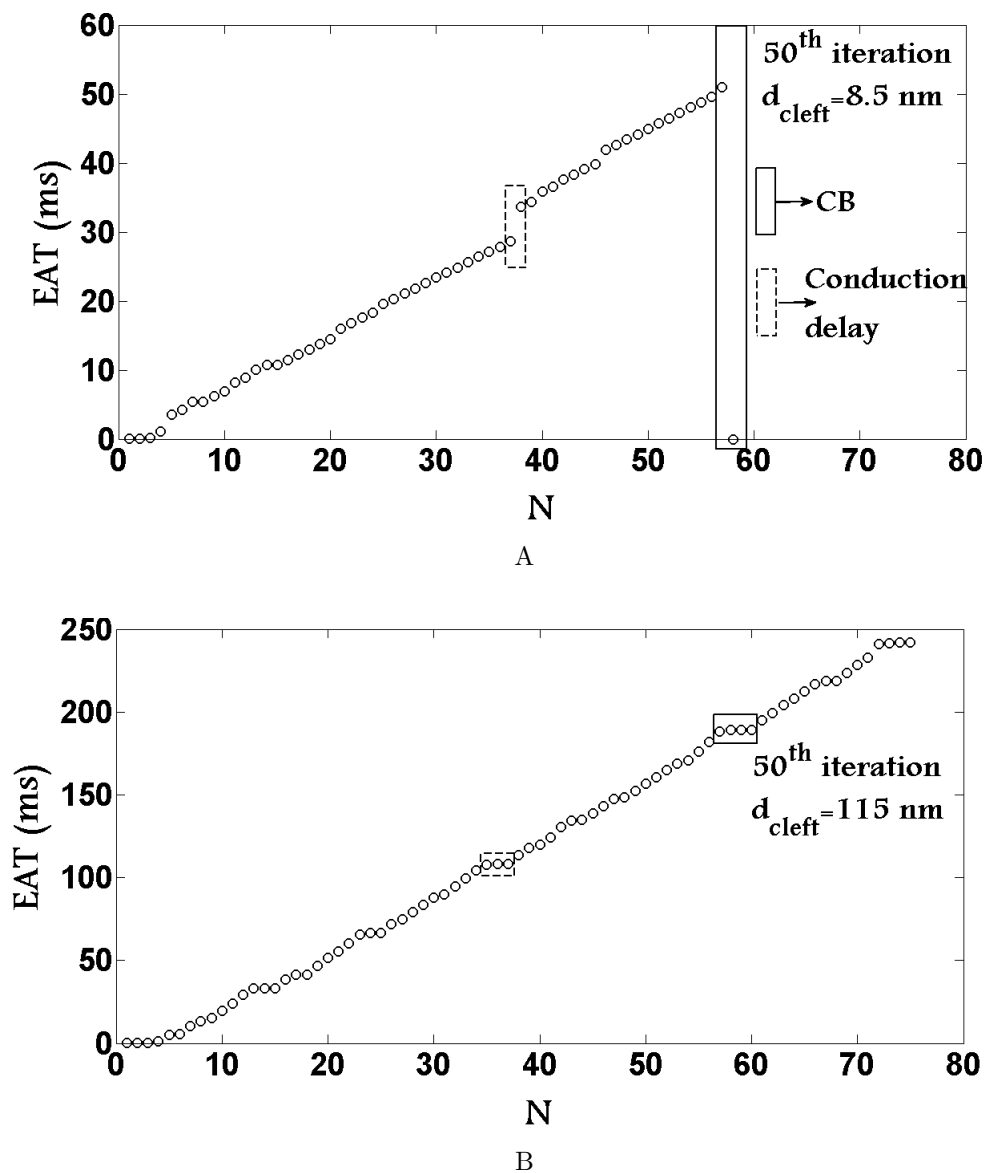


Figure 5.13: Representative plots of EAT along a 6×75 lattice at the 50th iteration, where $p = 0.6$, $d_{\text{cleft}} = 8.5 \text{ nm}$ (A), 115 nm (B). Conduction delays and CB (A) are denoted by dashed and solid boxes, respectively. Plateau phase of EAT (B) corresponding to conduction delays and CB are denoted by dash and solid boxes, respectively.

5.3 Conclusions and discussions

In this chapter, we explore the interplay between reduced heterogeneous Cx43 expression and ephaptic coupling on cardiac action potential propagation. Under severely reduced Cx43 expression, we identify three new phenomena in the presence of ephaptic coupling: alternating conduction, in which ephaptic and gap junction-mediated mechanisms alternate; instability of planar fronts; and SAP which has a smaller potential amplitude than the normal action potential. We then examine the effects of heterogeneous Cx43 expression and ephaptic coupling on CB using a 2D cell lattice as our model system. We find that ephaptic coupling can either prevent or promote CB depending on the Cx43KO content. When Cx43KO content is relatively high ($0.7 \leq p \leq 0.9$), ephaptic coupling reduces the possibilities of CB, an effect that is greater in narrower lattices. In wider lattices, ephaptic coupling promotes CB when the Cx43KO content $0.4 \leq p \leq 0.6$. This increase in the probabilities of CB can be attributed to an increase in current-to-load mismatch.

We demonstrate the biphasic behavior of CV_L as a function of d_{cleft} when Cx43KO content is 100% (Sec. 5.2.1). This nonmonotonicity of CV_L qualitatively agrees with previously published results shown in [10, 11]. In [10], the maximal CV_L (15 cm/s) under 1% of normal gap junction is achieved at $d_{\text{cleft}} = 40$ nm. In [11], the maximal CV_L (20 cm/s) is obtained at $d_{\text{cleft}} = 11$ nm under 1% of normal gap junction expression. Although the optimal d_{cleft} values are quantitatively different from ours, the qualitative behavior of CV_L is similar.

This is the first study to examine the interaction between heterogeneous Cx43 expression and ephaptic coupling on the occurrence of CB (Sec. 5.2.3). CB, especially unidirectional CB (UCB) has been considered a substrate for fatal reentrant arrhythmias and sudden cardiac death [72]. Therefore, over the last decades, CB or UCB has become the major focus of research. We report that ephaptic mechanism can lower the possibilities of CB when Cx43KO content $p \geq 0.7$, which implies an anti-arrhythmic role of ephaptic coupling when gap junctions are reduced. This finding is consistent with the result shown in Fig. 5.2A of Sec. 5.2.1 and earlier numerical ([11, 12, 52]) and experimental results ([6, 10, 57]), which suggest that ephaptic coupling can increase conduction speed when gap junction expression is low. On the other hand, we

show that ephaptic coupling can increase the proportion of CB when Cx43KO content $0.4 \leq p \leq 0.6$, which points to a disadvantageous role of ephaptic coupling in this context. This finding is also consistent with the result shown in Fig. 5.2B of Sec. 5.2.1, which suggests that ephaptic coupling can reduce conduction velocity when gap junctional coupling is sufficiently high. It is notable that similar results have been reported elsewhere in [10, 11, 12, 52]. It is important to note, however, that previous papers [6, 10, 11, 12, 52, 57] studied ephaptic coupling by examining its effect on conduction speed with a homogeneous change in gap junctional conductance. Our study focus on the reliability of cardiac signal propagation by studying CB in the presence of heterogeneous Cx43 expression.

Finally, we mention that all the effects of ephaptic coupling mentioned in our findings (results in Sec. 5.2) are shown to be highly dependent on the localized Na^+ channels, which are consistent with the experimental and numerical results in [10, 11, 12, 49, 50, 51, 73].

In this chapter, we adopt a simplified geometry, cell discretization (each cell is treated to be isopotential) and arrangement of cells. We believe that using realistic cell shape or delicate cell arrangement ([47, 12]) will not qualitatively change our conclusions, but may lead to new phenomena. Although we identify some important features of conduction, alternating conduction, instability of planar fronts and SAP, the detailed mechanisms behind these phenomena are still unclear. A future study with simplified models may allow us to obtain better understanding. Finally, we mention that the role of Cx43 may not be restricted to electrical conduction, as suggested in [74]. This is beyond the scope of our current paper, and is a subject for future study.

References

- [1] Sandeep K Goyal and Jeffrey N Rottman. Ventricular fibrillation. *Medscape*.
- [2] Alain Karma. Electrical alternans and spiral wave breakup in cardiac tissue. *Chaos*, 4(3):461–472, 1994.
- [3] Alan Garfinkel, Young-Hoon Kim, Olga Voroshilovsky, Zhilin Qu, Jong R Kil, Moon-Hyoung Lee, Hrayr S Karagueuzian, James N Weiss, and Peng-Sheng Chen. Preventing ventricular fibrillation by flattening cardiac restitution. *Proc.Natl.Acad.Sci.*, 97(11):6061–6066, 2000.
- [4] Stephen A Gaeta and David J Christini. Non-linear dynamics of cardiac alternans: subcellular to tissue-level mechanisms of arrhythmia. *Front. Physiol.*, 3:157, 2012.
- [5] Lance D Wilson and David S Rosenbaum. Mechanisms of arrhythmogenic cardiac alternans. *Europace*, 9(suppl 6):vi77–vi82, 2007.
- [6] Jian-An Yao, David E Gutstein, Fangyu Liu, Glenn I Fishman, and Andrew L Wit. Cell coupling between ventricular myocyte pairs from connexin43-deficient murine hearts. *Circ. Res.*, 93(8):736–743, 2003.
- [7] David E Gutstein, Gregory E Morley, Houman Tamaddon, Dhananjay Vaidya, Michael D Schneider, Ju Chen, Kenneth R Chien, Heidi Stuhlmann, and Glenn I Fishman. Conduction slowing and sudden arrhythmic death in mice with cardiac-restricted inactivation of connexin43. *Circ. Res.*, 88(3):333–339, 2001.
- [8] Nick Sperelakis and James E Mann. Evaluation of electric field changes in the cleft between excitable cells. *J. Theor. Biol*, 64(1):71–96, 1977.

- [9] David E Gutstein, Gregory E Morley, Dhananjay Vaidya, Fangyu Liu, Franklin L Chen, Heidi Stuhlmann, and Glenn I Fishman. Heterogeneous expression of gap junction channels in the heart leads to conduction defects and ventricular dysfunction. *Circulation*, 104(10):1194–1199, 2001.
- [10] Jan P Kucera, Stephan Rohr, and Yoram Rudy. Localization of sodium channels in intercalated disks modulates cardiac conduction. *Circ. Res*, 91(12):1176–1182, 2002.
- [11] Paul E Hand and Charles S Peskin. Homogenization of an electrophysiological model for a strand of cardiac myocytes with gap-junctional and electric-field coupling. *Bull. Math. Biol.*, 72(6):1408–1424, 2010.
- [12] Joyce Lin and James P Keener. Microdomain effects on transverse cardiac propagation. *Biophys. J.*, 106(4):925–931, 2014.
- [13] Leonid M Livshitz and Yoram Rudy. Regulation of ca^{2+} and electrical alternans in cardiac myocytes: role of $camkii$ and repolarizing currents. *Am. J. Physiol. Heart Circ. Physiol.*, 292(6):H2854–H2866, 2007.
- [14] JB Nolasco and Roger W Dahlen. A graphic method for the study of alternation in cardiac action potentials. *J. Appl. Physiol.*, 25(2):191–196, 1968.
- [15] MR Guevara, G Ward, A Shrier, and L Glass. Electrical alternans and period doubling bifurcations. *IEEE. Comp. Cardiol.*, 562:167–170, 1984.
- [16] A Petrie and X Zhao. Estimating eigenvalues of dynamical systems from time series with applications to predicting cardiac alternans. *Proc. R. Soc. A*, 468:3649–3666, 2012.
- [17] Michael R Franz. The electrical restitution curve revisited: steep or flat slope—which is better? *J. Cardiovasc. Electrophysiol.*, 14(s10):S140–S147, 2003.
- [18] James N Weiss, Alain Karma, Yohannes Shiferaw, Peng-Sheng Chen, Alan Garfinkel, and Zhilin Qu. From pulsus to pulseless the saga of cardiac alternans. *Circ. Res.*, 98(10):1244–1253, 2006.

- [19] Joseph M Pastore, Steven D Girouard, Kenneth R Laurita, Fadi G Akar, and David S Rosenbaum. Mechanism linking t-wave alternans to the genesis of cardiac fibrillation. *Circulation*, 99(10):1385–1394, 1999.
- [20] Douglas P Zipes and Hein JJ Wellens. Sudden cardiac death. *Circulation*, 98(21):2334–2351, 1998.
- [21] Robert J Myerburg and Peter M Spooner. Opportunities for sudden death prevention: directions for new clinical and basic research. *Cardiovasc. Res.*, 50(2):177–185, 2001.
- [22] Joseph M Pastore and David S Rosenbaum. Role of structural barriers in the mechanism of alternans-induced reentry. *Circ. Res.*, 87(12):1157–1163, 2000.
- [23] Etienne J Pruvot and David S Rosenbaum. T-wave alternans for risk stratification and prevention of sudden cardiac death. *Curr. Cardiol. Rep.*, 5(5):350–357, 2003.
- [24] Masaomi Chinushi, Dmitry Kozhevnikov, Edward B Caref, Mark Restivo, and Nabil El-Sherif. Mechanism of discordant t wave alternans in the in vivo heart. *J. Cardiovasc. Electrophysiol.*, 14(6):632–638, 2003.
- [25] Joseph M Pastore, Kenneth R Laurita, and David S Rosenbaum. Importance of spatiotemporal heterogeneity of cellular restitution in mechanism of arrhythmogenic discordant alternans. *Heart Rhythm*, 3(6):711–719, 2006.
- [26] Mari A Watanabe, Flavio H Fenton, Steven J Evans, Harold M Hastings, and Alain Karma. Mechanisms for discordant alternans. *J. Cardiovasc. Electrophysiol.*, 12(2):196–206, 2001.
- [27] Zhilin Qu, Alan Garfinkel, Peng-Sheng Chen, and James N Weiss. Mechanisms of discordant alternans and induction of reentry in simulated cardiac tissue. *Circulation*, 102(14):1664–1670, 2000.
- [28] Flavio H Fenton, Elizabeth M Cherry, Harold M Hastings, and Steven J Evans. Multiple mechanisms of spiral wave breakup in a model of cardiac electrical activity. *Chaos*, 12(3):852–892, 2002.

- [29] Jeffrey J Fox, Mark L Riccio, Fei Hua, Eberhard Bodenschatz, and Robert F Gilmour. Spatiotemporal transition to conduction block in canine ventricle. *Circ. Res.*, 90(3):289–296, 2002.
- [30] Peter Taggart, Peter Sutton, Zaid Chalabi, Mark R Boyett, Ron Simon, Donna Elliott, and Jaswinder S Gill. Effect of adrenergic stimulation on action potential duration restitution in humans. *Circulation*, 107(2):285–289, 2003.
- [31] Daisuke Sato, Donald M Bers, and Yohannes Shiferaw. Formation of spatially discordant alternans due to fluctuations and diffusion of calcium. *PLoS ONE*, 8(12):e85365, 2013.
- [32] Sergey Mironov, José Jalife, and Elena G Tolkacheva. Role of conduction velocity restitution and short-term memory in the development of action potential duration alternans in isolated rabbit hearts. *Circulation*, 118(1):17–25, 2008.
- [33] Hideki Hayashi, Yohannes Shiferaw, Daisuke Sato, Motoki Nihei, Shien-Fong Lin, Peng-Sheng Chen, Alan Garfinkel, James N Weiss, and Zhilin Qu. Dynamic origin of spatially discordant alternans in cardiac tissue. *Biophys. J.*, 92(2):448–460, 2007.
- [34] A Gizzi, E. M. Cherry, R. F. Gilmour Jr, S Luther, S Filippi, and F. H Fenton. Effects of pacing site and stimulation history on alternans dynamics and the development of complex spatiotemporal patterns in cardiac tissue. *Front. Physiol.*, 4:71, 2013.
- [35] Elena G Tolkacheva, Mónica M Romeo, Marie Guerraty, and Daniel J Gauthier. Condition for alternans and its control in a two-dimensional mapping model of paced cardiac dynamics. *Phys. Rev. E*, 69(3):031904, 2004.
- [36] Ning Wei, Yoichiro Mori, and Elena G Tolkacheva. The role of short term memory and conduction velocity restitution in alternans formation. *J. Theor. Biol.*, 367:21–28, 2015.
- [37] Jeffrey J Fox, Eberhard Bodenschatz, and Robert F Gilmour Jr. Period-doubling instability and memory in cardiac tissue. *Phys. Rev. Lett.*, 89(13):138101, 2002.

- [38] Elena G Tolkacheva and Xiaopeng Zhao. Nonlinear dynamics of periodically paced cardiac tissue. *Nonlinear Dyn.*, 68(3):347–363, 2012.
- [39] Jeffrey J Fox, Mark L Riccio, Paul Drury, Amanda Werthman, and Robert F Gilmour Jr. Dynamic mechanism for conduction block in heart tissue. *New J. Phys.*, 5(1):101–114, 2003.
- [40] Blas Echebarria and Alain Karma. Amplitude equation approach to spatiotemporal dynamics of cardiac alternans. *Phys. Rev. E*, 76(5):051911, 2007.
- [41] Blas Echebarria and Alain Karma. Instability and spatiotemporal dynamics of alternans in paced cardiac tissue. *Phys. Rev. Lett.*, 88(20):208101, 2002.
- [42] Niels F Otani. Theory of action potential wave block at-a-distance in the heart. *Phys. Rev. E*, 75(2):021910, 2007.
- [43] Lloyd M Davis, Mark E Rodefeld, Karen Green, Eric C Beyer, and Jeffrey E Saffitz. Gap junction protein phenotypes of the human heart and conduction system. *J. Cardiovasc. Electrophysiol.*, 6(10):813–822, 1995.
- [44] Stephan B Danik, Fangyu Liu, Jie Zhang, H Jacqueline Suk, Gregory E Morley, Glenn I Fishman, and David E Gutstein. Modulation of cardiac gap junction expression and arrhythmic susceptibility. *Circ. Res.*, 95(10):1035–1041, 2004.
- [45] Habo J Jongsma and Ronald Wilders. Gap junctions in cardiovascular disease. *Circ. Res.*, 86(12):1193–1197, 2000.
- [46] Shigeto Kanno and Jeffrey E Saffitz. The role of myocardial gap junctions in electrical conduction and arrhythmogenesis. *Cardiovasc. Pathol.*, 10(4):169–177, 2001.
- [47] Yann Prudat and Jan P Kucera. Nonlinear behaviour of conduction and block in cardiac tissue with heterogeneous expression of connexin 43. *J. Mol. Cell. Cardiol.*, 76:46–54, 2014.
- [48] Stephan Rohr. Role of gap junctions in the propagation of the cardiac action potential. *Cardiovasc. Res.*, 62(2):309–322, 2004.

- [49] Nicholas Sperelakis. An electric field mechanism for transmission of excitation between myocardial cells. *Circ. Res.*, 91(11):985–987, 2002.
- [50] Sidney A Cohen. Immunocytochemical localization of rh1 sodium channel in adult rat heart atria and ventricle presence in terminal intercalated disks. *Circulation*, 94(12):3083–3086, 1996.
- [51] Sebastian KG Maier, Ruth E Westenbroek, Kenneth A Schenkman, Eric O Feigl, Todd Scheuer, and William A Catterall. An unexpected role for brain-type sodium channels in coupling of cell surface depolarization to contraction in the heart. *Proc. Natl. Acad. Sci.*, 99(6):4073–4078, 2002.
- [52] Yoichiro Mori, Glenn I Fishman, and Charles S Peskin. Ephaptic conduction in a cardiac strand model with 3d electrodiffusion. *Proc. Natl. Acad. Sci.*, 105(17):6463–6468, 2008.
- [53] Rengasayee Veeraraghavan, Steven Poelzing, and Robert G Gourdie. Intercellular electrical communication in the heart: a new, active role for the intercalated disk. *Cell communication & adhesion*, 21(3):161–167, 2014.
- [54] Elizabeth D Copene and James P Keener. Ephaptic coupling of cardiac cells through the junctional electric potential. *J. Math. Biol.*, 57(2):265–284, 2008.
- [55] John B Picone, Nicholas Sperelakis, and James E Mann. Expanded model of the electric field hypothesis for propagation in cardiac muscle. *Math. Comput. Model.*, 15(8):17–35, 1991.
- [56] James Lin and James P Keener. Ephaptic coupling in cardiac myocytes. *IEEE Trans. Biomed. Eng.*, 60(2):576–582, 2013.
- [57] Rengasayee Veeraraghavan, Mohamed E Salama, and Steven Poelzing. Interstitial volume modulates the conduction velocity-gap junction relationship. *Am. J. Physiol. Heart Circ. Physiol.*, 302(1):H278–H286, 2012.
- [58] Xuejun Wang and A Martin Gerdes. Chronic pressure overload cardiac hypertrophy and failure in guinea pigs: Iii. intercalated disc remodeling. *J. Mol. Cell. Cardiol.*, 31(2):333–343, 1999.

- [59] XIAO-DI HUANG, George E Sandusky, and DOUGLES P ZIPES. Heterogeneous loss of connexin43 protein in ischemic dog hearts. *J. Cardiovasc. Electrophysiol.*, 10(1):79–91, 1999.
- [60] Masaaki Yoshida, Tomoko Ohkusa, Tadamitsu Nakashima, Hiroki Takanari, Masafumi Yano, Genzou Takemura, Haruo Honjo, Itsuo Kodama, Yoichi Mizukami, and Masunori Matsuzaki. Alterations in adhesion junction precede gap junction remodelling during the development of heart failure in cardiomyopathic hamsters. *Cardiovasc. Res.*, 92(1):95–105, 2011.
- [61] R Coronel, Ronald Wilders, Arie O Verkerk, Rob F Wiegeler, David Benoist, and Olivier Bernus. Electrophysiological changes in heart failure and their implications for arrhythmogenesis. *Biochimica et Biophysica Acta*, 1832(12):2432–2441, 2013.
- [62] Gordon F Tomaselli and Douglas P Zipes. What causes sudden death in heart failure? *Circ. Res.*, 95(8):754–763, 2004.
- [63] Ning Wei, Yoichiro Mori, and Elena G Tolkacheva. The dual effect of ephaptic coupling on cardiac conduction with heterogeneous expression of connexin 43. *J. Theor. Biol.*, 397:103–114, 2016.
- [64] Philippe Beauchamp, Thomas Desplantez, Megan L McCain, Weihui Li, Angeliki Asimaki, Ghislaine Rigoli, Kevin Kit Parker, Jeffrey E Saffitz, and Andre G Kleber. Electrical coupling and propagation in engineered ventricular myocardium with heterogeneous expression of connexin43. *Circ. Res.*, 110(11):1445–1453, 2012.
- [65] Megan L McCain, Thomas Desplantez, Nicholas A Geisse, Barbara Rothen-Rutishauser, Helene Oberer, Kevin Kit Parker, and Andre G Kleber. Cell-to-cell coupling in engineered pairs of rat ventricular cardiomyocytes: relation between cx43 immunofluorescence and intercellular electrical conductance. *Am. J. Physiol. Heart Circ. Physiol.*, 302(2):H443–H450, 2012.
- [66] Paul E Hand, Boyce E Griffith, and Charles S Peskin. Deriving macroscopic myocardial conductivities by homogenization of microscopic models. *Bull. Math. Biol.*, 71(7):1707–1726, 2009.

- [67] James Keener and James Sneyd. *Mathematical physiology: I: cellular physiology*, volume 1. Springer Science & Business Media, 2010.
- [68] Stephan Rohr, Jan P Kucera, and André G Kléber. Slow conduction in cardiac tissue, i effects of a reduction of excitability versus a reduction of electrical coupling on microconduction. *Circ. Res.*, 83(8):781–794, 1998.
- [69] Robin M Shaw and Yoram Rudy. Ionic mechanisms of propagation in cardiac tissue roles of the sodium and l-type calcium currents during reduced excitability and decreased gap junction coupling. *Circ. Res.*, 81(5):727–741, 1997.
- [70] Yoichiro Mori and Hiroshi Matano. Stability of front solutions of the bidomain equation. *Comm. Pure Appl. Math.*, In press, 2015.
- [71] Masato Iida, Roger Lui, and Hirokazu Ninomiya. Stacked fronts for cooperative systems with equal diffusion coefficients. *Siam J. Math. Anal.*, 43(3):1369–1389, 2011.
- [72] AL Waldo and AL Wit. Mechanisms of cardiac arrhythmias. *The Lancet*, 341(8854):1189–1193, 1993.
- [73] Rengasayee Veeraraghavan, Joyce Lin, Gregory S Hoeker, James P Keener, Robert G Gourdie, and Steven Poelzing. Sodium channels in the cx43 gap junction perinexus may constitute a cardiac ephapse: an experimental and modeling study. *Pflügers Arch.-Eur. J. Physiol.*, pages 1–13, 2014.
- [74] Indra Lübke-meier, Robert Pascal Requardt, Xianming Lin, Philipp Sasse, René Andrié, Jan Wilko Schrickel, Halina Chkourko, Feliksas F Bukauskas, Jung-Sun Kim, Marina Frank, et al. Deletion of the last five c-terminal amino acid residues of connexin43 leads to lethal ventricular arrhythmias in mice without affecting coupling via gap junction channels. *Basic Res. Cardiol.*, 108(3):1–16, 2013.
- [75] Alain Vinet. Quasiperiodic circus movement in a loop model of cardiac tissue: Multistability and low dimensional equivalence. *Ann. Biomed. Eng.*, 28(7):704–720, 2000.

Appendix A

Derivation of ξ and ω in chapter 3

Numerical solutions to Eq. (3.2) together with Eq. (3.4) develop unphysical spatial discontinuities along the cable, as observed in [41]. This can be avoided by considering the cell coupling effect, which contributes diffusion and advection terms, as has been suggested in [40, 41]. Therefore, in order to model a one dimensional cable, we adopt a spatially coupled mapping model Eq. (3.3) by adding diffusion and advection terms to Eq. (3.1), as suggested in [39].

Here, we discuss the values for ξ and ω that are used in Eq. (3.3) following [39]. An interpretation of ξ and ω can be found in [40]. The starting point is the following equation:

$$A_{n+1}(x) = (G * f)(x) = \int_{-\infty}^{+\infty} G(y)f[D_n(x - y)]dy. \quad (\text{A.1})$$

where $G(y)$ is some normalized asymmetrical kernel that expresses the diffusive coupling between neighboring cells. Let us define the Fourier transform ($\mathcal{F}(\cdot)$) of the kernel to be $(\mathcal{F}(G))(k) = \int_{-\infty}^{+\infty} G(y)e^{-iky}dy$. The exponential function in the above equation can be expanded in the form $e^{-iky} = 1 - iky - (ky)^2/2 + \dots$. It then follows that

$$(\mathcal{F}(G))(k) = 1 - i\hat{\omega}k - \hat{\xi}^2k^2 + \dots, \quad (\text{A.2})$$

where the coefficients are defined as

$$\hat{\omega} = \int_{-\infty}^{+\infty} G(y)ydy, \quad \hat{\xi}^2 = \frac{1}{2} \int_{-\infty}^{+\infty} G(y)y^2dy.$$

Now, consider the equation

$$(I - \xi^2\nabla^2 + \omega\nabla)A_{n+1} = f(D_n). \quad (\text{A.3})$$

This is the same as Eq. (3.3) except that the mapping model f only depends on D_n . Let us relate ξ and ω above with $\widehat{\xi}$ and $\widehat{\omega}$ of Eq. (A.2). By taking Fourier transform of both sides, we have

$$\mathcal{F}(A_{n+1}) = \frac{1}{1 + i\omega k + \xi^2 k^2} \mathcal{F}(f). \quad (\text{A.4})$$

Therefore,

$$A_{n+1}(x) = (G * f)(x), \text{ where } (\mathcal{F}(G))(k) = \frac{1}{1 + i\omega k + \xi^2 k^2}. \quad (\text{A.5})$$

By Taylor expansion, we see that

$$(\mathcal{F}(G))(k) = 1 - i\omega k - (\xi^2 + \omega^2)k^2 + \dots$$

Comparing the above with Eq. (A.2), we have

$$\widehat{\omega} = \omega, \quad \widehat{\xi}^2 = \xi^2 + \omega^2.$$

If $\omega^2 \ll \xi^2$, then $\widehat{\xi}^2 = \xi^2$. Therefore, $G = \mathcal{F}^{-1}\left(\frac{1}{1+i\omega k+\xi^2 k^2}\right)$. We point out that Eq. (A.1) (or a discretized version thereof) has been used in several other publications to describe electronic couplings between cells. For example, the papers [29] and [75] used the Gaussian kernel $G(y) = \exp(-\mu y^2)$.

Note that Eq. (A.1) is an approximation. It is more realistic to use a biophysical ionic model, and it is thus of interest to relate Eq. (A.1) to ionic models. For a simple two variable ionic model, [40] demonstrated that $\widehat{\omega}$ and $\widehat{\xi}$ can be calculated explicitly in certain limiting cases, giving

$$\widehat{\omega} = \frac{2D}{c}, \quad \widehat{\xi} = (D \times \text{APD}_c)^{1/2},$$

where D denotes the diffusion coefficient in the two variable ionic model, c denotes CV of a propagating wave and APD_c denotes APD at the bifurcation point. Using typical values of D , c and APD_c , the length $\widehat{\xi}$ is on the order of 1 mm, while $\widehat{\omega}$ is on the order 0.1 mm.

The authors of [39] adjust the value of $\omega (= \widehat{\omega})$ to 0.35 mm in order to produce spatial patterns that are similar to what they observe experimentally. We also investigate the effect of changing ω on dynamic behaviors of spatially coupled mapping model, and determine that it has a minor effect. For instance, $\omega = 0.1$ mm leads to simpler dynamic behaviors. Therefore, we use $\xi = 1$ mm and $\omega = 0.35$ mm in chapter 3, without loss of generality.